

Epitaxial metal nanocrystal-semiconductor quantum dot hybrid structures for plasmonics

Citation for published version (APA):

Urbanczyk, A. J. (2012). *Epitaxial metal nanocrystal-semiconductor quantum dot hybrid structures for plasmonics*. [Phd Thesis 1 (Research TU/e / Graduation TU/e), Applied Physics and Science Education]. Technische Universiteit Eindhoven. <https://doi.org/10.6100/IR734702>

DOI:

[10.6100/IR734702](https://doi.org/10.6100/IR734702)

Document status and date:

Published: 01/01/2012

Document Version:

Publisher's PDF, also known as Version of Record (includes final page, issue and volume numbers)

Please check the document version of this publication:

- A submitted manuscript is the version of the article upon submission and before peer-review. There can be important differences between the submitted version and the official published version of record. People interested in the research are advised to contact the author for the final version of the publication, or visit the DOI to the publisher's website.
- The final author version and the galley proof are versions of the publication after peer review.
- The final published version features the final layout of the paper including the volume, issue and page numbers.

[Link to publication](#)

General rights

Copyright and moral rights for the publications made accessible in the public portal are retained by the authors and/or other copyright owners and it is a condition of accessing publications that users recognise and abide by the legal requirements associated with these rights.

- Users may download and print one copy of any publication from the public portal for the purpose of private study or research.
- You may not further distribute the material or use it for any profit-making activity or commercial gain
- You may freely distribute the URL identifying the publication in the public portal.

If the publication is distributed under the terms of Article 25fa of the Dutch Copyright Act, indicated by the "Taverne" license above, please follow below link for the End User Agreement:

www.tue.nl/taverne

Take down policy

If you believe that this document breaches copyright please contact us at:

openaccess@tue.nl

providing details and we will investigate your claim.

Epitaxial Metal Nanocrystal-Semiconductor Quantum Dot Hybrid Structures for Plasmonics

PROEFSCHRIFT

ter verkrijging van de graad van doctor aan de Technische Universiteit
Eindhoven, op gezag van de rector magnificus, prof.dr.ir. C.J. van Duijn,
voor een commissie aangewezen door het College voor Promoties in het
openbaar te verdedigen op donderdag 20 september om 16.00 uur.

door

Adam Jan Urbańczyk

geboren te Wrocław, Polen

Dit proefschrift is goedgekeurd door de promotor:

prof.dr. P.M. Koenraad

Copromotor:

dr. R. Nötzel

A catalogue record is available from the Eindhoven University of Technology Library

ISBN: 978-90-386-3193-6

Subject headings: molecular beam epitaxy, quantum dots, metal nanocrystals, surface plasmon resonance, plasmonics

The work presented in this thesis was carried out in the group of Photonics and Semiconductor Nanophysics at the Department of Applied Physics of the Eindhoven University of Technology, the Netherlands.

This work was supported by the Smart Mix Program of the Dutch Ministry of Economic Affairs and the Dutch Ministry of Education, Culture and Science.

Cover design by A.J. Urbańczyk

Printed by Ipskamp Drukkers

Contents

List of abbreviations	v
Scope of the Thesis	1
1 Introduction	3
1.1 History of metal nanostructures	3
1.2 Synthesis and fabrication	4
1.2.1 Bottom-up methods	4
1.2.2 Top-down methods	7
1.2.3 Positioning and self-assembly	8
1.3 Optical properties	10
1.3.1 Plasmonics	11
1.3.2 Quasi-static approximation	12
1.3.3 Effects of size	13
1.3.4 Effects of shape	14
1.3.5 Plasmonic materials	15
1.3.6 Effects of material quality and crystallinity	16
1.3.7 Effects of dielectric environment	17
1.3.8 Complex structures	17
1.4 Semiconductor quantum dots	18
1.5 Metal quantum dots	18
1.6 Physical and chemical properties	19
1.7 Applications	19
1.7.1 Emission enhancement	19
1.7.2 Active plasmonics	22
1.7.3 Plasmonic sensing	23
1.7.4 Quantum dot formation	24
1.8 Summary	24
References	24
2 Sample growth, processing and characterization	31
2.1 Epitaxy	31
2.1.1 Metalorganic vapor phase epitaxy	32
2.1.2 MBE	33
2.1.3 Growth modes	34
2.2 Surface reconstructions	36
2.3 RHEED	36
2.4 Optical characterization	38
2.4.1 Differential reflectivity	38

2.4.2	Photoluminescence	40
2.5	AFM	40
2.6	Processing	41
2.6.1	Photolithography	41
2.6.2	Wet etching	41
2.6.3	Cleaning procedure for epitaxial regrowth	42
2.7	Summary	42
	References	42
3	In nanocrystals	45
3.1	Epitaxial metal nanocrystals	45
3.2	Experimental details	45
3.3	Structural properties	46
3.4	Optical properties of In nanocrystals	48
3.5	Positioning of the In nanocrystals on InGaAs quantum dot arrays	48
3.6	Photoluminescence of In nanocrystal/quantum dot arrays	51
3.7	Formation of isolated metal-semiconductor hybrid structures	52
3.8	Summary	54
4	Conversion of In nanocrystals into quantum dots	57
4.1	Droplet epitaxy	57
4.2	Experimental details	58
4.3	Structure and morphology	59
4.4	Optical properties	63
4.5	Summary	65
	References	66
5	Ag nanocrystals and hybrid quantum dot-Ag nanocrystal structures	69
5.1	Why In is not enough?	69
5.2	Experimental details	69
5.3	Structural properties of Ag nanocrystals	71
5.4	Shape, size and density control	71
5.5	Optical properties	72
5.6	Positioning on individual quantum dots	72
5.7	Optical properties of hybrid structures	75
5.8	Summary	77
	References	77
6	Positioning of Ag nanocrystals on patterned substrates	79
6.1	Importance of long-range ordering	79
6.2	Experimental details	81
6.3	Ordering	82
6.4	Room temperature photoluminescence emission	84
6.5	Challenges	86
6.6	Summary	87

References	87
7 Conclusions and outlook	91
Abstract	93
Acknowledgements	95
List of publications	97
Curriculum vitae	99

List of abbreviations

0D	zero dimensional
1D	one dimensional
2D	two dimensional
3D	three dimensional
AFM	atomic force microscope
CMOS	complementary metal-oxide semiconductor
CVD	chemical vapor deposition
DE	droplet epitaxy
DR	differential reflectivity
DUV	deep ultra-violet
EBID	electron beam induced deposition
EBL	electron beam lithography
EELS	electron energy loss spectroscopy
EUV	extreme ultra-violet
FIB	focused ion beam
FM	Frank van der Merwe
LSPR	localized surface plasmon resonance
LT	low temperature
MBE	molecular beam epitaxy
ML	monolayer
MOVPE	metalorganic vapour phase epitaxy
NC	nanocrystal
NIL	nanoimprint lithography
NIR	near infrared

List of abbreviations

PL	photoluminescence
PR	photo resist
PSP	propagating surface plasmon
PVD	physical vapor deposition
QD	quantum dot
QW	quantum well
RHEED	reflection high-energy electron diffraction
RT	room temperature
SEM	scanning electron microscope
SERS	surface enhanced Raman scattering
SK	Stranski-Krastanov
SL	superlattice
SPR	surface plasmon resonance
UHV	ultra high vacuum
UV	ultra-violet
VW	Vollmer-Weber
WL	wetting layer

Scope of the Thesis

The main goal of this thesis is to demonstrate the feasibility of epitaxial growth of Ag and In nanocrystals (NCs) on GaAs semiconductor substrates using molecular beam epitaxy (MBE), as well as to show ordering of such supported nanocrystals relying on self-assembly. This includes self-assembly on quantum dots (QDs) and artificially patterned substrates. The second goal of the thesis is to demonstrate that such metal NCs support localized surface plasmon resonances (LSPRs) in the near infrared (NIR) wavelength range, and that they can be used to modify the optical properties of QDs in complex metal NC semiconductor QD structures. Last, but not least, the final goal is to demonstrate that MBE-grown In NCs can be transformed in-situ into optically active QDs of high quality, and to investigate the influence of different growth parameters on this process.

The first chapter is a general introduction to the topic of metal NCs. It reviews different ways of obtaining them, as well as their properties. Different applications of metal NCs are discussed, with special treatment of LSPR-based enhancement of the optical properties of nearby emitters.

The second chapter contains a description of experimental apparatus, measurement set-ups and procedures used for growth, fabrication and characterization of the investigated samples. This includes detailed description of the MBE growth and reactors, as well as discussion of reflection high-energy electron diffraction (RHEED) for growth monitoring and structural characterization of the samples. Characterization methods for morphology analysis, namely atomic force microscope (AFM), are also described. Additionally, the principles and technical construction of photoluminescence (PL) and differential reflectivity (DR) set-ups used for characterization of optical properties are discussed. Moreover, techniques used for patterning and cleaning of the samples are presented.

In the chapter 3 the growth and properties of epitaxial In NCs on GaAs substrates are discussed. The epitaxial relation is derived from RHEED patterns observed after In deposition. Profound impact of the starting surface reconstruction of GaAs on final NC shape is demonstrated. The optical properties, namely surface plasmon resonance (SPR) wavelength measurements, are presented. What is more, ordering of In NCs on one dimensional (1D) arrays of InGaAs QDs is demonstrated. It is also shown that such structures facilitate LSPR-QD coupling down to the single QD level. Finally, the growth of low-density hybrid In NC-InAs island nanostructures, with possible applications in ultrafast switching of the LSPR wavelength, is described.

List of abbreviations

Conversion of In NCs into QDs is discussed in the fourth chapter. As an introduction the idea of droplet epitaxy (DE) is described. Afterwards, the structure and morphology of the QDs obtained in such a process are discussed. Finally, the results of PL measurements are presented, proving high quality of the investigated QDs and demonstrating their potential application as long-wavelength sources.

Chapter 5 is concerned with the growth and properties of Ag NCs and hybrid QD–Ag NC structures. The structure and morphology of the NCs are discussed, and routes of size, density and shape control are demonstrated. Subsequently, tuning of the SPR wavelength and its polarization dependence are presented. Finally, the self-assembly based positioning of Ag NCs on low density, near-surface QDs is demonstrated. It is shown that such hybrid structures have enhanced emission as compared to bare QDs.

In chapter 6 the positioning of Ag NCs on artificially patterned GaAs substrates is presented. It is demonstrated that under appropriate conditions Ag NCs nucleate in small holes with a high degree of reproducibility, offering an easy way to obtain ordered structures relying on guided self-assembly.

The thesis is concluded by a discussion of applications of the obtained results in chapter 7. Furthermore, the impact of the obtained results on future research, and some possible routes for their further development are outlined.

1 Introduction

1.1 History of metal nanostructures

One could argue that the topic of metal nanostructures or nanoparticles is nothing new. Indeed, already in times of ancient Rome they were applied for the coloring of glass, the Lycurgus Cup being a well known example of this technique. In the middle ages, the same principle was used to obtain beautiful coloring of stained glass in gothic churches. Obviously, all this was without any understanding of the underlying physics at all, however it clearly demonstrates that the field was initially driven only by applications.

For the first time metal nanostructures appeared in a more scientific setting, when in 1857 Lord Faraday investigated the colors of gold colloids [2]. The effect was theoretically explained by Gustav Mie around 1900 [3], who found an analytical formula to describe the optical properties of a metal sphere of arbitrary size. This by no means concludes the story. The discovery of effects such as modification of the radiative lifetime of an emitter near a metal surface [4], surface enhanced Raman scattering (SERS) [5] and extraordinary transmission through arrays of subwavelength features in optically thick metal layers [6] fueled the interest. On the other hand, rapid progress was enabled by developments in nanoscale fabrication, characterization, chemical synthesis and more and more widespread availability of computational power for electromagnetic simulations. All this caused an explosion of interest in the fabrication and properties of metal nanostructures in the late 20th and the beginning



Figure 1.1: The famous Lycurgus Cup dated to 30BC-640AD, exhibiting different colours in reflected (left image) and transmitted (right image) light due to nanoscale metal particles embedded in the glass (photo from [1])

1 Introduction

of 21st century.

As many rapidly growing and interdisciplinary fields of science nowadays, it bears a name ending with *onics*, namely plasmonics. This comes from the fact that metal nanostructures support certain electromagnetic modes called LSPRs or propagating surface plasmons (PSPs)¹ in the case of confined or extended structures, respectively. Plasmonics remains a very active field of research, as it promises many different applications with possibly very high impact on society and natural environment. These applications include more efficient solar cells and other energy conversion devices, more efficient solid-state light sources, biosensors, targeted drug delivery, nanoscale lasers and other active devices [7]. Only time can tell if these promises will be really fulfilled, however the author remains an optimist in this respect.

1.2 Synthesis and fabrication

In general, there are two types of approaches to prepare metal nanostructures, actually any kind of nanostructures, top-down and bottom-up. The first one utilizes tools that can fabricate a nanoscale object from a larger one. These include electron beam or optical lithography and etching of thin metal films, focused ion beam (FIB)-milling as well as electron beam induced deposition (EBID) for direct writing of metals. The second type of approach is based on self-assembly and includes chemical synthesis of metal colloids, physical vapor deposition (PVD) or chemical vapor deposition (CVD) of metal NCs on a substrate. One could also consider "hybrid" approaches, that combine artificially patterned templates with self-assembly techniques, in order to achieve size, density and shape control. All these techniques will be reviewed in the current section.

1.2.1 Bottom-up methods

In this category the most widely used method to obtain metal NCs is solution phase chemical synthesis. It is very versatile in terms of shape and size control. By changing process conditions, one can obtain a large variety of morphologies, as can be seen in figure 1.2. Moreover, it does not require large capital investments to buy necessary equipment, as compared to techniques requiring high vacuum for example. It is also very actively developed, what can be inferred from the number of recent publications found after performing a query on this topic in any scientific database.

The solution phase chemical synthesis usually follows a general scheme. One needs a metal salt MR of a corresponding acid HR, that is soluble in

¹Sometimes also called Surface Plasmon Polariton, due to the fact that they are excitations arising from coupling of electromagnetic field (photons) with electron plasma (plasmons) in metal.

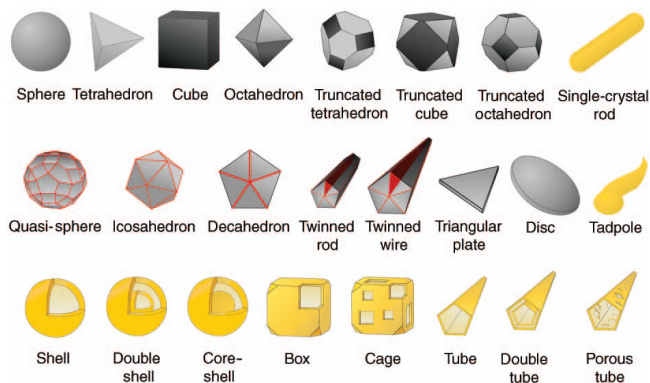


Figure 1.2: Variety of shapes obtainable by solution phase chemical synthesis. Golden-coloured structures can be synthesized only from gold, grey-coloured from silver, except for spheres, twinned rods, icosahedrons, and cubes, which can be also synthesized from gold (image adapted from [8]).

a given reaction medium. Under appropriate conditions, usually elevated temperature and stirring, the so called reducing agent is added, for example sodium citrate, that reduces the M^+ dissolved in the reaction medium into neutral atoms M^0 . They bind together to form initial nuclei and eventually the desired nanostructures. Usually some kind of stabilizing or capping agent is also added to prevent aggregation and also possibly allow shape control due to preferential adsorption to different crystallographic planes.

A specific and well known example of the general scheme is the polyol synthesis of Ag nanostructures [9]. In this case ethylene glycol (or a different polyol) acts both as the reaction medium and the reducing agent. The Ag salt used is usually $AgNO_3$. Additionally, capping agents are added in order to stabilize and direct the growth of the Ag NCs offering the possibility of shape control. One commonly used capping agent is poly(vinyl pyrolidone) (PVP), which is preferentially binding to $\{100\}$ Ag facets, what stabilizes them and defines the final shape of the synthesized NCs. The discussed process produces usually a mixture of shapes - pentagonal wires, bipyramids and cubes, which correspond to fivefold twinned crystals, bicrystals and single crystalline particles, respectively. Further selection of shape is possible by adding Cl^- ions in form of NaCl or HCl that, in conjunction with O_2 from the air, will etch the Ag NCs. Due to higher corrosion resistance of the monocrystalline NCs only the cubes remain.

Solution phase synthesis of metal NCs is clearly very versatile. There are even further possibilities like two step synthesis, using different reducing agents and utilizing galvanic displacement and subsequent etching to obtain hollow structures. Excellent reviews of different synthetic techniques and tricks can be found for example in [9].

1 Introduction

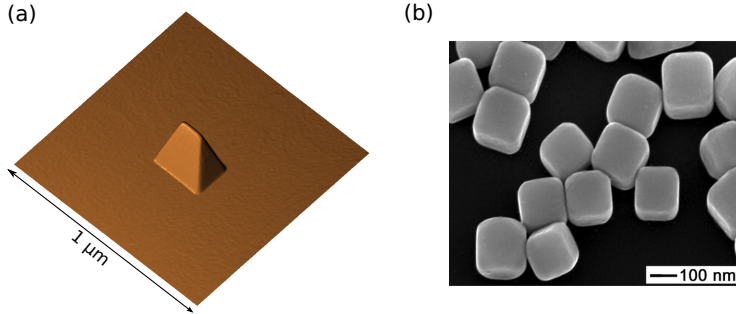


Figure 1.3: AFM image of a single Ag nanocrystal on a GaAs substrate obtained by MBE (a), and SEM image of Ag nanocrystals synthesized chemically.

Alternatively to chemical synthesis, one can rely on vacuum deposition techniques, namely PVD or CVD, to obtain metal NCs supported on a substrate. PVD can be defined as any deposition process using some "physical" phenomenon to transport the material onto the substrate. This includes resistive or e-beam evaporation and subsequent condensation on the substrate, as well as sputtering, that is removal of the target material due to bombardment by ions. CVD on the other hand uses volatile or gaseous substances like metalorganics, hydrides or halides that contain atoms of the material to be deposited. Such substances, usually called precursors, are transported in the vapor phase and undergo decomposition at the heated surface of the substrate leaving the desired materials. These two general techniques have many specific variants and modifications; a description of them can be found for example in [10]. It has to be noted at this point, that the specific technique used in this thesis is MBE which is a rather specialized member of the PVD class. It is described in full detail in chapter 2 of the thesis. If one deposits a crystalline material, whatever the exact technique is, on top of a single crystal substrate, epitaxial growth can occur. This means that the deposit has a well-defined crystallographic orientation with respect to the orientation of the substrate. Epitaxy is usually not trivial - additional necessary conditions to be fulfilled include high enough substrate temperature and low enough background contamination. In case of heteroepitaxy, that is deposition of a material different than the substrate, three different kinds of behaviours, so called growth-modes can be observed. They are the Frank van der Merwe (FM), Stranski-Krastanov (SK) and Vollmer-Weber (VW) growth modes. The first one is layer-by-layer growth, this means that the deposit forms a uniform two dimensional (2D) layer. In case of the SK growth first a thin 2D layer (called wetting layer (WL)) develops, and when the amount of the deposited material reaches a certain value (called critical thickness), three dimensional (3D) islands form. In the case of the VW growth 3D islands form right from the beginning. Obviously, the last two growth modes can be used to obtain supported metal NCs. Table

Table 1.1: Examples of different growth modes. Adapted from [11].

Frank-van der Merwe growth mode	Stranski-Krastanov growth mode	Vollmer-Weber growth mode
many metals on metals, e.g. Pd/Au, Au/Pd, Ag/Au, Au/Ag, Pd/Ag, Pb/Ag, Pt/Au, Pt/Ag, Pt/Cu	some metals on metals, e.g. Pb/W, Au/Mo, Ag/W	most metals on alkali halides
alkali halides on alkali halides	many metals on semiconductors, e.g. Ag/Si, Ag/Ge, Au/Si, Au/Ge, Sn/GaAs, Ag/GaAs	most metals on graphite
many III-V semiconductors on III-V semiconductors, e.g. AlGaAs/GaAs, InGaAsP/InP, InAlAs/InP, InGaP/GaAs	many III-V semiconductors on III-V semiconductors, e.g. InGaAs/GaAs, InGaAs/InP, InP/GaAs	most metals on MgO
some IV semiconductors on III-V semiconductors e.g. Ge/GaAs, Si/GaP	IV semiconductors, e.g. Ge/Si	most metals on MoS ₂

1.1 shows examples of all three behaviours in different material systems. It can be seen that island formation is actually quite common. The case of metals on semiconductors is especially interesting and is investigated in-depth in the thesis. This is because it provides the possibility of integrating metal NCs with active semiconductor structures emitting light.

1.2.2 Top-down methods

Probably the most widely used top-down method for the fabrication of metallic nanostructures is electron beam lithography (EBL). It uses a tightly focused electron beam in the 50-100 kV range that is scanned across the surface of the sample, which is covered with an e-beam sensitive material called an e-beam resist. A positive resist becomes more soluble in a developer due to electron exposure and a negative one becomes less soluble. One specific example of an e-beam resist is poly(methyl methacrylate) (PMMA), which is a positive one. After exposure and development a pattern is created. Such a pattern can be transferred to the underlying thin metal layer for example by chemical or plasma etching. Another possibility is to deposit the metal on top of a developed resist layer, and then to perform a lift-off, that is immersion of the sample in a solvent. After such a procedure only the metal without resist underneath will remain attached to the substrate. EBL can achieve very high resolution down to a few nm [12] due to the very small wavelength

1 Introduction

associated with high energy electrons. Actually, in practice the factor limiting the resolution is not diffraction, but rather scattering of the electrons within the substrate.

Another possibility to achieve nanometer scale supported metal structures is by directly physically patterning thin metal film by FIB-milling [13, 14]. This method uses an accelerated and finely focused beam of massive ions, such as Ga^+ , from a liquid metal ion source. The ions have enough energy to locally sputter away material, and in this way can generate the desired pattern after scanning the beam over the substrate surface. In terms of resolution this technique has similar performance to EBL. Both techniques share also a serious disadvantage, namely intrinsically low throughput due to the scanning-based patterning process. It is, however, necessary to mention, that there are companies [15] trying to solve this issue by developing high-throughput EBL systems with multiplexed electron beam sources.

There are two additional techniques closely related to EBL and FIB, namely e-beam [16–19] and FIB [13] induced deposition. They both utilize the fact that a gaseous metal precursor adsorbed on a substrate can be cracked by an energetic beam of charged particles leaving a tiny deposit of the desired material. This is in direct analogy to CVD, but with very small spatial extent. By scanning the beam one can deposit an arbitrarily shaped structure. Induced deposition does not require any further processing steps what is very advantageous. It does, however, inherit all the disadvantages of its parent techniques due to the scanning nature of the process. Additionally, the deposited material quality and purity might be an issue, what is caused by the high incorporation of impurities due to low deposition temperature.

Although not really developed at present, there is a possibility to leverage the complementary metal-oxide semiconductor (CMOS) technology and utilize commercial state of the art deep ultra-violet (DUV) and extreme ultra-violet (EUV) lithography tools that offer better and better resolution. In case of sufficient economic motivation, such tools together with clever processing techniques could enable large scale and high throughput fabrication of metal nanostructures on semiconductor substrates. An additional high throughput technique to fabricate such nanostructures is nanoimprint lithography (NIL) [20]. It uses a master mold to imprint a pattern in a thin polymer layer which covers the processed substrate. This is in direct analogy to the well-known molding process, but performed at the nanoscale. NIL is very accessible in terms of cost and has been already used successfully to obtain metallic structures with nanoscale dimensions [21].

1.2.3 Positioning and self-assembly

In order to use metal nanostructures together with different photonic and electronic devices, one has to be able to place them arbitrarily on

a substrate, so that they can interact with other building blocks of the desired integrated system. Moreover, in order to tailor and optimize the properties of the metal nanostructures, it is desirable to put them close together, so that they form complex arrangements, like dimers, with very small gaps between the elements. This facilitates coupling of the LSPR modes in both nanostructures and causes that such structures have better optical properties in terms of local field enhancement, as will be discussed in the following sections. However, this coupling, in order to work, requires extreme positional accuracy at the single nanometer level due to the high degree of localization of the LSPRs. The same degree of positional accuracy is needed for fabrication of active devices, because they require controlled separation of the metal particle and an optical emitter.

Position control is an intrinsic feature of lithography based techniques. They offer a high degree of uniformity over large area surfaces and arbitrary control of the placement of each metal structure at large length scales. This would be required if one wanted to fabricate, in direct analogy to the ubiquitous microelectronic integrated circuits, integrated plasmonic circuits with different interconnected passive and active devices on one substrate or semiconductor chip. However, lithographic techniques are not very good at generating features that are spaced apart below 10 nm. What is more, it is not clear if lithography can position accurately the metal nanostructures with respect to optical emitters, especially at the single emitter level. If one considers, for example, position controlled SK QDs [22] as a basis of active structures, not only high resolution of the individual lithography steps, but also overlay of the multiple lithography steps defining the QD and metal NC position is needed. Probably, the achievable overlay precision will not be enough to obtain optimized active structures with high yield. Extremely precise positioning of metal nanostructures, both with respect to each other and individual emitters, is much easier to achieve with self-assembly based approaches. Such approaches may utilize the following effects: electrostatic and capillary forces, polymer mediated interactions, assembly on organic templates, covalent bond formation [9], as well as strain driven migration and preferential nucleation [23]. On the other hand, it is very difficult to obtain long distance ordering on a substrate. All the mentioned assembly approaches, except for the last one, are liquid phase based processes. Usually, the transfer of the metal nanostructures from the liquid phase onto a substrate is based on drop-casting, that is dispersing a small amount of the solution onto the substrate and subsequent evaporation of the solvent. This is inherently a random process leaving no or little long range ordering of the metal nanoparticles. Without any additional measures, arbitrary placement on a substrate is not possible with such a process. Strain driven migration can indeed produce long-range ordering [23], but only in the form of simple periodic arrangements. Arbitrary placement control over large areas is not possible.

1 Introduction

Clearly, there is no one ideal approach offering both very good long range and short range position control. The author thinks, that it will be necessary to consider hybrid approaches, utilizing both lithography and self-assembly, in order to make full use of plasmonics and facilitate the fabrication of integrated plasmonic circuits. One of such hybrid approaches will be investigated in chapter 6 considering the self assembly of Ag nanocrystals on a patterned semiconductor substrate with the help of near-surface SK QDs.

1.3 Optical properties

Without no doubt the enormous interest in metal nanostructures is mainly due to their optical properties that allow to manipulate light at deep subwavelength length-scales and in the regime of very high local fields. This, in turn, enables all kinds of interesting effects like spontaneous emission enhancement, SERS and many others. In order to understand the optical properties of metal nanostructures, one has to consider first the optical properties of bulk metals. The bulk properties of any material can be explained by using its complex dielectric function $\epsilon(\omega) = \epsilon_1(\omega) + i\epsilon_2(\omega)$ or its complex refractive index $\tilde{n} = n + i\kappa$. Those quantities are related through the following equations

$$\begin{aligned}\epsilon_1 &= n^2 - \kappa^2, \\ \epsilon_2 &= 2n\kappa,\end{aligned}$$

where n is the refractive index from Snell's law and κ is the extinction coefficient that determines the amount of absorption in a given medium. It is related to the absorption coefficient A by Beer's law (describing the exponential decrease of the intensity of during propagation in a lossy medium $I(x) = I_0 \exp^{-Ax}$)

$$A(\omega) = \frac{2\kappa(\omega)\omega}{c}.$$

One can see that ϵ_2 determines how lossy a given medium is, and for non-absorbing media $\epsilon_2 = 0$. What is more, for weakly absorbing media, mainly the real part of ϵ determines the refractive index, that is $n \approx \sqrt{\epsilon_1}$.

Due to causality, ϵ_1 and ϵ_2 are not independent, they must obey the Kramers-Kronig relation. In practice, one can decompose any physical dielectric function into a sum of Drude and Lorentz oscillators, which correspond to the free electron response and interband transitions or lattice vibration absorption, respectively. In case of metals the free-electron response dominates and usually is sufficient to explain the optical properties over a wide range of frequencies. For an electron gas with density n , characteristic collision frequency $\gamma = \frac{1}{\tau}$ and electron effective

Table 1.2: Drude model parameters for different metals. Adapted from [24]

metal	$\hbar\omega_p$, eV	$\hbar\gamma$, eV
Ag	9.04	0.021
Au	8.89	0.071
Cu	8.76	0.096
Li	6.45	0.13
Na	5.93	0.038
Al	12.04	0.12
Ga	14.05	1.5
In	12.8	0.46

mass m the Drude dielectric function is given by:

$$\epsilon_{Drude}(\omega) = 1 - \frac{\omega_p^2}{\omega^2 + i\gamma\omega},$$

where $\omega_p^2 = \frac{ne^2}{\epsilon_0 m}$ is the characteristic plasma frequency. Both ω_p and γ parameters are given for many metals of interest in table 1.2. It is evident that Ag and Au have the lowest losses of all metals, and that is why they are most often used for plasmonics. Obviously other materials can be and are used, but at the price of much higher resistive losses. Another advantage of using noble metals is their chemical stability and resistance to oxidation. Both Au and Ag do not oxidize easily. In case of the latter metal, there is however the possibility of corrosion in the presence of S and S containing compounds. Formation of sulphides is the reason of the well-known phenomenon of tarnishing of Ag.

1.3.1 Plasmonics

Bulk metals support certain elementary excitations due to collective oscillations of free electrons that are called bulk plasmons. The frequency of such modes for $k = 0$ is equal to the plasma frequency ω_p of the given metal, which is one of the parameters of the Drude model. Bulk plasmons are longitudinal waves, thus they cannot couple to electromagnetic waves which are transverse. They couple however to e-beams passing through the material, causing characteristic energy losses that are multiples of ω_p . The spectroscopic technique utilizing this effect is called electron energy loss spectroscopy (EELS). Careful EELS studies reveal an additional loss peak at $\omega_p/\sqrt{2}$ for large k numbers. This is due to the surface plasmons or PSPs at the metal-vacuum interface. One can see the idealized dispersion relation $\omega(k)$ for both bulk and surface plasmons in figure 1.4. For the sake of completeness it has to be mentioned that above ω_p photons propagating inside the metal are referred to as bulk plasmon-polaritons. The PSP branch lies to the right of the photon dispersion line, what means that it does not couple to the electromagnetic field. Indeed, optical excitation of the PSP requires special tricks like using gratings for momentum matching or evanescent coupling. The electromagnetic field associated with a surface plasmon is strongly localized at the interface

1 Introduction

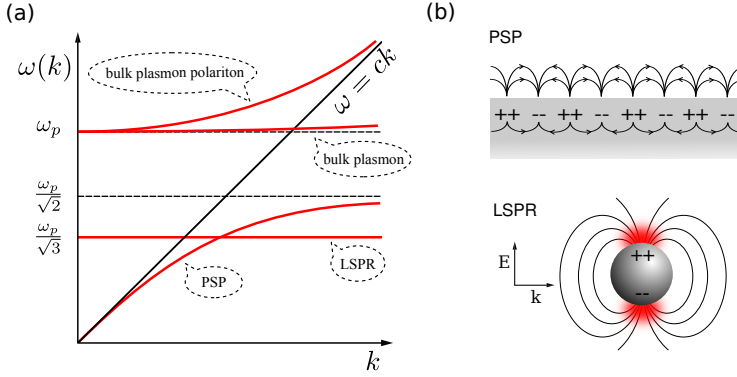


Figure 1.4: Dispersion relation of bulk plasmon-polariton, bulk, surface and localized plasmon in case of vanishingly small damping ($\epsilon_2 \rightarrow 0$) (a). The localized plasmon is shown for the dipole resonance of a small metal sphere in vacuum. Schematic depiction of the propagating and localized surface plasmons (b).

and decays exponentially in both directions. If one considers the surface of a small ($R \ll \lambda$) metal sphere in vacuum, it will support similar modes, albeit with a discrete spectrum due to the finite size. The allowed frequencies are given by $\epsilon_l = \frac{l+1}{l}$, $l = 1, 2, 3, \dots$. For $l = 1$ one observes a dipole mode, for $l = 2$ a quadrupole mode, and so on. These are the LSPRs that can be physically understood as standing waves arising due to interference of PSPs on a finite metal surface. The resonance frequency of the lowest mode in the case of a Drude metal with negligible losses equals $\omega = \frac{\omega_p}{\sqrt{3}}$. In the case of the LSPR the field is also strongly confined at the interface, however there is no translational symmetry, and thus momentum conservation is not relevant. This means that LSPRs couple well to electromagnetic radiation and no additional measures to facilitate this are necessary. To conclude, metal structures support different electromagnetic modes which offer subwavelength confinement of light and plasmonics is the multidisciplinary field of research that includes fabrication, characterization and application of such structures.

1.3.2 Quasi-static approximation

The understanding of the optical properties of a small metal sphere excited by an electromagnetic wave can be reduced to an analytically solvable problem in electrostatics provided that the condition $R \ll \lambda$ is met. This is due to the fact that on the length scale of the sphere diameter the variation of the electric field can be neglected. Such an assumption is called the quasi-static approximation. Following the derivation found in e.g. [25] one can obtain the polarizability α , defined as $\mathbf{p} = \epsilon_0 \epsilon_m \alpha \mathbf{E}_0$

of such metal object:

$$\alpha = 4\pi R^3 \frac{\epsilon - \epsilon_m}{\epsilon + 2\epsilon_m},$$

where ϵ is the dielectric constant of the sphere and ϵ_m of the surrounding medium. Obviously when $|\epsilon + 2\epsilon_m|$ reaches a minimum, the $|\alpha|$ will have the maximum value. In case of small or slowly varying ϵ_2 the resonance condition simplifies to $\epsilon_1 = -2\epsilon_m$. The mode associated with this resonance is the dipolar localized surface plasmon. It has to be mentioned that in the derivation of α no explicit assumptions about the nature of the material of the sphere are made. This means that the formula is valid for any physical dielectric function. However, for a resonance to be observed it is necessary that $\epsilon_1 < 0$, which can be met only for the electron plasma in metals and semiconductors or in the case of dielectrics in the far-infrared frequency anomalous dispersion range of lattice absorption [26]. In the latter case, one calls such modes localized surface phonon polaritons, as they arise due to the coupling of the electromagnetic field and lattice vibrations.

The polarizability of a small metal sphere is complex, what means that the sphere will both scatter and absorb light. The total extinction cross-section $C_{ext} = C_{sca} + C_{abs}$ determines the absorption coefficient A of a medium with N scatterers per unit volume, namely $A = NC_{ext}$. The contribution of each effect equals

$$C_{sca} = \frac{k^4}{6\pi} |\alpha|^2,$$

$$C_{abs} = k \text{Im}[\alpha].$$

It is evident that scattering and absorption scale differently with particle size. For small sizes absorption dominates ($\propto R^3$), and for larger ones scattering is more significant ($\propto R^6$). For this reason it is much easier to measure the optical response of larger metal structures than that of smaller ones, especially in case of single particle scattering experiments.

1.3.3 Effects of size

In order to account for the influence of size effects on the optical properties of metal nanoparticles, one has to divert from the quasi-static approximation. This can be done rigorously utilizing the Mie scattering theory. On the other hand, to gain physical insight one can also use so-called Modified Long-Wavelength Approximation [27], which is much less mathematically involved. It includes the effects of radiation damping and dynamic depolarization on the polarizability of a metal sphere. The polarization inside of the sphere, which is assumed to be uniform in this approximation, is given by $\mathbf{p} = \epsilon_0 \epsilon_m \alpha (\mathbf{E}_0 + \mathbf{E}_{corr})$, where the correction field \mathbf{E}_{corr} equals

$$\mathbf{E}_{corr} = \frac{2}{3} i k^3 \mathbf{p} + \frac{k^2}{R} \mathbf{p}.$$

1 Introduction

The first term is due to the dipole radiating energy away into space, and the second one is due to dynamic depolarization. One can obtain the effective polarizability defined as $\mathbf{p} = \alpha_{eff} \mathbf{E}_0$

$$\alpha_{eff} = \frac{\alpha}{1 - \frac{k^2}{4\pi R} \alpha - i \frac{k^3}{6\pi} \alpha}$$

The main result of this analysis is twofold. Firstly, the LSPR position redshifts with increasing size, and secondly the strength of the resonance, i.e. local field enhancement, decreases, what is accompanied by an increase of the linewidth.

So far it was assumed that the dielectric function of a small metal particle is the same as that of a macroscopic one. In reality, one observes increased damping due to surface effects [26] that usually obeys the empirical relation

$$\gamma = \gamma_\infty + \frac{A}{R},$$

where A is a proportionality constant depending both on the material and the exact state of the surface. Such enhanced damping is especially important in the case of very small particles and structures made of finely polycrystalline material.

1.3.4 Effects of shape

One can incorporate easily the effect of shape into the quasi-static approximation provided that the shape can be approximated by an ellipsoid with semiaxes a_1, a_2, a_3 . The generalized expression for α in the direction of the i -th semiaxes is given by [25]

$$\alpha_{eff} = 4\pi a_1 a_2 a_3 \frac{\epsilon - \epsilon_m}{3\epsilon_m + 3L_i(\epsilon - \epsilon_m)},$$

where L_i is a geometrical quantity with the following definition

$$L_i = \frac{a_1 a_2 a_3}{2} \int_0^\infty \frac{dq}{(a_i^2 + q) \sqrt{\sum_j (q + a_j^2)}}.$$

This geometric factor obeys the rule $\sum L_i = 1$, and in the case of a sphere $L_i = \frac{1}{3}$. This complicated analytical result translates into the fact that for non-spherical particles the resonance splits into multiple modes with different eigenfrequencies due to symmetry breaking of the particles. This also means that depending on the orientation of such anisotropic metal structures and polarization of the incoming light one can excite different modes. An additional conclusion from the analysis is that increase of the aspect ratio results in red shifting of the LSPR, what is also accompanied by a higher local field enhancement.

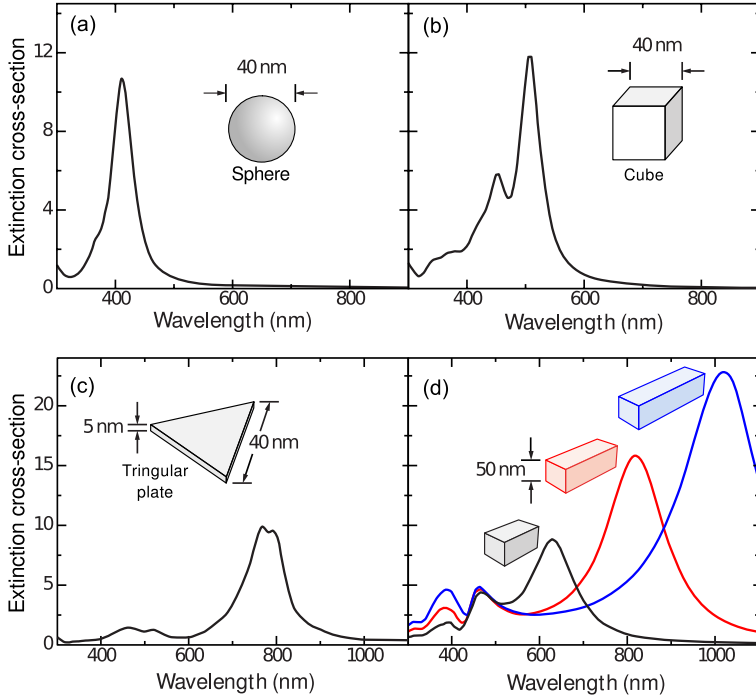


Figure 1.5: Numerically calculated extinction spectra of Ag nanostructures of varying shapes (a-c) and different sizes (d). Figure adapted from [28].

For arbitrarily sized and shaped particle one has to resort to numerical methods in order to calculate the optical response. Both experimental results and theoretical calculations agree with the trend resulting from the quasi-static analysis – the LSPR redshifts for structures with shapes diverting more from a sphere, as seen in figure 1.5.

1.3.5 Plasmonic materials

The choice of the optimal material for plasmonic applications is an important issue, as it is one of the factors determining the maximum achievable local field enhancement. For a sphere in the quasi-static approximation this is given by $\frac{\epsilon_1}{\epsilon_2}$ [29]. That is why noble metals (Ag, Au, Cu) are usually used for this purpose with their low γ , resulting in low ϵ_2 compared to ϵ_1 . An additional practical argument is their high chemical stability, preventing deterioration of the optical properties due to corrosion, and facilitating easier processing in the case of top-down fabrication. Metals, however, have high ω_p , what makes the tuning of the LSPR into the infrared complicated. This is why also other materials are consid-

1 Introduction

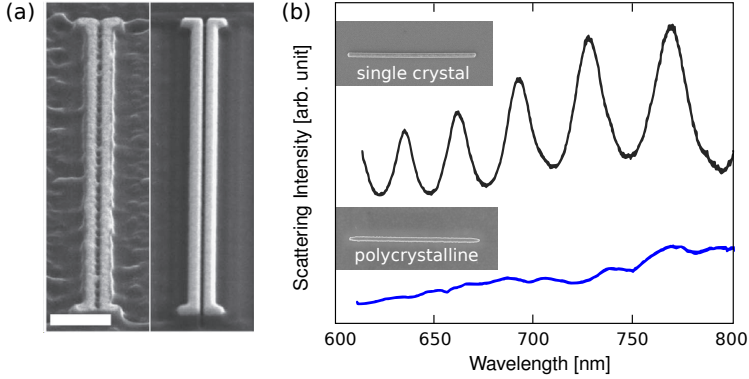


Figure 1.6: Effect of crystallinity of metal nanostructures on surface roughness (a) and optical spectra (b). Figures adapted from [31, 32].

ered. They include conductive nitrides (TiN), doped conductive oxides ($\text{In}_2\text{O}_3:\text{SnO}_2, \text{ZnO}:\text{Al}, \text{ZnO}:\text{Ga}$ [29]) for the near infrared, and doped semiconductors for the far infrared applications. A similar analysis holds for PSPs, for which an important figure of merit is the ratio of the real and imaginary parts of the wavevector, which is approximately equal to $\frac{\epsilon_1^2}{\epsilon_2}$ [29, 30]. Extending further the wavelength range into the infrared and finding suitable low-loss semi-metallic or semiconducting compounds is certainly an important challenge for materials science.

1.3.6 Effects of material quality and crystallinity

If one considers real metallic nanostructures, the importance of good quality of the used metal cannot be overrated. Too much impurities or excess scattering at grain boundaries cause additional losses. It is a reasonable approximation to assume that every contribution to the losses is independent and adds linearly to the intrinsic collision frequency $\gamma = \gamma_0 + \sum \gamma_i$. This is also known as Matthiessen's rule. Single crystal materials of high purity are desired if one wants to obtain the highest possible field enhancements. What is more, it has been demonstrated that in the case of top-down fabricated structures, polycrystalline materials are less reliable in terms of fabrication reproducibility and cause additional losses due to the scattering of electromagnetic field at their rough surfaces [31, 32]. Both effects are shown in figure 1.6. Due to crystallographic selectivity of chemical etching or FIB-milling, single crystal materials can be patterned into shapes with atomically smooth surfaces eliminating this problem. Their etch or sputtering rates are also more stable, causing better reproducibility of the obtained nanostructures. In this context, epitaxial NCs investigated in this thesis are also superior to traditional polycrystalline lithographic nanostructures due to naturally occurring atomic-level smoothness of their facets.

1.3.7 Effects of dielectric environment

Embedding a metal nanostructure in a dielectric medium will result in the redshifting of its resonance wavelength. In the quasi-static regime the denominator of the polarizability α vanishes approximately for $\epsilon_1 = -2\epsilon_m$, so with increasing ϵ_m this condition will be met for more negative ϵ_1 , that is at lower frequencies. In experimental situations the metallic structures are very often supported on a substrate, so their dielectric environment is non-uniform. To estimate the influence of the substrate one can assume that the whole structure is embedded in a medium with effective dielectric function being an average of the dielectric functions of the substrate and air. This is a rather crude approximation and can be further refined by weighing the dielectric function with the ratio of the substrate contact area and surface area [33]. Introduction of a substrate has also an additional effect, it reduces the symmetry of a particle causing additional mode splitting. Usually the mode with polarization parallel to the substrate has a lower energy than the one polarized perpendicular [34].

1.3.8 Complex structures

It is usually desirable to obtain as high local field enhancements E_{loc}/E_{inc} , as possible. Engineering the shape of the nanostructures is an effective approach to do this. To obtain even higher E_{loc}/E_{inc} , one can resort to complex metal nanoparticle arrangements, for example dimers. Such structures, often called optical nanoantennas as they resemble "classical" antennas used for radiofrequencies, offer enhancement boosts well above one order of magnitude [35]. A typical example of such a nanoantenna is a pair of aligned metal nanospheres, nanorods or prisms (shown in figure 1.7a), which is an optical analog of a dipole antenna. The nanorods are separated by a small gap, ideally less than 10 nm. This proves the profound importance of reliable and precise fabrication or positioning techniques, that were discussed in section 1.2.3. When two metallic structures are brought into close proximity, their SPRs interact and hybridize. For two identical metal nanostructures with dipole resonance frequency ω_0 two hybridized modes are created, one symmetric with eigenfrequency $\omega_+ < \omega_0$, and one antisymmetric, where $\omega_- > \omega_0$ as presented in figure 1.7b. This phenomenon is sometimes called plasmon hybridization [36], where in the simplest case one bonding, and one anti-bonding orbital are formed. Probably in the context of plasmonics it would be more correct to refer to it as coupled-mode theory [37]. Spectral shifts due to plasmon hybridization can be substantial for small gap widths [35], and offer an interesting possibility of fine tuning the SPR wavelength if the gap can be controlled precisely enough.

1 Introduction

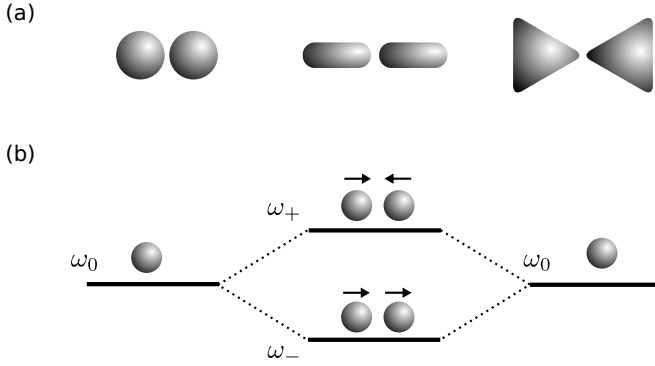


Figure 1.7: Typical optical nanoantennas configurations (a) and illustration of bright (ω_-) and dark (ω_+) LSPR modes arising due to coupling of two metal nanostructures (b).

1.4 Semiconductor quantum dots

Though not directly related to the topic of metal nanostructures, semiconductor epitaxial QDs require some introduction, as they will serve as the emitters used throughout the thesis. QDs are small structures that have dimensions at least comparable to the bulk exciton Bohr radius, being in that sense zero dimensional (0D) structures. Semiconductor QDs gained broad interest after it was predicted that QD-based lasers will be less temperature sensitive [38] and will have smaller threshold currents [39]. Initial focus was on top-down fabricated QDs, however they were generally of low optical quality due to processing defects. In 1985 SK InAs/GaAs QDs were grown for the first time by MBE [40]. It turned out that such dots have superior optical quality, and at low temperatures they exhibit extremely sharp, atomic-like transitions. Not only are they used as gain medium for high-performance semiconductor lasers, but also as basic building block for many quantum-functional devices including single photon sources and qubits.

1.5 Metal quantum dots

Even very small metal clusters in the few nm size range can be described with bulk metal dielectric functions if additional losses ($\propto \frac{1}{R}$) are accounted for. In the case of semiconductor QDs of similar size very strong quantization effects are observed. This is due to the high free electron density in the case of metals screening any confinement effects, which are easily observable in the case of semiconductors. Splitting of the energy levels due to quantum size effects can be observed only in the case of extremely small metallic clusters consisting of few atoms, when

the size of the metal particle is less than the Fermi wavelength. Such small clusters can be synthesized chemically with suitable capping agents. This has been demonstrated both for Au [41], as well as Ag [42] and other materials [43, 44]. The metal QDs remain stable in the solution, as well as after drying. They are optically active with quantum efficiency up to 70%, and have a very wide range of emission wavelength, from ultra-violet (UV) (385 nm), in the case of Au₅, to NIR (866 nm) for Au₃₁. This allows to consider fabrication of active plasmonic structures utilizing metals both as gain and guiding medium.

1.6 Physical and chemical properties

One very important physical property that is a function of the metal particle size is its melting point [45, 46]. For particle sizes smaller than few tens of nm one observes so-called melting point depression. This effect is significant and can amount to hundreds of K. In fact, a size-dependent melting point is a phenomenon observed also for other materials. It has no connection to the presence or lack of metallic conduction. This effect is important for example in context of the thermal stability of metal nanostructures under high excitation powers or for thermo-optical metal nanoparticle-based information storage. Other important properties that depend on the size include chemical stability and reactivity, manifesting themselves in much higher abundance of clusters consisting of defined numbers of atoms (so-called magic numbers) [47], size dependent toxicity of metal nanoparticles [48] or catalytic activity [49].

1.7 Applications

The applications of metal nanostructures and nanoparticles are very rich. Here, the author will concentrate mostly on those relating to plasmonics due to the topic of the thesis. This, however, does not exhaust all the possibilities. Metal nanoparticles, for example, are interesting for applied sciences, because they can be used as effective germicidal agents, they possess interesting tribological properties and are effective catalysts. On the more optical side, arrays of metal nanostructure can act for example as metamaterials with negative index of refraction.

1.7.1 Emission enhancement

In general, the radiative decay rate Γ of any emitter depends on its dielectric environment, even if one excludes any interactions modifying the confinement or electronic structure of that emitter. It has been first proposed and observed by Purcell [50] in the context of magnetic resonance transitions in solids. This effect can be explained on the grounds of classical electrodynamics if one considers the radiative decay

1 Introduction

of a dipole. Intuitively one can understand the modification of the intrinsic decay rate Γ_0 as an effect of the field emitted from the dipole polarizing its environment or reflecting from some nearby structure and interfering constructively or destructively with further emission from the source. It can be modeled classically with the equation [51]

$$\ddot{\mathbf{p}} + \Gamma_0 \dot{\mathbf{p}} + \omega_0 \mathbf{p} = \frac{e^2}{m} \mathbf{E}_{loc}(\mathbf{r}_0),$$

where ω_0 is the free space resonance frequency of the dipole and $E_{loc}(\mathbf{r}_0)$ is the local field at the position of the dipole. Provided that $\Gamma_0 < 2\omega_0$ the dipole moment decays in time like $\propto \exp(-\Gamma t)$ and the normalized decay rate is given by

$$\frac{\Gamma}{\Gamma_0} = 1 + \frac{6\pi\epsilon_0}{k^3} \text{Im} [\mathbf{u}^* \mathbf{S}(\mathbf{r}, \mathbf{r}_0, \omega_0) \mathbf{u}],$$

where \mathbf{u} is an unit vector such that $\mathbf{p} = p\mathbf{u}$, and \mathbf{S} is the field susceptibility tensor defining the local field in terms of the dipole moment $\mathbf{E}_{loc}(\mathbf{r}) = \mathbf{S}(\mathbf{r}, \mathbf{r}_0, \omega_0) \mathbf{p}(\mathbf{r}_0)$. The tensor \mathbf{S} is connected with Green's function by the following equation $\mathbf{G}(\mathbf{r}, \mathbf{r}_0, \omega_0) = \mathbf{G}_0(\mathbf{r}, \mathbf{r}_0, \omega_0) + \mathbf{S}(\mathbf{r}, \mathbf{r}_0, \omega_0)$ [51], i.e. it represents the contribution of the inhomogeneous dielectric environment.

In the quantum treatment of this problem one can use Fermi's golden rule to derive [52]

$$\Gamma = \frac{2\omega_0}{e\hbar\epsilon_0} |\mu|^2 \rho_u(\mathbf{r}_0, \omega_0),$$

where $|\mu|$ is the matrix element for the considered transition, and ρ_u is the local density of photonic states for light polarized along \mathbf{u}

$$\rho_u = \frac{6\omega_0}{\pi c^2} (\mathbf{u}^* \text{Im} [\mathbf{G}(\mathbf{r}_0, \mathbf{r}_0, \omega_0)] \mathbf{u}).$$

Taking into account that $\mathbf{G} = \mathbf{G}_0 + \mathbf{S}$, one can reconcile the quantum and classical normalized radiative rate. Classical electrodynamics does not, however, account correctly for the resonant frequency shift $\Delta\omega_0$ and for the phenomenon of strong coupling. Moreover it does not include emission saturation effects that are intrinsic to real, that is quantum emitters.

The analytical calculation of the photonic density of states ρ is in general difficult, if not an impossible task. One can resort to numerical calculations [53] or use the following heuristics to understand this concept. The density of states is higher in regions of high concentration of electromagnetic field, namely $\rho \sim E_{loc}/E_{inc}^2$ [54]. Objects that support such high field regions and are thus used to engineer radiative decays include resonators, photonic microcavities and of course all kinds of metallic nanostructures.

In real experimental situations one has to consider also nonradiative losses of the emitter, as well as the collection efficiency of light. The rate

of photon detection of a quantum emitter can be expressed as [55]

$$D = \kappa\eta \frac{\Gamma_{ex}}{1 + \frac{\Gamma_{ex}}{\Gamma}},$$

where κ is the collection efficiency defined by the experimental setup and directional emission pattern, $\Gamma = \Gamma_{rad} + \Gamma_{nrad}$ is the total relaxation rate including radiative and nonradiative processes, $\Gamma_{ex} = \sigma I_{ex}$ is the excitation rate depending on the power of incident light and on the absorption cross-section of the emitter and $\eta = \frac{\Gamma_{rad}}{\Gamma}$ is the quantum efficiency. Obviously one wants to maximize D . In order to do so, one has to optimize Γ_{rad} keeping the nonradiative losses at minimum. This usually means finding an optimum separation from the surface of the used metal nanostructure, because direct proximity of the metal surface can induce nonradiative recombination due to coupling to higher plasmonic dark modes, as well as because of modification of the electronic structure of the emitter and presence of defect states. The second issue is of profound importance in the case of semiconductor QDs, because of their moderate confinement potential depth, as well as high sensitivity to surface states and surface recombination. To circumvent this problem one can consider utilizing different passivation treatments of the semiconductor and metal surface or additional passivating layers between them [56]. Additional enhancement, in the case of optical pumping, can be obtained due to the higher \mathbf{E}_{loc} at the excitation wavelength increasing Γ_{ex} for fixed pumping power. Furthermore, if one uses rationally designed nanoantennas D can be increased by controlling the directional distribution of the emitted light what can greatly increase the collection efficiency. All above-mentioned contributions to the overall brightness of an emitter are presented graphically in figure 1.8.

It has been assumed so far, that the emitter can be approximated by a point dipole, what effectively means that it is much smaller than any characteristic dimension of the confined electromagnetic mode it is interacting with. Such assumption is reasonable outside of the realm of plasmonics even for relatively large emitters such as SK QDs. Since metallic nanostructures support electromagnetic modes confined at deep subwavelength scales, this assumption may not be valid anymore. Indeed, it was demonstrated experimentally that the dipole approximation does not hold for semiconductor QDs coupled to PSPs in a thin metal film [57]. In this case additional effect modifies the emission rate

$$\Gamma = \Gamma_{dip} + \Xi,$$

where Γ_{dip} is the familiar point-like dipole contribution proportional to the transition dipole moment μ and the local density of states. Ξ is the mesoscopic contribution proportional to the electromagnetic field gradient inside of the emitter and higher order (electric quadrupole and magnetic dipole) transition moments. This additional effect can both

1 Introduction

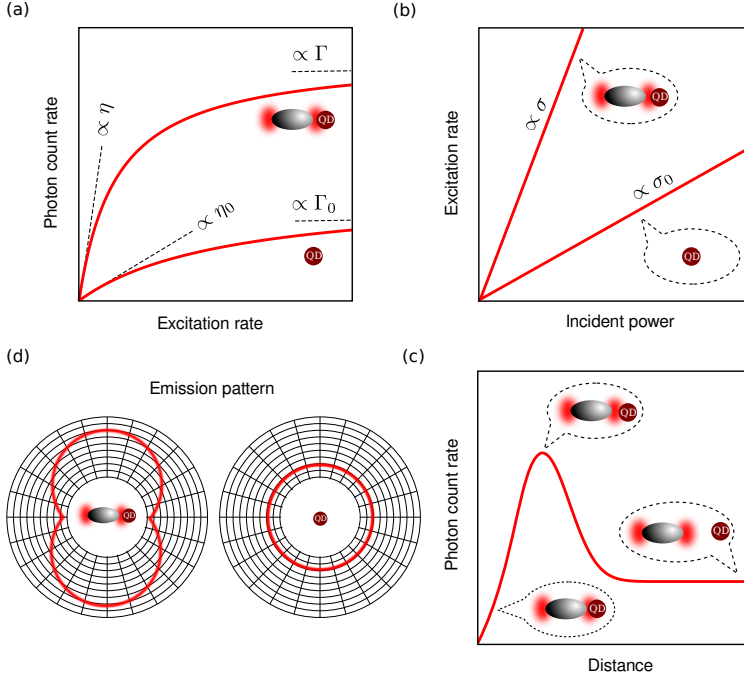


Figure 1.8: Different emission enhancement mechanisms. Improvement of quantum efficiency η and saturation emission rate (a), improvement of absorption cross-section (b) and improvement of collection efficiency κ due to emission pattern modification (c). At all times careful balance between emission enhancement and quenching has to be maintained, what requires extremely precise QD to metal nanoparticle distance control (d).

increase and decrease the emission rate depending on the orientation of the QD. Breaking of the dipole approximation offers an additional degree of freedom and additional possibilities when designing hybrid QD-metal nanostructures. Moreover, one could use it to observe radiative transitions that are normally "dipole forbidden" due to symmetry considerations.

1.7.2 Active plasmonics

By combining gain or nonlinear media with metallic nanostructures, one can build many active devices providing a route to photonic integrated circuits with integration scales that could rival those of CMOS technology. Embedding metallic nanostructures in a gain medium can compensate for the resistive losses of the metal. In the case of LSPRs this would result in greater polarizability, and in the case of extended structures it would enhance the propagation length of PSPs. For high enough gain, the polarizability α in the quasi-static approximation diverges to infinity, when the denominator $\epsilon + 2\epsilon_m$ equals 0. Obviously infinite polarizability

is not physical. One would expect that for a certain critical gain value lasing action will occur. Such a plasmonic laser, called spaser, has been proposed and investigated theoretically in [58]. It has been demonstrated for the first time in [59]. The investigated structure consisted of small, 14 nm diameter Au nanoparticles, surrounded by a fluorescent dye doped SiO_2 shell of around 44 nm diameter and lased around 520 nm. So indeed the whole structure had subwavelength dimensions, being probably the smallest laser ever. Amplification of PSPs was also demonstrated in a thin metallic film embedded in a dye-doped polymer [60] and for other configurations [61].

Generating light is not the only possible application of the spaser, it can also act as an optical analog of a transistor, offering in theory extremely high frequencies of operation [62]. A different implementation of a plasmonic optical transistor has been also proposed [63] operating at the single photon level. Another interesting possibility of active plasmonic devices is combining metal nanostructures with nonlinear media. Such hybrids can exhibit bistable behaviour and facilitate all-optical ultrafast tuning of the resonance wavelength. One particularly interesting example is a metallic nanowire antenna with a semiconducting material in the gap, that can be tuned over a wide wavelength range by injecting electron-hole pairs in the semiconductor [64, 65]. Propagation of plasmons and the LSPR wavelength can also be controlled by other, non-optical, means using for example temperature or electric field [66, 67].

1.7.3 Plasmonic sensing

Metal nanostructures have many applications in the field of sensing, especially bio-sensing. Good reviews of the topic can be found for example in [68–70]. In its simplest form plasmonic sensors can be based on the influence of the local refractive index on the wavelength of the LSPR or the coupling of a PSP to external radiation. In this case, some kind of surface functionalization is required to distinguish the analyte from other substances. As discussed in previous sections, plasmonic nanostructures support very strong local fields that can enhance the luminescence. In favourable cases single-molecule detection is possible [71]. This means that with proper functionalization extreme sensitivities for luminescent molecule detection could be achieved. Another important sensing mechanism is SERS, that is also based on local field enhancement. It scales more favourably ($\propto E_{loc}^4$) than luminescence enhancement ($\propto E_{loc}^2$), so huge gains in the Raman cross-section up to 10^{15} are attainable with optimized SERS structures enabling single molecule sensitivity [72]. Moreover, Raman spectroscopy is intrinsically chemically sensitive and can be combined with scanning probe techniques, offering spatially resolved information on chemical composition or strain [73]. In sensing applications enhancement of radiative processes is not always desirable. Certain studies of the structure of large molecules like proteins require

1 Introduction

fluorescence quenchers and small metal clusters are good candidates for this application as well [74]. Attaching a fluorescent marker with known properties at the site of interest and the quencher at another site and measuring the fluorescence lifetime can yield information on their spatial separation. Yet another interesting application in the field of biosensing is based on the high light scattering cross-section of metal nanoparticles, which after proper functionalization can be used as *in-vivo* markers sensitive to cancer cells [75].

1.7.4 Quantum dot formation

There is one additional interesting application of metal nanoparticles, or more precisely epitaxial metal nanocrystals or nanometer sized metal droplets, which has also been investigated in this thesis. Such metal nanostructures can be used as precursors for formation of epitaxial III-V QDs in MBE, as well as metalorganic vapour phase epitaxy (MOVPE). Usually one relies on strain to grow high-quality SK QDs. This approach has, however, its limitations. For example, in the case of InAs growth on (111)A oriented GaAs it is not possible to obtain good quality strained QDs, instead dislocation form instantly. It is also desirable to form QDs in strain-free systems like AlGaAs/GaAs that does not support SK growth. These issues can be solved if first one deposits group-III material in order to form small metal droplets or nanocrystals, which afterwards are converted to III-V QDs under group-V flux. This process is called DE, and has been invented by Koguchi and co-workers [76]. Interestingly, the first demonstration of SK precedes DE QDs only by five years, however it took considerably more time to obtain high optical quality QDs by this method. DE allows finer control over the density of QDs, especially in the regimes necessary for single QD investigations [77], and also can be used to synthesize more complex low dimensional structures like single and multiple quantum rings [78].

1.8 Summary

In this chapter the fabrication and synthesis methods, properties, as well as applications of metal nanostructures were described. It is by no means a complete review, but the discussed topics like growth, self-assembly of metal NCs, shape, size and dielectric environment effects on the LSPR wavelength, as well as on the radiative emission rate shall serve as a basis for interpreting and understanding the original research results presented in this thesis.

References

- [1] <http://www.britishmuseum.org>.

- [2] M. Faraday, "The Bakerian Lecture: Experimental Relations of Gold (and Other Metals) to Light," *Philosophical Transactions of the Royal Society of London*, vol. 147, p. 145, 1857.
- [3] G. Mie, "Beiträge zur Optik trüber Medien, speziell kolloidaler Metallösungen," *Annalen der Physik*, vol. 330, p. 377, 1908.
- [4] K. H. Drexhage, "Influence of a dielectric interface on fluorescence decay time," *Journal of Luminescence*, vol. 1–2, p. 693, 1970.
- [5] M. Fleischmann, P. Hendra, and A. McQuillan, "Raman spectra of pyridine adsorbed at a silver electrode," *Chemical Physics Letters*, vol. 26, p. 163, 1974.
- [6] T. W. Ebbesen, H. J. Lezec, H. F. Ghaemi, T. Thio, and P. A. Wolff, "Extraordinary optical transmission through sub-wavelength hole arrays," *Nature*, vol. 391, p. 667, 1998.
- [7] M. I. Stockman, "Nanoplasmonics: The physics behind the applications," *Physics Today*, vol. 64, p. 39, 2011.
- [8] Y. Xia and N. J. Halas, "Shape-Controlled Synthesis and Surface Plasmonic Properties of Metallic Nanostructures," *MRS Bulletin*, vol. 30, p. 338, 2005.
- [9] M. Rycenga, C. M. Cobley, J. Zeng, W. Li, C. H. Moran, Q. Zhang, D. Qin, and Y. Xia, "Controlling the Synthesis and Assembly of Silver Nanostructures for Plasmonic Applications," *Chemical Reviews*, vol. 111, p. 3669, 2011.
- [10] P. Martin, *Handbook of Deposition Technologies for Films and Coatings: Science, Applications and Technology*. Elsevier, 2009.
- [11] Lüth, H., *Solid Surfaces, Interfaces and Thin Films*. Springer, 2010.
- [12] A. E. Grigorescu and C. W. Hagen, "Resists for sub-20-nm electron beam lithography with a focus on HSQ: state of the art," *Nanotechnology*, vol. 20, p. 292 001, 2009.
- [13] S. Reyntjens and R. Puers, "A review of focused ion beam applications in microsystem technology," *Journal of Micromechanics and Microengineering*, vol. 11, p. 287, 2001.
- [14] P. Mühlischlegel, H.-J. Eisler, O. J. F. Martin, B. Hecht, and D. W. Pohl, "Resonant Optical Antennas," *Science*, vol. 308, p. 1607, 2005.
- [15] <http://www.mapperlithography.com>.
- [16] S. J. Randolph, J. D. Fowlkes, and P. D. Rack, "Focused, Nanoscale Electron-Beam-Induced Deposition and Etching," *Critical Reviews in Solid State and Materials Sciences*, vol. 31, p. 55, 2006.
- [17] W. F. van Dorp and C. W. Hagen, "A critical literature review of focused electron beam induced deposition," *Journal of Applied Physics*, vol. 104, 081301, p. 081 301, 2008.

1 Introduction

- [18] A. Dhawan, M. Gerhold, A. Madison, J. Fowlkes, P. E. Russell, T. Vo-Dinh, and D. N. Leonard, "Fabrication of nanodot plasmonic waveguide structures using FIB milling and electron beam-induced deposition," *Scanning*, vol. 31, p. 139, 2009.
- [19] S. Graells, S. Aćimović, G. Volpe, and R. Quidant, "Direct Growth of Optical Antennas Using E-Beam-Induced Gold Deposition," *Plasmonics*, vol. 5, p. 135, 2010.
- [20] S. Y. Chou, P. R. Krauss, and P. J. Renstrom, "Imprint Lithography with 25-Nanometer Resolution," *Science*, vol. 272, p. 85, 1996.
- [21] B. D. Lucas, J.-S. Kim, C. Chin, and L. J. Guo, "Nanoimprint Lithography Based Approach for the Fabrication of Large-Area, Uniformly-Oriented Plasmonic Arrays," *Advanced Materials*, vol. 20, p. 1129, 2008.
- [22] T. Ishikawa, S. Kohmoto, and K. Asakawa, "Site control of self-organized InAs dots on GaAs substrates by in situ electron-beam lithography and molecular-beam epitaxy," *Applied Physics Letters*, vol. 73, p. 1712, 1998.
- [23] A. Urbańczyk, G. J. Hamhuis, and R. Nötzel, "Strain-driven alignment of In nanocrystals on InGaAs quantum dot arrays and coupled plasmon-quantum dot emission," *Applied Physics Letters*, vol. 96, p. 113101, 2010.
- [24] E. J. Zeman and G. C. Schatz, "An accurate electromagnetic theory study of surface enhancement factors for silver, gold, copper, lithium, sodium, aluminum, gallium, indium, zinc, and cadmium," *The Journal of Physical Chemistry*, vol. 91, p. 634, 1987.
- [25] S. Maier, *Plasmonics: fundamentals and applications*. Springer, 2007.
- [26] U. Kreibig and M. Vollmer, *Optical Properties of Metal Clusters*. Springer, 1995.
- [27] A. Wokaun, J. P. Gordon, and P. F. Liao, "Radiation Damping in Surface-Enhanced Raman Scattering," *Physical Review Letters*, vol. 48, p. 957, 1982.
- [28] X. Lu, M. Rycenga, S. E. Skrabalak, B. Wiley, and Y. Xia, "Chemical Synthesis of Novel Plasmonic Nanoparticles," *Annual Review of Physical Chemistry*, vol. 60, p. 167, 2009.
- [29] P. R. West, S. Ishii, G. V. Naik, N. K. Emani, V. M. Shalaev, and A. Boltasseva, "Searching for better plasmonic materials," *Laser Photonics Reviews*, vol. 4, p. 795, 2010.
- [30] H. Raether, *Surface plasmons on smooth and rough surfaces and on gratings*. Springer, 1988.

- [31] H. Ditlbacher, A. Hohenau, D. Wagner, U. Kreibig, M. Rogers, F. Hofer, F. R. Aussenegg, and J. R. Krenn, "Silver Nanowires as Surface Plasmon Resonators," *Physical Review Letters*, vol. 95, p. 257 403, 2005.
- [32] J.-S. Huang, V. Callegari, P. Geisler, C. Braning, J. Kern, J. C. Prangnsma, X. Wu, T. Feichtner, J. Ziegler, P. Weinmann, M. Kamp, A. Forchel, P. Biagioni, U. Sennhauser, and B. Hecht, "Atomically flat single-crystalline gold nanostructures for plasmonic nanocircuitry," *Nature Communications*, vol. 1, p. 150, 2010.
- [33] G. Xu, Y. Chen, M. Tazawa, and P. Jin, "Influence of dielectric properties of a substrate upon plasmon resonance spectrum of supported Ag nanoparticles," *Applied Physics Letters*, vol. 88, 043114, p. 043 114, 2006.
- [34] S. Zhu, T. P. Chen, Z. H. Cen, E. S. M. Goh, S. F. Yu, Y. C. Liu, and Y. Liu, "Split of surface plasmon resonance of gold nanoparticles on silicon substrate: a study of dielectric functions," *Optics Express*, vol. 18, p. 21 926, 2010.
- [35] P. Biagioni, J.-S. Huang, and B. Hecht, "Nanoantennas for visible and infrared radiation," *Reports on Progress in Physics*, vol. 75, p. 024 402, 2012.
- [36] E. Prodan, C. Radloff, N. J. Halas, and P. Nordlander, "A Hybridization Model for the Plasmon Response of Complex Nanostructures," *Science*, vol. 302, p. 419, 2003.
- [37] G. Sun and J. Khurgin, "Coupled-Mode Theory of Plasmonic Field Enhancement in Complex Metal Nanostructures," in *Photonic Metamaterials and Plasmonics*, Optical Society of America, 2010, MTuB2.
- [38] Y. Arakawa and H. Sakaki, "Multidimensional quantum well laser and temperature dependence of its threshold current," *Applied Physics Letters*, vol. 40, p. 939, 1982.
- [39] M. Asada, Y. Miyamoto, and Y. Suematsu, "Gain and the threshold of three-dimensional quantum-box lasers," *Quantum Electronics, IEEE Journal of*, vol. 22, p. 1915, 1986.
- [40] L. Goldstein, F. Glas, J. Y. Marzin, M. N. Charasse, and G. L. Roux, "Growth by molecular beam epitaxy and characterization of InAs/GaAs strained-layer superlattices," *Applied Physics Letters*, vol. 47, p. 1099, 1985.
- [41] J. Zheng, C. Zhang, and R. M. Dickson, "Highly Fluorescent, Water-Soluble, Size-Tunable Gold Quantum Dots," *Physical Review Letters*, vol. 93, p. 077 402, 2004.
- [42] L. Shang and S. Dong, "Facile preparation of water-soluble fluorescent silver nanoclusters using a polyelectrolyte template," *Chemical Communications*, vol. 1, p. 1, 2008.

1 Introduction

- [43] H. Zhang, X. Huang, L. Li, G. Zhang, I. Hussain, Z. Li, and B. Tan, "Photoreductive synthesis of water-soluble fluorescent metal nanoclusters," *Chemical Communications*, vol. 48, p. 1, 2012.
- [44] S.-I. Tanaka, J. Miyazaki, D. K. Tiwari, T. Jin, and Y. Inouye, "Fluorescent Platinum Nanoclusters: Synthesis, Purification, Characterization, and Application to Bioimaging," *Angewandte Chemie International Edition*, vol. 50, p. 431, 2011.
- [45] T. Castro, R. Reifenger, E. Choi, and R. P. Andres, "Size-dependent melting temperature of individual nanometer-sized metallic clusters," *Physical Review B*, vol. 42, p. 8548, 1990.
- [46] Q. Jiang, S. Zhang, and M. Zhao, "Size-dependent melting point of noble metals," *Materials Chemistry and Physics*, vol. 82, p. 225, 2003.
- [47] W. D. Knight, K. Clemenger, W. A. de Heer, W. A. Saunders, M. Y. Chou, and M. L. Cohen, "Electronic Shell Structure and Abundances of Sodium Clusters," *Physical Review Letters*, vol. 52, p. 2141, 1984.
- [48] Y. Pan, S. Neuss, A. Leifert, M. Fischler, F. Wen, U. Simon, G. Schmid, W. Brandau, and W. Jähnen-Dechent, "Size-Dependent Cytotoxicity of Gold Nanoparticles," *Small*, vol. 3, p. 1941, 2007.
- [49] T. K. Sau, A. Pal, and T. Pal, "Size Regime Dependent Catalysis by Gold Nanoparticles for the Reduction of Eosin," *The Journal of Physical Chemistry B*, vol. 105, p. 9266, 2001.
- [50] N. Bloembergen, E. M. Purcell, and R. V. Pound, "Relaxation Effects in Nuclear Magnetic Resonance Absorption," *Physical Review*, vol. 73, p. 679, 1948.
- [51] E. Fort and S. Grésillon, "Surface enhanced fluorescence," *Journal of Physics D: Applied Physics*, vol. 41, p. 013001, 2008.
- [52] L. Novotny and B. Hecht, *Principles of nano-optics*. Cambridge University Press, 2006.
- [53] Y. Chen, T. R. Nielsen, N. Gregersen, P. Lodahl, and J. Mørk, "Finite-element modeling of spontaneous emission of a quantum emitter at nanoscale proximity to plasmonic waveguides," *Physical Review B*, vol. 81, p. 125431, 2010.
- [54] G. C. des Francs, C. Girard, J.-C. Weeber, and A. Dereux, "Relationship between scanning near-field optical images and local density of photonic states," *Chemical Physics Letters*, vol. 345, p. 512, 2001.
- [55] J. Wenger, D. Gérard, J. Dintinger, O. Mahboub, N. Bonod, E. Popov, T. W. Ebbesen, and H. Rigneault, "Emission and excitation contributions to enhanced single molecule fluorescence by gold nanometric apertures," *Optics Express*, vol. 16, p. 3008, 2008.

- [56] L. Meiners and H. Wieder, “Semiconductor surface passivation,” *Materials Science Reports*, vol. 3, p. 139, 1988.
- [57] M. L. Andersen, S. Stobbe, A. S. Sorensen, and P. Lodahl, “Strongly modified plasmon-matter interaction with mesoscopic quantum emitters,” *Nature Physics*, vol. 7, p. 215, 2011.
- [58] D. J. Bergman and M. I. Stockman, “Surface Plasmon Amplification by Stimulated Emission of Radiation: Quantum Generation of Coherent Surface Plasmons in Nanosystems,” *Physical Review Letters*, vol. 90, p. 027402, 2003.
- [59] M. A. Noginov, G. Zhu, A. M. Belgrave, R. Bakker, V. M. Shalaev, E. E. Narimanov, S. Stout, E. Herz, T. Suteewong, and U. Wiesner, “Demonstration of a spaser-based nanolaser,” *Nature*, vol. 460, p. 1110, 2009.
- [60] M. A. Noginov, G. Zhu, M. Mayy, B. A. Ritzo, N. Noginova, and V. A. Podolskiy, “Stimulated Emission of Surface Plasmon Polaritons,” *Physical Review Letters*, vol. 101, p. 226806, 2008.
- [61] P. Berini and I. De Leon, “Surface plasmon-polariton amplifiers and lasers,” *Nature Photonics*, vol. 6, p. 16, 2012.
- [62] M. I. Stockman, “The spaser as a nanoscale quantum generator and ultrafast amplifier,” *Journal of Optics*, vol. 12, p. 024004, 2010.
- [63] D. E. Chang, A. S. Sorensen, E. A. Demler, and M. D. Lukin, “A single-photon transistor using nanoscale surface plasmons,” *Nature Physics*, vol. 3, p. 807, 2007.
- [64] N. Large, M. Abb, J. Aizpurua, and O. L. Muskens, “Photoconductively Loaded Plasmonic Nanoantenna as Building Block for Ultracompact Optical Switches,” *Nano Letters*, vol. 10, p. 1741, 2010.
- [65] M. Abb, P. Albella, J. Aizpurua, and O. L. Muskens, “All-Optical Control of a Single Plasmonic Nanoantenna-ITO Hybrid,” *Nano Letters*, vol. 11, p. 2457, 2011.
- [66] K. F. MacDonald and N. I. Zheludev, “Active plasmonics: current status,” *Laser & Photonics Reviews*, vol. 4, p. 562, 2010.
- [67] J. Berthelot, A. Bouhelier, C. Huang, J. Margueritat, G. Colas-des-Francis, E. Finot, J.-C. Weeber, A. Dereux, S. Kostcheev, H. I. E. Ahrach, A.-L. Baudrion, J. Plain, R. Bachelot, P. Royer, and G. P. Wiederrecht, “Tuning of an Optical Dimer Nanoantenna by Electrically Controlling Its Load Impedance,” *Nano Letters*, vol. 9, p. 3914, 2009.
- [68] J. Homola, “Surface Plasmon Resonance Sensors for Detection of Chemical and Biological Species,” *Chemical Reviews*, vol. 108, p. 462, 2008.

- [69] K. A. Willets and R. P. Van Duyne, "Localized Surface Plasmon Resonance Spectroscopy and Sensing," *Annual Review of Physical Chemistry*, vol. 58, p. 267, 2007.
- [70] K. M. Mayer and J. H. Hafner, "Localized Surface Plasmon Resonance Sensors," *Chemical Reviews*, vol. 111, p. 3828, 2011.
- [71] H. Rigneault, J. Capoulade, J. Dintinger, J. Wenger, N. Bonod, E. Popov, T. W. Ebbesen, and P.-F. Lenne, "Enhancement of Single-Molecule Fluorescence Detection in Subwavelength Apertures," *Physical Review Letters*, vol. 95, p. 117401, 2005.
- [72] S. Nie and S. R. Emory, "Probing Single Molecules and Single Nanoparticles by Surface-Enhanced Raman Scattering," *Science*, vol. 275, p. 1102, 1997.
- [73] F. De Angelis, G. Das, P. Candeloro, M. Patrini, M. Galli, A. Bek, M. Lazzarino, I. Maksymov, C. Liberale, L. C. Andreani, and E. Di Fabrizio, "Nanoscale chemical mapping using three-dimensional adiabatic compression of surface plasmon polaritons," *Nature Nanotechnology*, vol. 5, p. 67, 2010.
- [74] Y. Cheng, T. Stakenborg, P. Van Dorpe, L. Lagae, M. Wang, H. Chen, and G. Borghs, "Fluorescence Near Gold Nanoparticles for DNA Sensing," *Analytical Chemistry*, vol. 83, p. 1307, 2011.
- [75] X. Qian, X.-H. Peng, D. O. Ansari, Q. Yin-Goen, G. Z. Chen, D. M. Shin, L. Yang, A. N. Young, M. D. Wang, and S. Nie, "In vivo tumor targeting and spectroscopic detection with surface-enhanced Raman nanoparticle tags," *Nature Biotechnology*, vol. 26, p. 83, 2008.
- [76] T. Chikyow and N. Koguchi, "MBE Growth Method for Pyramid-Shaped GaAs Micro Crystals on ZnSe (001) Surface Using Ga Droplets," *Japanese Journal of Applied Physics*, vol. 29, p. L2093, 1990.
- [77] A. Urbańczyk and R. Nötzel, "Low-density InAs QDs with subcritical coverage obtained by conversion of In nanocrystals," *Journal of Crystal Growth*, vol. 341, p. 24, 2012.
- [78] C. Somaschini, S. Bietti, A. Fedorov, N. Koguchi, and S. Sanguinetti, "Growth Interruption Effect on the Fabrication of GaAs Concentric Multiple Rings by Droplet Epitaxy," *Nanoscale Research Letters*, vol. 5, p. 1897, 2010.

2 Sample growth, processing and characterization

In this chapter the author discusses the methods and techniques used throughout his research to grow, process and characterize all investigated samples. Additionally, he discusses some important phenomena influencing the growth of the samples and addresses challenges, as well as possible problems arising when using the introduced techniques.

2.1 Epitaxy

The word epitaxy comes from the greek *epi taxis*, what literally means ordering upon. It is a process by which a crystalline material grows on a substrate, forming a single crystal deposit which has a well defined orientation with respect to this substrate. It includes heteroepitaxy, when the substrate and the deposit are two different materials, as well as homoepitaxy, when one deposits the same material as the substrate. There are many techniques to realize epitaxial growth, they include liquid phase epitaxy, when the deposited material is provided from a melt or solution, vapor phase epitaxy, when the deposit is transported by a vapor containing the desired molecular species, MBE, in case of which a molecular beam condenses on a substrate, and finally solid phase epitaxy, in case of which the epitaxially grown material is initially an amorphous layer on top of the substrates which is subsequently recrystallized.

Epitaxy is an extremely important process from the applications point of view. It enables the fabrication of integrated electronic circuits, semiconductor lasers, light emitting diodes and other optoelectronic components, as well as high-efficiency solar cells. Moreover, it allows to grow thin layers of compounds with the highest achievable purity, as well as to synthesize new thin film materials that cannot be formed by other means. This, in turn, allows to engineer the electrical and optical properties of the deposited materials, what is also known as bandgap engineering. This is illustrated in figure 2.1 which shows the bandgap versus lattice constant for different III-V and IV semiconductors and their alloys. What is more, epitaxy allows to grow different nanostructures such as quantum wells (QWs), quantum wires, and QDs that can be used to observe and utilize quantum size effects. A general overview of epitaxial growth can be found in [1].

2 Sample growth, processing and characterization

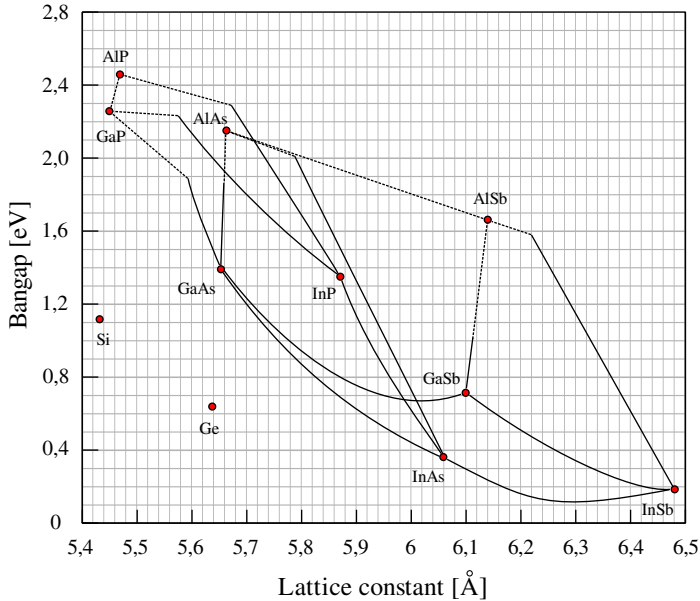


Figure 2.1: Bandgap versus lattice constant relation of different III-V and group IV semiconductors and their alloys. It is evident that only certain combinations are possible for lattice-matched growth. The two technologically most important of them are GaAs/AlGaAs and InP/InGaAs/InAlAs/InGaAsP.

2.1.1 Metalorganic vapor phase epitaxy

MOVPE, in the compound semiconductor context, and Vapor phase epitaxy are the two most important techniques from the commercial and wafer output point of view. Both operate in low vacuum up to atmospheric pressure in the viscous gas flow regime and use volatile chemicals as precursors for the materials to be grown. Common examples of such chemicals are group-III and group-IV alkyls like trimethyl gallium or tertiarybutyl arsine, hydrides like AsH_3 or SiH_4 and halides like SiCl_4 . The precursors are transported through the vapor to be decomposed and react together at the heated surface of the substrate in order to form the desired epitaxial layer. Probably the simplest example of such a reaction is the decomposition of silane to form silicon: $\text{SiH}_{4(g)} \longrightarrow \text{Si}_{(s)} + 2 \text{H}_{2(g)}$. The reactions taking place during the growth can be considerably more complex, especially if larger or more numerous precursors are used, like in case of the deposition of compound semiconductors [2].

A typical MOVPE reactor consists of a quartz tube with an inductively or radiatively heated susceptor on which the substrates are placed, a suitable low vacuum pumping system equipped with a scrubber for neutralizing toxic reaction byproducts and a precise gas and vapor handling system with mass flow or pressure controllers and, in the case of metalor-

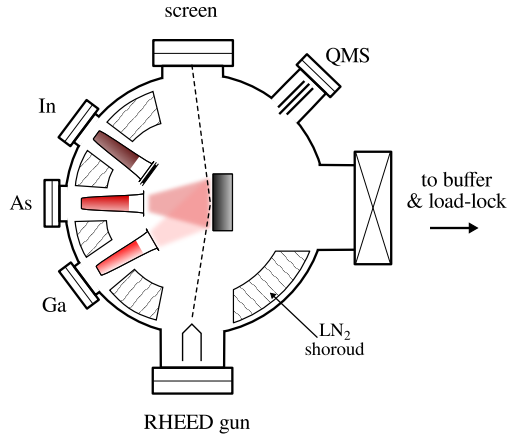


Figure 2.2: Schematic of a MBE growth chamber.

ganic sources, a precise temperature control system for the bubblers. The reactor as a whole is a quite complicated system, but its maintenance is relatively easy, as it does not require high vacuum. The advantages of using MOVPE include high scalability for multiwafer growth, high throughput, the possibility of selective growth, as well as the already mentioned quick maintenance cycle. On the other hand, the disadvantages include usage of toxic gasses and liquids, limited accessibility to the low growth rate regime, as well as problems with the incorporation of impurities coming from the cracked precursors, what can cause high background doping levels. More information on the topic of MOVPE can be found in [2].

2.1.2 MBE

MBE is the epitaxial growth method used by the author to grow all of the samples that were investigated in this thesis. It is an ultra high vacuum (UHV) technique that utilizes molecular beams generated by heating of the source materials to deposit the desired compound on a substrate. Due to the UHV nature of the whole process, using MBE one can achieve record high purities and electrical qualities of the deposited layers and in general background doping is not an issue.

A schematic of a typical III-V MBE growth chamber is presented in figure 2.2. In this case it is an elemental source MBE with the molecular beams being generated using effusion cells. Such cells contain the desired elements which are heated up, and in the case of group III elements kept molten, in order to generate the necessary molecular flux. Its magnitude can be precisely controlled by changing the source temperature, which, once at the desired value, is stabilized by a feedback loop. Additionally, the molecular beams can be rapidly switched on

2 Sample growth, processing and characterization

and off by shutters, what allows to grow layered structures of different materials with atomically abrupt interfaces. In order to achieve the desired base pressure in the 10^{-10} mbar range, various UHV pumps (ion, cryo, Ti sublimation, turbomolecular, or suitable combinations thereof), as well as liquid nitrogen shrouds are used. The growth process and the condition of the substrate surface are usually monitored in-situ by RHEED. It is a very helpful characterization technique for the grower that provides him a lot of information. It can be used for example for growth rate calibration and monitoring with single monolayer (ML) accuracy. Additionally, MBE growth chambers are usually equipped with a quadrupole mass spectrometer for contamination and leak control, as well as for monitoring of chemical processes such as cracking of group V species. MBE is not limited to elemental sources, it can also rely on gaseous or metalorganic sources. In such a case, instead of effusion cells one uses gas injectors often equipped with provisions for plasma generation or thermal cracking of the injected species.

Due to the UHV nature of the MBE process the growth chamber cannot be exposed to the atmosphere every time a sample is introduced. Because of that the MBE systems are equipped with additional buffer and load-lock chambers which are used to prepare and store the substrates, as well as introduce them quickly into the vacuum without generating excessive contamination, respectively. Sometimes the whole system has to be vented to repair it or refill the sources. In such a case after the maintenance procedure, which may take only few hours, the whole system has to be baked, that is heated up to 150–200 °C, for an extended period of time (typically a week) in order to desorb contaminants (mostly H₂O) sticking to the walls of the vacuum chamber. The bakeout allows to achieve again the UHV conditions. This is the biggest disadvantage of MBE, as even the smallest repairs require large amounts of additional time for restoring of the original base pressure. Moreover, after the bakeout a growth rate recalibration is usually necessary, what consumes additional time. From the personal experience of the author the downtime due to maintenance can be reduced to a few weeks per year, however to achieve this, very good planning and extremely careful operation of the system by all users are required. More information about theoretical and practical aspects of MBE can be found in [3].

2.1.3 Growth modes

In general, during heteroepitaxy, depending on the lattice mismatch and the relevant surface and interface energies, one can observe three distinct growth modes, as mentioned already in the previous chapter. This is illustrated in figure 2.3. In case of VW growth 3D crystalline islands form immediately after the deposition starts. For SK growth first a 2D layer forms, and only after a certain critical coverage is reached, 3D islands appear. Finally, in case of the FM mode the growth proceeds

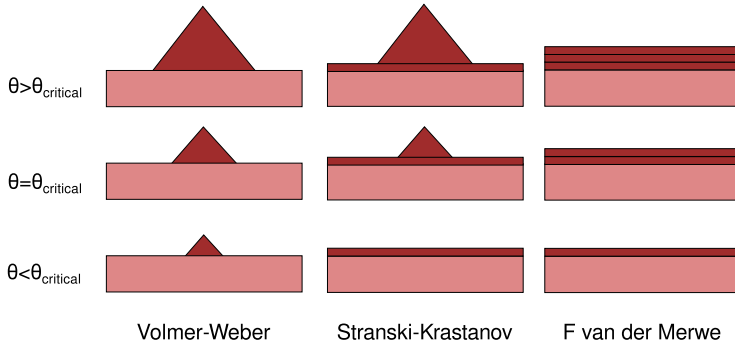


Figure 2.3: Schematic illustration of different growth modes observed during heteroepitaxy.

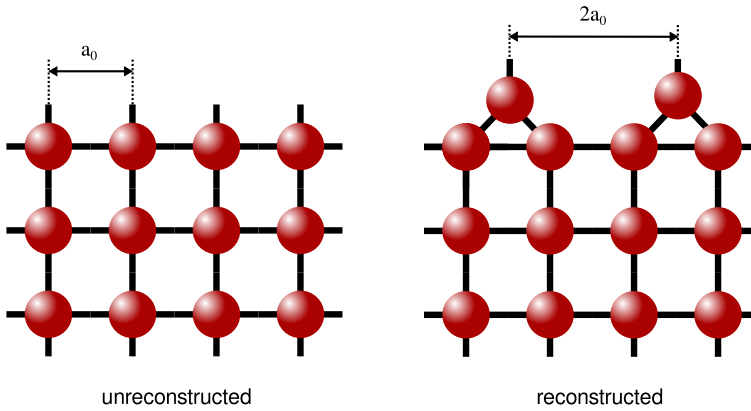


Figure 2.4: Schematic depiction of the surface reconstruction phenomenon. It is evident that a superstructure forms with periodicity lower than that of the bulk material.

layer by layer for an arbitrary coverage. The canonical example of the last growth mode is the deposition of $\text{Al}_x\text{Ga}_{1-x}\text{As}$ on GaAs. This is due to almost perfect lattice matching between those two materials. On the other hand, lattice mismatch often induces SK growth, as in case of $\text{In}_x\text{Ga}_{1-x}\text{As}$ on GaAs, what is the standard way to grow epitaxial semiconductor QDs. It has been already mentioned in the introduction that the SK or VW growth mode can be used to obtain supported metal NCs on semiconductor substrates. An example that is extensively studied in this thesis is the Ag/GaAs material system, which supports the SK growth mode.

2.2 Surface reconstructions

Clean surfaces of crystalline materials in UHV undergo relaxation, that is they change locally the lattice constant and unit cell, and under certain circumstances form a surface superstructure called a surface reconstruction [4]. The latter phenomenon is presented graphically in figure 2.4. A given surface may form many reconstructions with different periodicity and stoichiometry. For example in case of the (100)-oriented GaAs surface one can typically observe $c(4\times 4)$, (2×4) or (4×6) reconstructions (many more are possible), the former two being As-rich, and the last one being Ga-rich. It has to be noted that reconstructions with the same periodicity may exist in different phases, that is with different atom arrangement in their unit cells. What surface reconstruction is observed in a given situation depends on many parameters, such as substrate temperature, flux of the constituent species, as well as the exact history of the substrate. As an example of the last statement one can use the GaAs surface with initial $c(4\times 4)$ reconstruction that has been heated up under no group V flux to a temperature high enough to form the (2×4) reconstruction and finally cooled down to the initial temperature. After such cycle the surface will not recover to the starting state unless group V flux is supplied. This is sometimes called surface reconstruction freeze-in. It will be shown later that the surface reconstruction can have profound influence on the formation and morphology of the metal NCs. Moreover, one can use the transitions between different reconstructions to calibrate temperature or III/V flux ratio in a growth system independent way. Finally, it has to be mentioned that one can directly deduce the surface reconstruction using RHEED or reflectance anisotropy spectroscopy.

2.3 RHEED

RHEED is an in-situ characterization technique used in almost every MBE system. It uses a parallel, high energy (typically 10-20 keV) electron beam incident at very high angle to the substrate surface in order to gain some insight into the state of this surface by means of diffraction. Once scattered, the electron beam hits a fluorescent screen, what allows to observe visually the obtained diffraction pattern. In principle, this can be, and sometimes is, done by eye, however in modern systems one uses a digital camera to capture and record or inspect in real-time the appearing RHEED patterns. The principle of RHEED is visualized in figure 2.5. This in-situ characterization technique is almost indispensable. As already mentioned, it allows to infer the surface reconstruction. What is more, it allows to assess qualitatively the cleanliness and roughness of the substrate, as well as to determine if the growth is 2D or 3D. It can be also used to estimate the density of the grown 3D islands. Faint 3D diffraction spots on top of the regular 2D pattern correspond to low density islands. In the extremely low density limit actually no spots

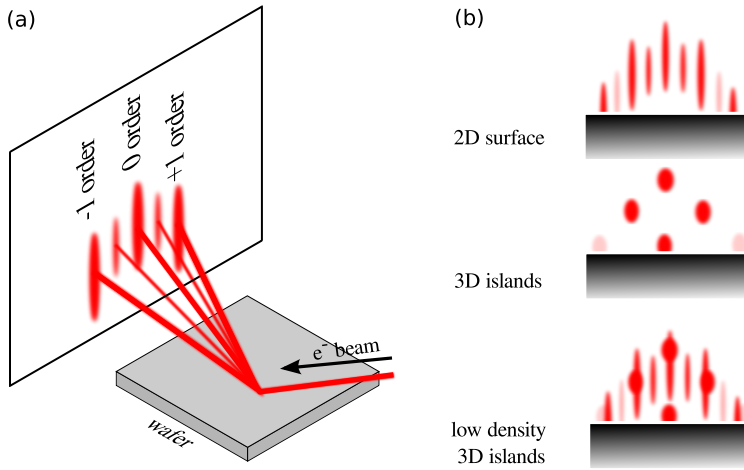


Figure 2.5: Illustration of the principle of the RHEED measurements. Using this technique it is very easy to qualitatively determine if 2D or 3D growth occurs

can be observed, as all the signal is buried in the diffuse scattering background that is always present. On the other hand, for high densities the diffraction spots dominate completely. Additionally, one can deduce some information about the shape of the islands from the shape of the diffraction spots observed in different azimuths. RHEED enables also the grower to measure the growth rate using so called RHEED oscillations. The period of such oscillations corresponds to the deposition of a single ML, so extreme degree of thickness control can be obtained. It has been even demonstrated that the RHEED signal can be used in real-time to control the deposition times, this technique is known as phase-locked epitaxy [3]. Obviously, this is only possible if the oscillations can be observed, what is not always the case. Sometimes one wants to measure extremely low growth rates, like in the case of the growth of low density InAs QDs or metal NCs. This can be done by means of the 2D-3D transition time if the critical thickness is known beforehand. On the other hand, the same principle can be applied to determine the critical thickness if the growth rate is known. Finally, RHEED allows to calibrate the substrate temperature using reference points such as the native oxide desorption temperature, melting point of In NCs, or using transition temperatures of different surface reconstructions under static conditions, that is no flux.

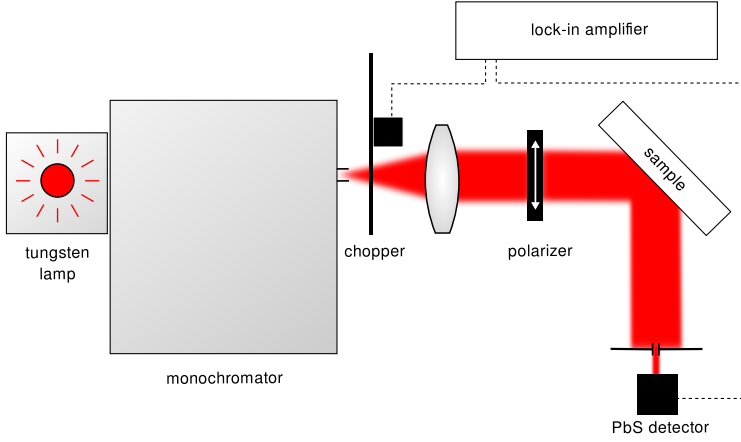


Figure 2.6: Schematic of the experimental setup used to measure DR.

2.4 Optical characterization

2.4.1 Differential reflectivity

In order to determine the LSPR wavelength of the deposited metal NCs the author used a technique called DR. The setup assembled to perform such measurements is presented in figure 2.6. It consisted of an incandescent white light source that was coupled into a monochromator in order to select the desired wavelength. After the light exited the monochromator it was collimated by a single lens, it passed through a polarizer, reflected from the sample surface placed under an angle of 45° , and finally was measured by a thermoelectrically cooled photoconductive PbS detector. A lock-in detection scheme was used in the setup, so the light beam was modulated mechanically by a chopper, and the PbS detector was connected to a lock-in amplifier. The whole setup was controlled by a self-developed labview software via a GPIB interface. In order to obtain the result, first a reference scan was performed on a sample without any metal NCs giving $\tilde{R}_0(\lambda) = R_0(\lambda)s(\lambda)$, where R is the real reflectivity and s is the instrumental characteristic of the setup. Only after that a measurement of the actual sample of interest with metal NCs on top was done yielding $\tilde{R}(\lambda) = R(\lambda)s(\lambda)$. The final result was calculated from the relation

$$\frac{\Delta R}{R_0} = \frac{\tilde{R}}{\tilde{R}_0} - 1.$$

Since the measurement was double pass, it was necessary to check the stability of the used light source in order to exclude the possibility of experimental errors due to long term drift of its spectral characteristic. Measurements performed consecutively on the same sample gave repeat-

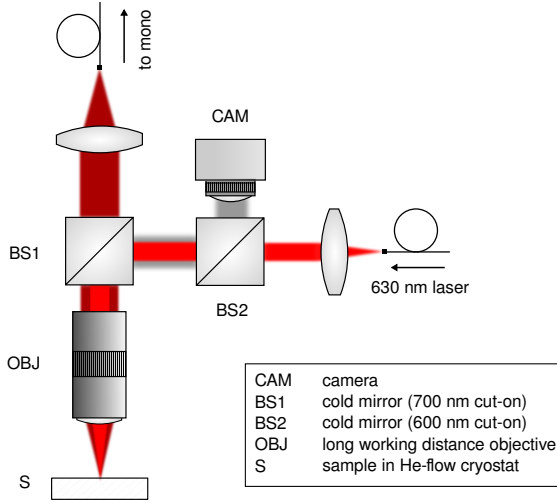


Figure 2.7: Schematic of the experimental setup used to perform PL measurements.

edly results equal to unity within 0.2% relative error in the whole spectral range. This is much less than the observed changes of the reflectivity in all cases greater than 5%, so the light source instability did not introduce a significant error. Additionally, potential small differences in angular alignment between the reference and main sample could result in severe errors due to the ratiometric nature of the measurement. This, however, was not the case. Repeated measurements on the same sample pair gave consistent results. What is more, introduction of intentional misalignment did not result in a qualitative change of the resultant DR spectrum. Such misalignment resulted only in the appearance of a slowly varying background with the SPR peak on top.

The theory behind DR can be found for example in [5]. In the context of the thesis it is sufficient to mention that the measured quantity $\frac{\Delta R}{R_0}$ scales like

$$\frac{\Delta R}{R_0} \propto N \text{Im}[\alpha],$$

where N is the density of the metal NCs, and α is their polarizability. $\frac{\Delta R}{R_0}$ depends intrinsically on the polarization and incidence angle of the incoming light. Moreover, in the case of anisotropic structures it is influenced by the orientation of the sample and obviously once again by the polarization of the incident beam. For this reason all measurements were performed with consistent sample orientation, that is with the [011] direction perpendicular to the plane of incidence.

2.4.2 Photoluminescence

In order to further investigate the optical properties of the grown samples the author performed room and low temperature measurements with the setup that is presented in figure 2.7. A semiconductor laser diode emitting at 630 nm was used as an excitation source. It was coupled by means of a single-mode fiber to one of the arms of the setup. The sample was placed in a He-flow cryostat mounted on a computer controlled xyz stage used for alignment and focusing. The laser light was focused and the PL emission was collected by a long working distance objective. The emitted light was separated from the exciting light beam by means of a cold mirror. The light was coupled into an optical fiber that could be connected to different monochromators. For most of the work a single quarter meter monochromator equipped with a liquid nitrogen cooled InGaAs photodiode array detector was used. For some of the work the author used a double, one meter monochromator with a liquid nitrogen cooled Si CCD detector. Depending on the magnification of the mounted objective, core size of the out-coupling fiber, as well as defocusing of the laser spot the setup could be used for both macro and micro-PL measurements. The sample surface could be illuminated off-axis in order to observe a dark-field image of the surface. This was especially helpful for the investigations of the patterned samples discussed in chapter 6.

2.5 AFM

The morphology of all grown samples was investigated by means of AFM. This characterization technique relies on a cantilever with an extremely sharp pyramidal tip (<10 nm radius) that is scanned in xy direction across the sample surface by means of piezoelectric actuators. While scanning, the deflection (so called contact mode), or oscillation amplitude (so called tapping-mode) is kept constant by a feedback loop controlling the z piezoelectric actuator. Both the deflection and oscillation amplitudes are measured using a laser beam reflected from the cantilever and shining on a four quadrant photodiode. If the piezos are calibrated beforehand, one obtains a 3D map of the sample surface. All data presented in the thesis were analyzed by the open source software called Gwyddion [6] that, among many other things, allows to analyze the different characteristics of the sample. They include density or size distribution of the 3D islands present on the surface. This was especially useful for the author to investigate all the grown QD and NC samples.

It has to be mentioned that although AFM is a widespread and standard characterization technique, it is somewhat of an art to obtain really good images. In order to become a proficient AFM operator, one has to accustom with the effects of tip wear and contamination, loose debris on the surface, wrong feedback loop settings and finally external disturbances of all kinds. There is no possibility to know apriori if a given result is

real or not. In the end it is mostly a matter of experience that is gained only after many hours of AFM measurements.

2.6 Processing

In chapter 6 the author investigates the growth on patterned substrates. In order to obtain such substrates, it was necessary to use few processing steps like photolithography and wet chemical etching. Semiconductor processing and device fabrication is a huge topic on its own rights, so only brief descriptions of the used techniques are given. A general review of semiconductor processing with good in-depth coverage of many additional topics can be found in [7].

2.6.1 Photolithography

In order to obtain the desired pattern on the substrates, contact photolithography was used. It utilizes a glass mask with such pattern defined in a thin film of Cr. It is brought in contact with the sample surface covered beforehand with a thin photoresist layer. UV light is used to transfer the pattern. The exposed areas become more, or less soluble in a suitable developer in the case of, respectively, positive and negative photoresists. After development the layer can act as a mask for etching or metallization and, when not needed anymore, can be stripped chemically or by means of O_2 plasma.

In this work the author used a Karl-Suss MA-6 mask aligner in hard-contact mode, and a HPR-504 photoresist. Before spinning on the resist the wafers were baked for 5 minutes at $250\text{ }^\circ\text{C}$ in order to improve the adhesion. No additional adhesion promoters were used. After spinning the wafers were put on a hotplate for 2 minutes at $95\text{ }^\circ\text{C}$ and for additional 2 minutes at $105\text{ }^\circ\text{C}$ after the exposure. The patterns were developed in a NaOH-based developer and finally descummed for 2 minutes in an O_2 plasma asher.

2.6.2 Wet etching

There are numerous known effective wet etchants for III-V semiconductors [8]. Many of them follow a similar scheme. It employs a base or an acid and an oxidizing agent. The latter oxidizes the semiconductor, and the former two dissolve the products of such a reaction. The author chose the citric acid/hydrogen peroxide etching mixture because it is relatively safe and allows to use photoresist as a masking layer. The exact composition used was 50 % aqueous solution of citric acid monohydrate and 30 % hydrogen peroxide mixed together in 40:1 proportion by volume. The etching rate of this mixture was 70 nm per minute at room temperature as measured with a surface profilometer. This allowed to easily obtain

2 Sample growth, processing and characterization

holes with sub 100 nm depth which were used for the positioning of Ag NCs.

2.6.3 Cleaning procedure for epitaxial regrowth

All GaAs wafers used to grow the investigated samples were supplied by Wafertech in "epi-ready" quality, that is factory cleaned with a propriety process. Although no exact details of the wafer preparation process are known by the author, it worked quite well. No additional cleaning steps were necessary if the samples were used as delivered. However, after processing and thus inevitable contact with different organic and inorganic chemicals this was not true anymore. In order to clean the GaAs surface and prepare it for epitaxial growth, the following procedure was used. First the photoresist used as etching mask was removed by rinsing in acetone followed by rinsing in deionized water. Any remaining organic residues were removed with a O₂ plasma asher. Afterwards, the substrate was immersed for ten minutes in 98 % H₂SO₄, once again rinsed in deionized water, blown dry with N₂, and finally put on a hotplate at 250 °C for 5 minutes in order to regrow a native oxide layer. No real optimization of this preparation recipe was necessary as it performed very well from the beginning. The RHEED patterns observed just after thermal oxide removal indicated an almost flat surface and were much better than those observed for "epi-ready" wafers used as-is. It is obviously possible that there is some additional contamination introduced by the described process. It did not, however, influence the grown samples in any visible way.

2.7 Summary

To conclude, in this chapter the author introduced the growth, processing and characterization methods used in the course of his research to prepare and investigate the samples. The presented information is by no means complete, however, it should be helpful to fully understand all reported results, and should help to recreate or further develop them.

References

- [1] J. Ayers, *Heteroepitaxy of semiconductors: theory, growth, and characterization*. CRC Press, 2007.
- [2] G. Stringfellow, *Organometallic Vapor-Phase Epitaxy: Theory and Practice*. Elsevier Science, 1998.
- [3] M. A. Herman and H. Sitter, *Molecular beam epitaxy: fundamentals and current status*. Springer, 1996.
- [4] Lüth, H., *Solid Surfaces, Interfaces and Thin Films*. Springer, 2010.

- [5] R. Lazzari, S. Roux, I. Simonsen, J. Jupille, D. Bedeaux, and J. Vlioger, “Multipolar plasmon resonances in supported silver particles: The case of Ag/ α -Al₂O₃(0001),” *Physical Review B*, vol. 65, p. 235 424, 2002.
- [6] <http://gwyddion.net>.
- [7] A. Baca, C. Ashby, and I. of Electrical Engineers, *Fabrication of GaAs devices*. Institution of Electrical Engineers, 2005.
- [8] A. Clawson, “Guide to references on III–V semiconductor chemical etching,” *Materials Science and Engineering: R: Reports*, vol. 31, p. 1, 2001.

3 In nanocrystals

In the current chapter the author demonstrates the growth of epitaxial In NCs by MBE on GaAs. It is shown that such NCs support a LSPR in the NIR wavelength range, coinciding with the typical emission wavelength of InAs QDs. What is more, the author shows that it is possible to position such In NCs on both near-surface, as well as uncapped InAs QDs with very high yield. PL measurements of such hybrid structures show an additional spectral feature corresponding to coupled LSPR-QD emission. This additional feature resolves into individual QD lines in micro-PL measurements, proving that plasmonic enhancement is observed at single QD level.

3.1 Epitaxial metal nanocrystals

MBE growth of different metals on semiconductors has been already investigated in many contexts. The specific examples include Au, Ag, Al, In, CoAl, NiAl, as well as rare-earth arsenides [1]. It can yield both planar layers, as well as 3D NCs with excellent quality due to the high cleanliness of the process and high purity of the sources. Surprisingly, the usage of MBE growth of metals for applications in plasmonics has so far not been considered. This is especially puzzling if one takes into account that it enables the growth of single-crystalline structures that exhibit the lowest resistive losses, as well as it enables the monolithic integration of metallic nanostructures with active media based on semiconductor QDs or QWs. Epitaxial growth might seem uncontrollable and unable to provide positioned structures. This is, however, not true, as guided self-assembly on artificially and naturally patterned substrates has proven to allow the precise positioning of semiconductor QDs [2, 3]. It is not obvious whether such mechanism applies to metal NC positioning as well. This question shall be answered in the current chapter and throughout the rest of the thesis and it is the main focus of the authors work. In order to do so, In was chosen as the model material because of its availability in the used MBE system, as well as because of previous reports on In forming epitaxial NCs on GaAs surfaces [4–7].

3.2 Experimental details

All samples investigated in this chapter were grown by a Varian Gen II solid-source MBE system on singular, (100) oriented, undoped GaAs

substrates. After oxide removal under As_4 flux at 580°C , a 200 nm thick GaAs buffer layer was deposited. In case of the samples for structural and optical characterization of the In NCs, the substrate was cooled down to temperatures between 50 and 120°C (thermocouple reading) and the As valve was closed around 300°C . This resulted in an As-rich $c(4\times 4)$ surface reconstruction, as determined by RHEED. After considerable time necessary for temperature stabilization, In was deposited with a coverage equivalent to 2 and 12 ML of InAs. The deposition process was monitored in all cases by RHEED. During this step the As background pressure was below 2×10^{-9} Torr to prevent any unwanted reactions. After the growth all samples were removed immediately from the MBE system and characterized by tapping-mode AFM, as well as DR spectroscopy.

In order to study the self-assembly of In NCs, they were grown on top of 1D QD arrays formed by strain-correlated stacking. The growth of such ordered structures is considerably complicated, and thus a schematic of the whole process is presented in figure 3.3a. After the buffer layer deposition, a 15-period InGaAs/GaAs superlattice (SL) template was grown for 1D QD ordering on top. Each SL period consisted of a 2.3 nm $\text{In}_{0.4}\text{Ga}_{0.6}\text{As}$ QD layer grown at 540°C immediately capped with 0.7 nm GaAs, annealed for 2 minutes at 580°C , and a 12 nm GaAs layer grown at this temperature. On the SL template a single layer of 2.3 nm $\text{In}_{0.4}\text{Ga}_{0.6}\text{As}$ QDs was deposited, either left uncapped or capped with a 3 nm thick GaAs layer. After this the samples were cooled down to 100 or 120°C and In NCs were grown following the already described procedure. The growth rates for GaAs and InAs used throughout the process were 0.054 and 0.0375 nm/s, respectively. In addition to AFM and DR characterization, temperature dependent PL measurements were performed.

Additional samples with In NCs deposited on top of isolated surface InAs QDs were investigated in order to demonstrate the feasibility of self-assembly based synthesis of low density hybrid metal-semiconductor nanostructures. In this case the low density InAs QDs were obtained by conversion of In NCs. Details of that process can be found in chapter 4.

3.3 Structural properties

The results of the RHEED and AFM measurements of the samples with In grown directly on GaAs are shown in figure 3.1. The In islands deposited below nominally 120°C exhibit a pyramid-like shape with square base oriented along [011] and distinct side facets, most likely of the $\{110\}$ kind. Some islands adopt more complicated shapes, which probably originate from the formation of defects, especially twin planes. A clear 2D to 3D RHEED transition is observed, as visible in figure 3.1 c and d. This is strong evidence that the islands obtained below 120°C are epitaxial metal NCs. In the case of deposition at nominally 120°C and

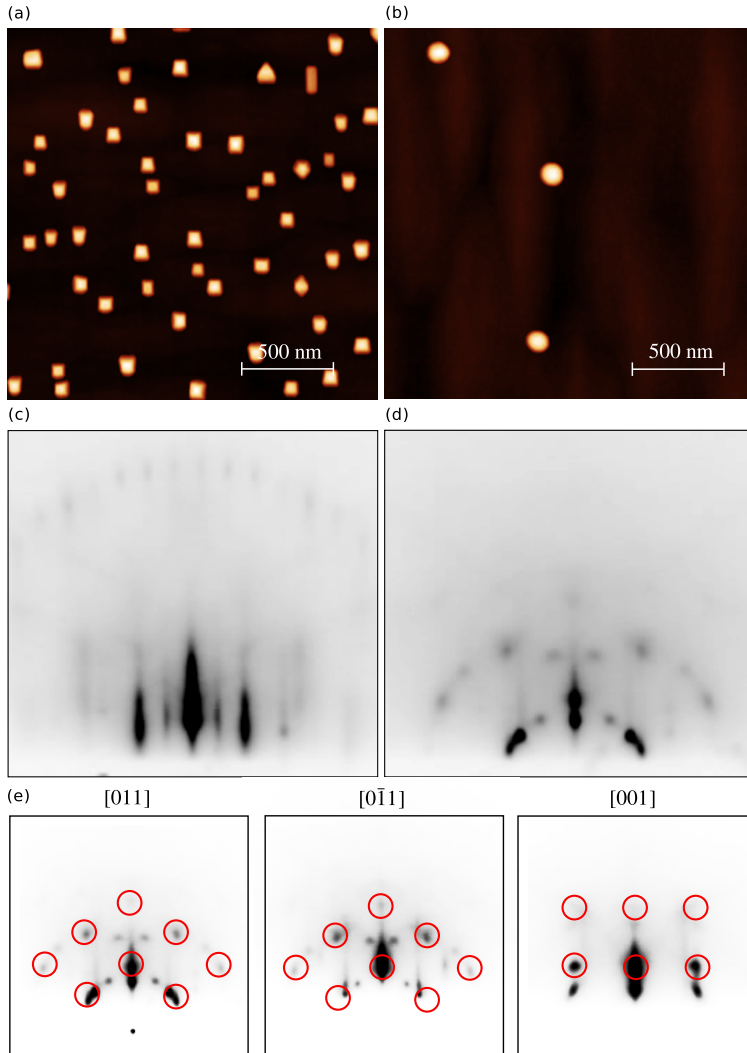


Figure 3.1: AFM measurement of In NCs obtained with 3 nm coverage and nominal substrate temperature of 80°C (a). Similar data for a sample with nominal deposition temperature of 120°C (b). Typical 2D to 3D RHEED transition observed during the deposition of In (c,d). Additional RHEED patterns in different azimuths used to deduce the epitaxial relation of the In NCs (e).

above, only spherical islands are formed with no visible crystallographic features. What is more, there is no RHEED transition. The initial $c(4 \times 4)$ pattern merges into an increasing diffuse scattering background. This behavior is explained by the fact that the islands grown nominally at 120 °C are liquid. The melting temperature of bulk In is 156 °C. In

an additional experiment to melt the In NCs in the MBE chamber by increasing the substrate temperature from 80 °C, a melting temperature between 170–180 °C was deduced from the disappearance of the spotty RHEED pattern. This discrepancy can be explained by heating of the GaAs surface by the open In effusion cell during In deposition and a slight offset of 10–20 °C between the thermocouple reading and the actual GaAs surface temperature for the closed In effusion cell during melting. Then, during In island growth, the thermocouple temperature reading of 80 °C is still below the bulk In melting temperature and the temperature reading of 120 °C is above. It is interesting to note that the In islands observed after melting of the NCs have the size, shape, and density very similar to the In islands grown at 120 °C. Hence, during the melting there is no memory of the size, shape, and density of the crystalline islands and an equilibrium state according to the higher temperature is reached.

Careful analysis of the RHEED patterns observed for different azimuths allows to deduce the in-plane epitaxial relation of the In NCs with the GaAs substrate to be $[001]_{\text{In}} \parallel [011]_{\text{GaAs}}$, where $[100]_{\text{In}} \parallel [100]_{\text{GaAs}}$ is the high symmetry direction of the body-centered tetragonal In lattice. The out of plane epitaxial relation is $(100)_{\text{In}} \parallel (100)_{\text{GaAs}}$, what can be inferred from the RHEED and AFM data. The additional diffraction features might be attributed to twin planes in the islands [8], surface scattering [9], finite size effects [10] or electron refraction [11].

3.4 Optical properties of In nanocrystals

In order to measure the spectral position of the NC LSPR, DR measurements were performed on samples with different metal coverage. The results are presented in figure 3.2. With the coverage increasing from 3 nm to 7 nm, the average In NC base size and height increased from 80 and 40 nm to 100 and 47 nm, respectively. This was accompanied by a clearly observable red shift of the LSPR peak from 940 to 1000 nm, as presented in figure 3.2d. This wavelength range matches well the typical emission wavelength of InGaAs QDs, what is very important in the studies of coupled structures. Additionally, the magnitude and the width of the LSPR peak increased significantly, what is, respectively, due to higher density and larger size non-uniformity of the In NCs.

3.5 Positioning of the In nanocrystals on InGaAs quantum dot arrays

In order to prove the feasibility of the epitaxy based approach for the synthesis of ordered active plasmonic nanostructures, the author investigated the growth of In NCs on naturally templated substrates with 1D

3.5 Positioning of the In nanocrystals on InGaAs quantum dot arrays

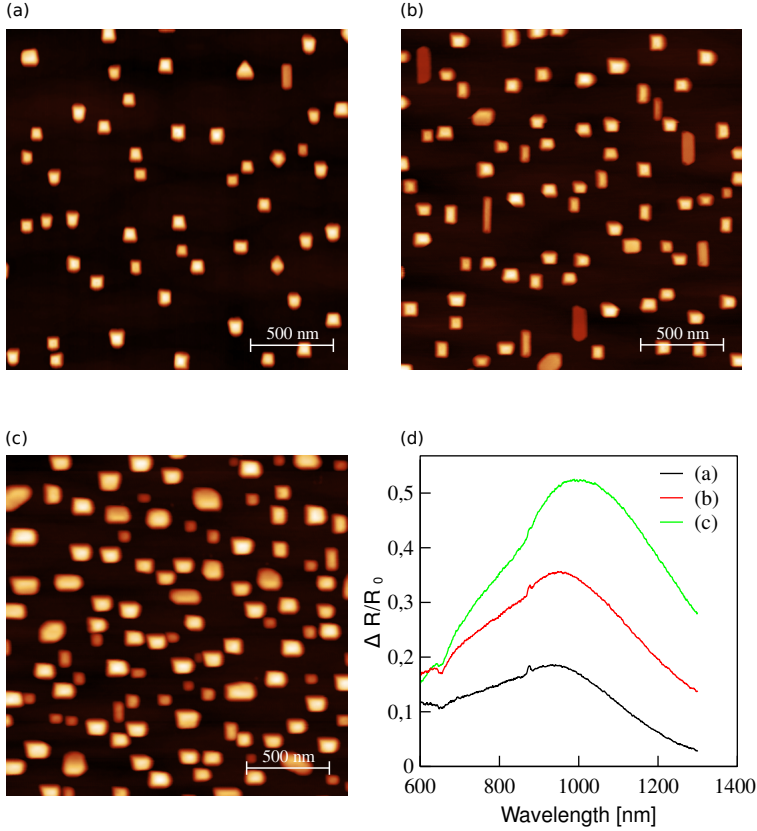


Figure 3.2: AFM images of In NCs obtained with coverages of 3 nm (a), 5 nm (b) and 7 nm (c), as well as corresponding DR data (d).

QD arrays. This was done with the hope of observing ordering analogous to strain-driven QD assembly. Figure 3.3 presents the results of such investigations. Two samples are shown, 1D QD arrays without capping and with 4 ML In coverage deposited at 100 °C, as well as QD arrays with 3 nm GaAs capping layer, 4 ML In coverage and the substrate temperature during the metal deposition equal to 120 °C. The density, average base size and height of the In NCs were strongly influenced by the presence of the thin GaAs capping layer and deposition temperature. They changed from $25 \mu\text{m}^{-2}$, 30 nm and 22 nm to $5 \mu\text{m}^{-2}$, 70 nm and 40 nm, respectively. This is most likely due to higher roughness of the uncapped sample, however, other factors, like different In ad-atom mobilities on GaAs and InGaAs surfaces and at different temperatures, might be also relevant. What is most important, in both cases the In NCs aligned on top of the InGaAs QDs. This resulted in correlated dilute NC arrangements for a relatively small In amount (figure 3.3b) and high growth temperature and to ordered 1D arrays of closely spaced In NCs

3 In nanocrystals

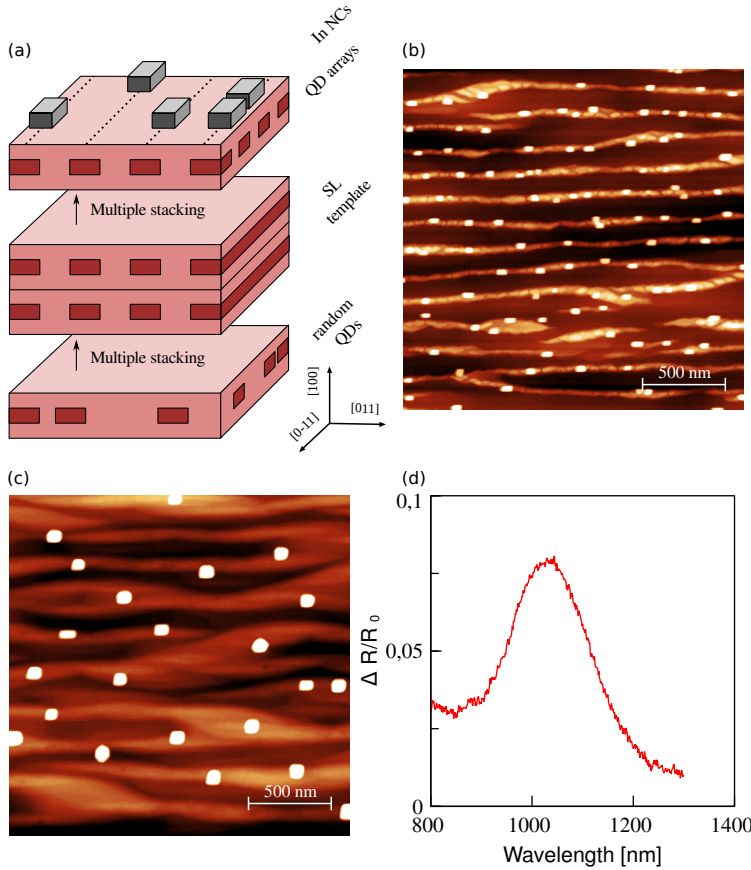


Figure 3.3: Schematic of the ordered sample structure (a). AFM image of such sample without (b) and with (c) 3 nm GaAs capping layer. DR spectrum of the capped sample.

for larger In amount and lower growth temperature (data not shown) [12]. The correlated In NC growth was preserved in the presence of the GaAs cap layer on the InGaAs QDs even though the surface smoothed with increasing cap layer thickness (height modulation of 7 nm without GaAs cap, and of 5 nm with 3 nm GaAs cap). This indicates that the alignment is not due to morphological features but due to strain mediated nucleation similar to the case of correlated stacking of InGaAs QDs. The fact that such alignment takes place is attributed to the crystalline nature of the In NCs with the shape of a truncated pyramid and a clear epitaxial relationship with the GaAs (100) surface.

The investigated ordered structures support a distinct LSPR centered at 1030 nm in the case of the In NCs on the capped QD arrays, as shown in figure 3.3d. The width of the peak is significantly smaller than that in the case of unordered NCs directly grown on GaAs. This is most likely

3.6 Photoluminescence of In nanocrystal/quantum dot arrays

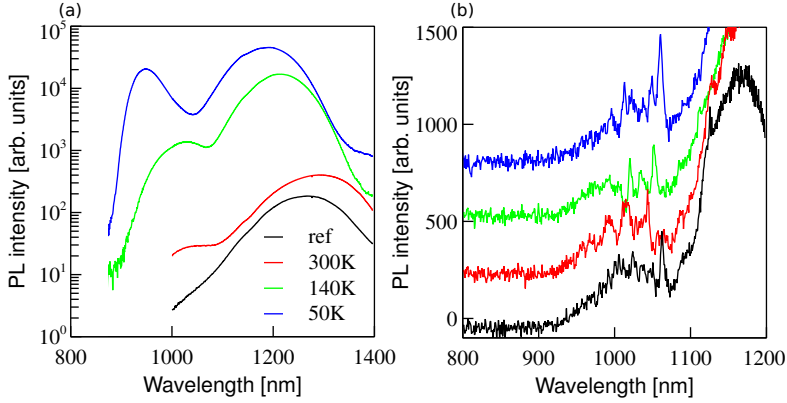


Figure 3.4: Results of macro- (a) and micro-PL (b) measurements on capped InGaAs QD arrays with In NCs on top.

due to higher uniformity of the metal NCs grown on QD templates.

3.6 Photoluminescence of In nanocrystal/quantum dot arrays

Figure 3.4 shows the temperature dependent PL spectra of the InGaAs QD arrays capped with 3 nm GaAs and with 3 nm In NCs deposited on top at 120 °C. The peak centered at low temperature at 1200 nm is from the QDs and that centered at 940 nm is from the SL template. As always observed, the PL from the SL template vanishes with increasing temperature due to thermally activated carrier transfer from the SL template to the QDs. At elevated temperature an additional peak centered at 1020 nm becomes visible, most clearly at 140 K, which is detected up to room temperature (RT). Such emission is not observed for the InGaAs QD arrays without In NCs on top, as seen in the PL spectrum denoted as ref in figure 3.4a, taken at RT. The PL peak coincides in energy with the plasmon resonance of the In NCs determined from the DR measurements performed at RT, shown in the figure 3.3d. The author assigns the PL peak of the InGaAs QD arrays centered at 1020 nm to coupled LSPR-QD emission which manifests itself in the resonant enhancement of the PL efficiency, although the overall PL intensity of the QDs is reduced in the presence of the In NCs. Coupled LSPR-QD emission is supported by the small low-energy shift with increasing temperature (due to the small change of the refractive index of GaAs, slightly redshifting the LSPR with temperature) compared to the much larger low-energy shift of the QD PL (due to the temperature dependent shrinkage of the GaAs band gap energy and carrier delocalization). At the lowest temperatures the LSPR enhanced emission overlaps with the SL template PL and can therefore

not be identified, although it increases in intensity due to lower resistive losses in the In NCs. LSPR enhanced emission of the SL template is not expected due to its larger separation from the In NCs together with the large refractive index of GaAs.

For micro-PL investigations the measurement temperature of 150 K was chosen as it is the temperature where the most distinct PL enhancement can be observed. At lower temperature the PL of the SL template dominates while at higher temperature the enhancement becomes less pronounced though it stays visible up to RT. No enhanced PL emission is observed for the reference sample without In NCs. Moreover, enhanced PL emission is not observed for similar structures with increased GaAs cap layer thickness and when the LSPR of the In NCs is detuned with respect to the QD PL by changing the size of the In NCs (depending on In amount and growth temperature). The enhanced PL emission splits up into distinct lines from single QDs. The linewidth of the emission from the single QDs is 3 to 5 nm. This relatively broad linewidth is typical for single surface QDs or QDs close to processed interfaces due to surface states or defects creating a fluctuating charge environment affecting the QD energy levels [13]. Most remarkably, the splitting up of the micro-PL can be only observed in the spectral region of the LSPR. This additionally confirms that it is due to enhanced emission only from those single QDs that are coupled to the LSPR of the In NCs which intentionally have a low density. Otherwise the QD density would be too high for the emission from individual QDs to be resolved with the achievable spatial resolution of about 1 μm . The one-dimensional QD ordering is beneficial for the observation of LSPR-QD coupling because it provides a continuous variation of the QD-metal separation. Nevertheless, the number of lines observed in micro-PL is much smaller than the number of metal NCs in the laser spot, because only very few QDs are both spatially and spectrally matched for optimum enhancement.

3.7 Formation of isolated metal-semiconductor hybrid structures

In the previous sections it was demonstrated that In NCs can be positioned on QD arrays based on the principle of strain-driven migration. Certainly it would be interesting to be able to fabricate also single, isolated hybrid QD-metal nanostructures based on low-density QDs. Investigations of samples with In deposited on top of low density QDs proved that it is possible. Figure 3.5a shows the AFM images of such samples, in this case with uncapped QDs. AFM investigations before and after In NC deposition unambiguously identify the smaller more round structures as the InAs QDs and the larger square/rectangular shaped structures as the In NCs. The density of the InAs QDs and In NCs is matched to within 20% and indeed every In NC is aligned to an InAs

3.7 Formation of isolated metal-semiconductor hybrid structures

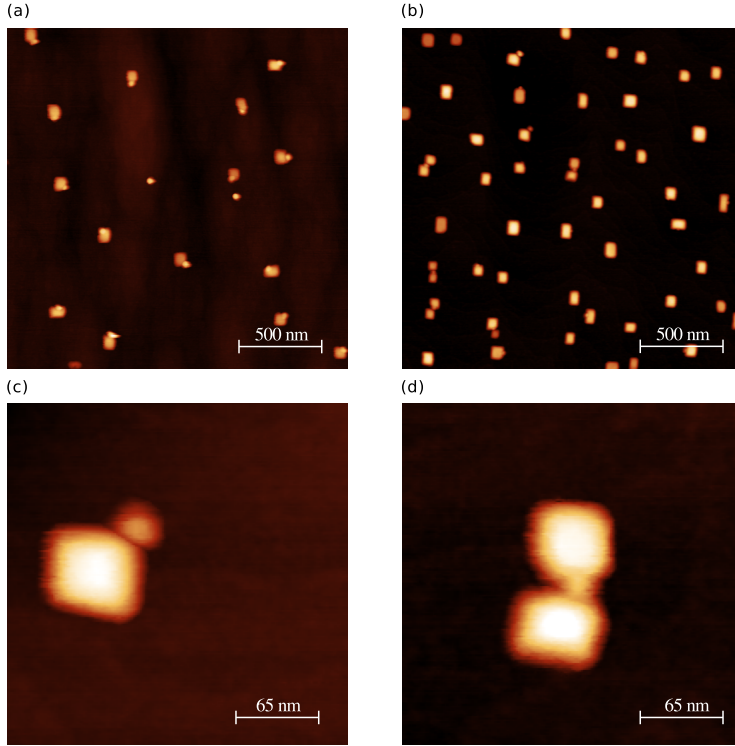


Figure 3.5: AFM images of hybrid InAs QD-In NC structures obtained with coverage of 1 (a) and 2 nm In (b). (c) and (d) show enlarged images of an individual QD-NC pair and a complex arrangement of a NC dimer with a single QD in the middle, respectively.

QD, demonstrating that the alignment mechanism is very robust. The In NCs and surface InAs QDs are in contact, as visible in figure 3.5c. Hence, as already demonstrated in this chapter, a precise separation control at the nanometer scale is guaranteed by the natural alignment and additionally a thin GaAs cap layer on the QDs. For the 2 nm In NCs their density is significantly larger than the density of the InAs QDs, namely 14 versus $5 \mu\text{m}^{-2}$. As a consequence, all QDs have an In NC attached to them with excess In NCs in between, presented in figure 3.5b. What is most interesting, a large amount of In NC dimers with an InAs QD in the gap appears. An example of such a complex structure is shown with enlarged scale in the figure 3.5d. The density of these dimer structures is about 25% of the density of all QD-metal pairs. Such dimer structures are extremely interesting, because they facilitate local plasmon field enhancements orders of magnitude larger than those of single metal nanoparticles [14] and thus are the prime candidates for achieving single QD lasing and entering the QD-SPR strong coupling

regime [15]. Additionally they are suitable for active plasmonic structures facilitating all-optical switching of the LSPR position [16].

3.8 Summary

In conclusion, the author demonstrated the growth of epitaxial In NCs on GaAs, that support a LSPR in the NIR wavelength range. When grown on top of uncapped or near-surface QDs, the NCs align themselves on the QDs due to strain-drive ad-atom migration. This allows for bottom-up fabrication of active plasmonic nanostructures with different arrangements including sparse and dense arrays, as well as isolated QDs paired with single metal NCs or NC dimers. Additionally, the author showed coupled LSPR-QD emission in the ordered structures, which could be resolved down to the single QD level. This proves that bottom-up epitaxial synthesis of active plasmonic nanostructures is indeed a feasible and effective fabrication approach.

References

- [1] T. Sands, C. Palmstrøm, J. Harbison, V. Keramidis, N. Tabatabaie, T. Cheeks, R. Ramesh, and Y. Silberberg, “Stable and epitaxial metal/III-V semiconductor heterostructures,” *Materials Science Reports*, vol. 5, p. 99, 1990.
- [2] C. Schneider, A. Huggenberger, T. Sünner, T. Heindel, M. Strauß, S. Göpfert, P. Weinmann, S. Reitzenstein, L. Worschech, M. Kamp, S. Höfling, and A. Forchel, “Single site-controlled In(Ga)As/GaAs quantum dots: growth, properties and device integration,” *Nanotechnology*, vol. 20, p. 434 012, 2009.
- [3] T. Mano, R. Nötzel, G. J. Hamhuis, T. J. Eijkemans, and J. H. Wolter, “Direct imaging of self-organized anisotropic strain engineering for improved one-dimensional ordering of (In,Ga)As quantum dot arrays,” *Journal of Applied Physics*, vol. 95, p. 109, 2004.
- [4] D. E. Savage and M. G. Lagally, “Crystallography of In on GaAs (110): Possible Relationship of Laterally Inhomogeneous Structure to Fermi-Level Pinning,” *Physical Review Letters*, vol. 55, p. 959, 1985.
- [5] —, “Reflection high-energy electron diffraction study of the growth of In on GaAs (110) at different temperatures,” *Journal of Vacuum Science & Technology B: Microelectronics and Nanometer Structures*, vol. 4, p. 943, 1986.
- [6] J. Ding, J. Washburn, T. Sands, and V. G. Keramidis, “In/GaAs reaction: Effect of an intervening oxide layer,” *Applied Physics Letters*, vol. 49, p. 818, 1986.

- [7] J. S. Kim and N. Koguchi, "Near room temperature droplet epitaxy for fabrication of InAs quantum dots," *Applied Physics Letters*, vol. 85, p. 5893, 2004.
- [8] R. Tanner, I. Goldfarb, M. Castell, and G. Briggs, "The evolution of Ni nanoislands on the rutile TiO₂ (110) surface with coverage, heating and oxygen treatment," *Surface Science*, vol. 486, p. 167, 2001.
- [9] H. Lee, R. Lowe-Webb, W. Yang, and P. C. Sercel, "Determination of the shape of self-organized InAs/GaAs quantum dots by reflection high energy electron diffraction," *Applied Physics Letters*, vol. 72, p. 812, 1998.
- [10] B. Fultz and J. Howe, *Transmission electron microscopy and diffraction of materials*. Springer, 2002.
- [11] T. Hanada, B.-H. Koo, H. Totsuka, and T. Yao, "Anisotropic shape of self-assembled InAs quantum dots: Refraction effect on spot shape of reflection high-energy electron diffraction," *Physical Review B*, vol. 64, p. 165 307, 2001.
- [12] A. Urbani czyk, G. J. Hamhuis, and R. N tzel, "Strain-driven alignment of In nanocrystals on InGaAs quantum dot arrays and coupled plasmon-quantum dot emission," *Applied Physics Letters*, vol. 96, p. 113 101, 2010.
- [13] M. Pfeiffer, K. Lindfors, P. Atkinson, A. Rastelli, O. G. Schmidt, H. Giessen, and M. Lippitz, "Positioning plasmonic nanostructures on single quantum emitters," *Physica Status Solidi (b)*, vol. 249, p. 678, 2012.
- [14] E. Hao and G. C. Schatz, "Electromagnetic fields around silver nanoparticles and dimers," *The Journal of Chemical Physics*, vol. 120, p. 357, 2004.
- [15] S. Savasta, R. Saija, A. Ridolfo, O. Di Stefano, P. Denti, and F. Borghese, "Nanopolaritons: Vacuum Rabi Splitting with a Single Quantum Dot in the Center of a Dimer Nanoantenna," *ACS Nano*, vol. 4, p. 6369, 2010.
- [16] M. Abb, P. Albella, J. Aizpurua, and O. L. Muskens, "All-Optical Control of a Single Plasmonic Nanoantenna-ITO Hybrid," *Nano Letters*, vol. 11, p. 2457, 2011.

4 Conversion of In nanocrystals into quantum dots

In this chapter the author investigates the formation of InAs QDs by recrystallization of In NCs grown at low temperatures. Despite the low temperature nature of the process, single QDs exhibit excellent linewidths comparable to those of high quality SK QDs. By using this non-conventional growth method it is possible to obtain very easily low density QDs. It has also a large potential for the synthesis of QDs without a WL, as well as ones emitting at long wavelengths.

4.1 Droplet epitaxy

InAs/GaAs QDs are prime candidates for solid-state realization of functionalities such as qubits [1], quantum gates [2], single photon sources [3, 4], and cavity quantum electrodynamics systems [5, 6]. Such applications require reproducible and well controllable means of obtaining low-density QDs, as a single QD is the basic building block of above mentioned devices. Low-density InAs/GaAs QDs are usually obtained by MBE or MOVPE using the SK growth mode and small InAs coverage above the critical thickness [7] or extremely low growth rates [8]. The disadvantage of those well-established approaches is the fact that they are very sensitive to small variations of the growth conditions. This lowers significantly the reproducibility of such processes. An alternative, yet so far widely unexplored route to achieve this is to use DE [9], where one first deposits metallic liquid In droplets or, in the discussed case, epitaxial In NCs and afterward recrystallizes them under As flux. This offers a very robust and reproducible way to grow low-density QDs without relying on extremely low flux or precise coverage control. It has to be mentioned that DE allows as well to obtain QDs in strain free systems like GaAs/AlAs [10], what is the main motivation to investigate it. Additionally, with DE it is possible to obtain QDs on $\{111\}$ surfaces, for which the SK growth mode does not occur. This is especially important for obtaining highly symmetric QDs, which are good candidates for solid-state entangled photon sources [11, 12]. What is more, DE enables also to grow complex nanostructures such as single and multiple nanorings [13], QD-pairs [14] and many others [15]. All this is possible because of the multi-step nature of the DE process, what allows to control and rationally design the growth

4 Conversion of In nanocrystals into quantum dots

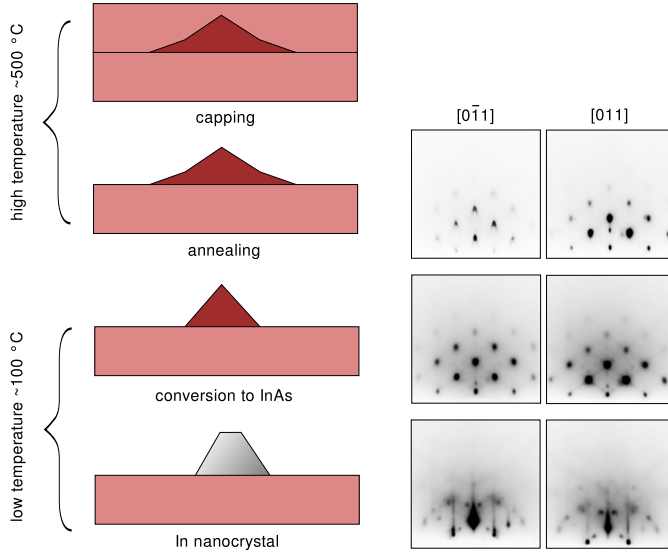


Figure 4.1: Scheme of the In NC to InAs QD conversion process. On the right side of each step typically observed RHEED patterns are shown. It is evident that after high temperature annealing the QDs become anisotropic, because different diffraction patterns are observed in the $[011]$ and $[0\bar{1}1]$ azimuths.

process with much greater precision and freedom than in the case of SK growth of QDs.

4.2 Experimental details

All investigated samples were grown by a solid-source MBE on singular, (100) oriented, undoped GaAs substrates. After oxide removal under As_4 flux at 580 °C, a 200 nm thick GaAs buffer layer was grown. The substrates were then cooled to 420 °C, 350 °C or 250 °C and the As flux was switched off. For the highest temperature a clear (2x4) surface reconstruction was observed by RHEED, while for the lower temperatures the surface reconstruction was c(4x4). The (2x4) reconstruction was most likely the gamma phase. The substrates were then cooled to 100 °C with the base pressure in the growth chamber below 2×10^{-8} mbar. The As_4 background pressure was low enough for the respective surface reconstructions to be stable for at least 30 minutes, also in the (2x4) case. In was deposited at a growth rate of 0.01 ML/s to form In NCs with well defined epitaxial relationship. This was evidenced by the observation of a spotty RHEED transmission diffraction pattern, which was described in detail in chapter 3. The NCs were transformed to InAs QDs by annealing under As_4 flux, initially at 100 °C, and then at 420 °C for 10 minutes. The samples for optical characterization were

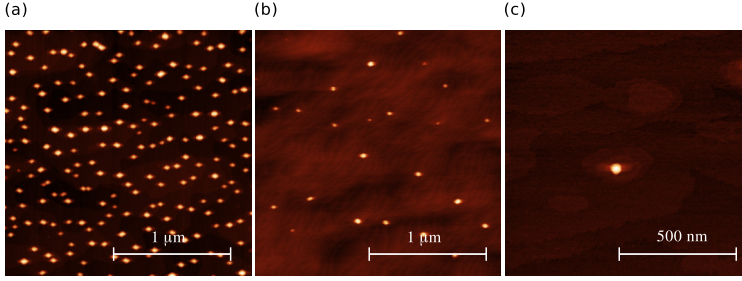


Figure 4.2: AFM images of different samples obtained with the proposed method. It is possible to obtain QD densities down to $1 \mu\text{m}^{-2}$.

additionally heated up to 480°C , annealed for one or ten minutes, capped with 20 nm GaAs, then heated to 580°C , and finally capped with 100 nm GaAs. Additionally, higher density samples for future structural characterization were grown by a similar procedure, albeit with higher In deposition rate and lower substrate temperature during NC deposition of about 80°C to facilitate a higher In NC nucleation density. In the case of such samples there was no intermediate annealing step at 420°C , and the initial 20 nm GaAs capping layer was grown at this temperature. The morphology of all the samples was characterized by tapping-mode AFM under ambient conditions. The density of the QDs was determined based on $8 \text{ by } 8 \mu\text{m}^2$ images to evaluate a statistically significant QD number. PL measurements were performed with the samples placed in a continuous-flow He cryostat at 10K and RT in the setup described in chapter 2. In order to accurately determine the PL linewidths of individual QDs, high resolution PL measurements were performed by fiber-coupling this setup to a double monochromator equipped with a liquid nitrogen cooled multichannel Si detector.

4.3 Structure and morphology

As already discussed in chapter 3, In can form both epitaxial NCs and liquid or amorphous droplets when the substrate temperature during the metal deposition is lower or higher than the melting point of In, respectively. Upon exposure to As flux, both can be converted to InAs. In the case of GaAs/AlAs DE one usually uses the droplets to obtain QDs, but in the case InAs this is not possible, because under typical growth conditions on (100)-oriented GaAs the obtained droplets are too big and too sparse. Their low temperature recrystallization results in very large InAs islands that are not suitable for further regrowth [16]. High temperature recrystallization of liquid In droplets results in very irregular and nonuniform structures [17], which are not desired as well. Therefore, in order to obtain InAs QDs one has to start with In NCs.

4 Conversion of In nanocrystals into quantum dots

The different steps of the In to InAs conversion process are depicted in figure 4.1. The As flux is turned on immediately after the NCs are deposited. Already at this point, despite the very low temperature, InAs forms. This is evidenced by a change in the RHEED pattern, revealing diffraction spots characteristic for InAs QDs. The recrystallization is however not complete, as additional features are still visible. Upon heating up and annealing of the samples only the InAs pattern remains visible. Additionally, due to anisotropic ad-atom migration on the GaAs surface, the RHEED pattern visible along $[0\bar{1}1]$ develops characteristic chevrons.

Examples of AFM images of different QD samples obtained with different In deposition conditions are shown in figure 4.2. By varying the growth rate from 0.5 ML/s to 0.01 ML/s it is easy to obtain QDs with densities ranging from 150 to 1 per μm^2 . The low density regime is thus accessible without resorting to extremely low growth rates, what makes the process much more controllable and easily repeatable. On the other hand, the maximum measured density is not very high compared to what has been reported for classical SK growth. High density QDs are desirable for fabrication of devices such as lasers and optical amplifiers. The present results indicate that DE of InAs is not suitable to be used for these applications. However, further investigations of the growth process may enable this. One possible strategy to achieve high QD density is to grow on substrates with intentional miscut or with high-index orientation like (311)B. Such approach was used successfully to obtain very high QD densities for the GaAs/AlAs material system [18].

It is well known that the stoichiometry of the GaAs surface varies significantly with changing surface reconstruction [19]. This is expected to have significant impact on the growth of In NCs, as In is very reactive with excess As bound to the surface. Indeed, careful studies confirm this proposition. The results of such investigation are presented in figure 4.3. For the most As-rich starting surface, with the As flux stopped at 250 °C, no In NCs form for an In coverage up to 2 ML and the resulting surface is very rough. All In reacts with excess As to form an irregular InAs layer. For the intermediate case when the As supply is switched off at 350 °C, In NCs form for 1.2 ML In deposition. Unexpectedly, they have a clearly bimodal size distribution. 80% of them have a square shape with average height of 15 nm and base size of 40 nm. The remaining 20% have an elongated shape with long-axis parallel to $[011]$, average height of 5 nm and average length and width of 90 nm and 35 nm, respectively. Careful analysis of figure 4.3b reveals that the elongated islands are connected to traces parallel to $[011]$. This observation is analogous to findings of Tersoff et. al. [20]. Most likely the driving force for elongation is reaction of excess As on the surface with metallic In leaving behind those traces. In case of the less As-rich (2x4) starting surface reconstruction studied here, prepared by switching off the As supply at 420°C, the RHEED transition indicating the In NC formation is observed for In coverages as

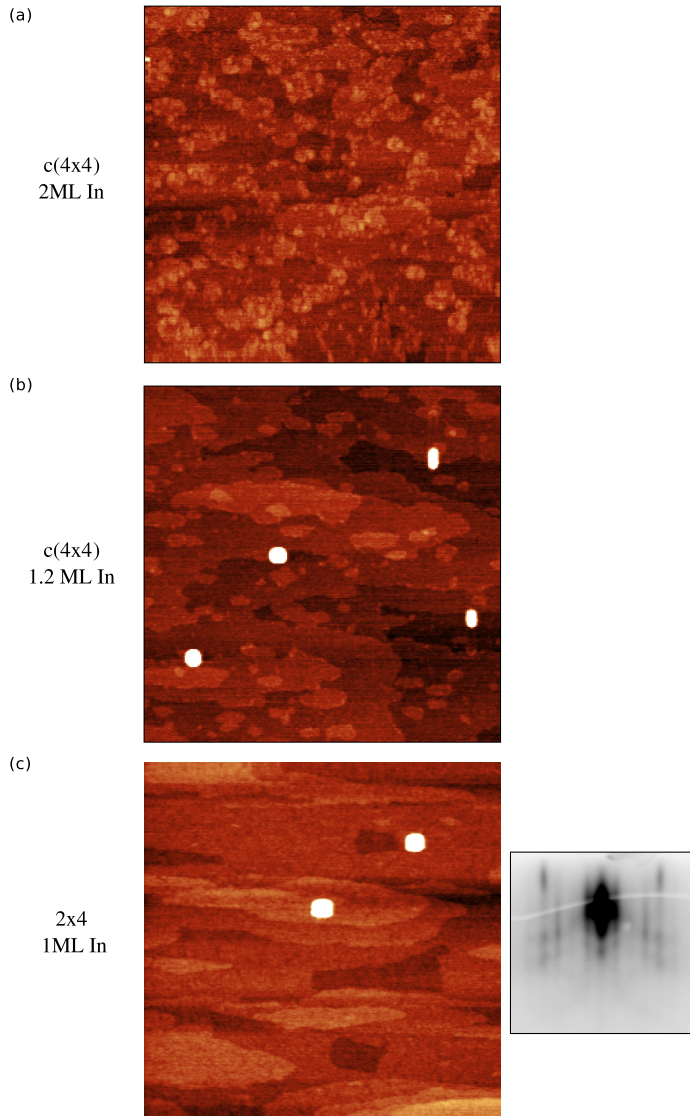


Figure 4.3: The influence of the initial substrate reconstruction on the morphology of the In NCs and the In amount necessary to obtain them. The height contrast is 3 nm and all scan fields are 1 μm x 1 μm . (a) As supply switched off at 250 $^{\circ}\text{C}$, starting surface reconstruction c(4x4), no RHEED transition observed for In coverage up to 2 ML. (b) As supply switched off at 350 $^{\circ}\text{C}$, starting surface reconstruction c(4x4), RHEED transition visible for In coverage of 1.2 ML. (c) As supply switched off at 420 $^{\circ}\text{C}$, starting surface reconstruction (2x4), RHEED transition visible for In coverage of 1 ML. Inset in (c) shows a RHEED pattern in the $[\bar{1}\bar{1}0]$ direction captured directly before the deposition of In.

4 Conversion of In nanocrystals into quantum dots

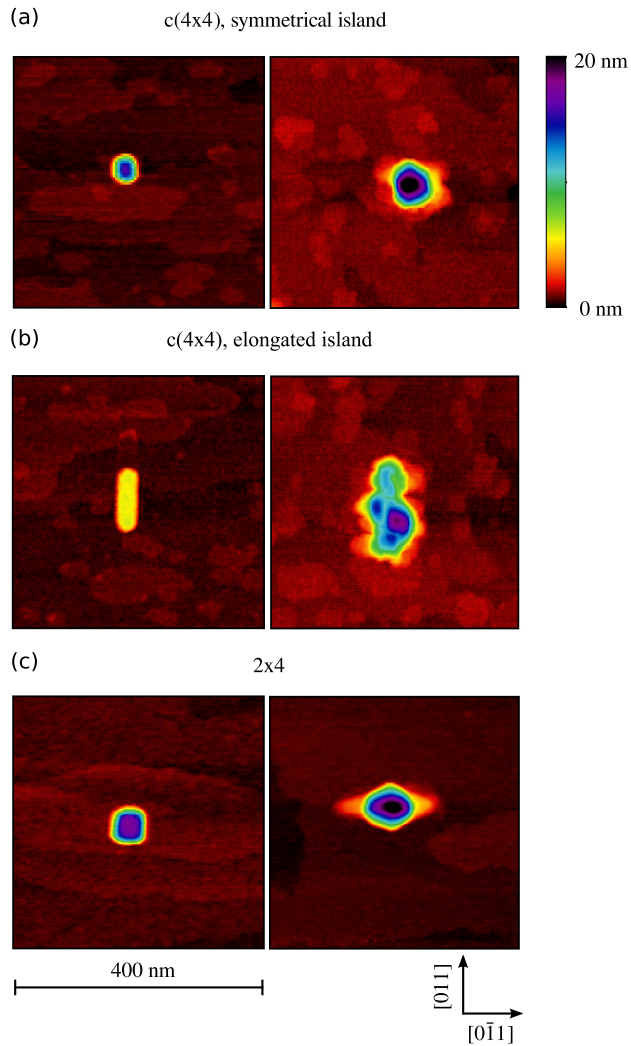


Figure 4.4: Single NC AFM study of the initial shape and surface reconstruction influence on the final QD morphology. Left images acquired after In deposition, and right after annealing for 10 minutes at 420 °C in As flux. (a) $c(4 \times 4)$ starting surface reconstruction, symmetric In NC, (b) $c(4 \times 4)$ starting surface reconstruction, elongated In NC, (c) (2×4) starting surface reconstruction.

low as 1 ML. Moreover, the observed surface roughness is lowest of all three cases. It has to be noted that the initial surface reconstruction does not influence the observed spotty RHEED pattern of the In NCs, which means that it does not have any influence on the In/GaAs crystallinity and epitaxial relationship. The In NCs in case of the (2x4) reconstruction (figure 4.3c) have a uniform square shape with average base size of 55 nm and mean height of 17 nm. Clearly, there is a trend of decreasing critical coverage for In NC formation with the decreasing amount of As on the initial GaAs surface. This is understandable, as excess As is first converted to InAs by impinging In atoms before metallic In NCs can form. The additional InAs does not form a smooth layer, but contributes to the increased roughness of the surface.

The starting surface reconstruction, as well as the initial NC morphology should have significant impact on the final shape of the InAs QD. This is demonstrated in figure 4.4, which shows the conversion of individual In NCs on the c(4x4) and (2x4) reconstructed GaAs surfaces (left images) to InAs annealed at 420 °C (right images). There is one-to-one In NC to InAs island correspondence, because the initial and final densities match. The InAs islands flatten and develop a local wetting layer elongated along $[0\bar{1}1]$. For the symmetric In NCs on the c(4x4) reconstructed surface (figure 4.4a) and in particular for the elongated In NCs (figure 4.4b) this results in a very distorted shape of the InAs islands and of the local wetting layer. Prolonged annealing and/or annealing at higher temperature lead to extension of this layer, further flattening of the QDs and finally complete collapse leaving only a quasi two-dimensional InAs layer (not shown here). This is understood by the fact that the total InAs coverage is lower than the critical thickness for QD formation in the SK growth mode, hence, the InAs islands are not stable. This, however, provides a very reproducible and robust means of controlling QD size and PL emission wavelength upon post-growth annealing, what shall be demonstrated in the following section for the symmetric QDs (figure 4.4c) obtained on the (2x4) reconstructed GaAs surface.

4.4 Optical properties

The results of LT PL measurements of the capped QD samples annealed for 1 and 10 minutes at 480 °C are presented in figure 4.5. They reveal clear ensemble emission peaks centered at 1030 and 925 nm, respectively. No wetting layer signal is observed at shorter wavelength for the 1030 nm sample, even at high excitation power density of 5 kW/cm². This fact indicates the absence of an optically active wetting layer. This finding is very important in view of more ideal zero-dimensional nanostructures with minimized interaction with their surroundings [21, 22]. For long anneals a PL signal at shorter wavelength attributed to the local wetting layer becomes clearly visible, what is consistent with the AFM

4 Conversion of In nanocrystals into quantum dots

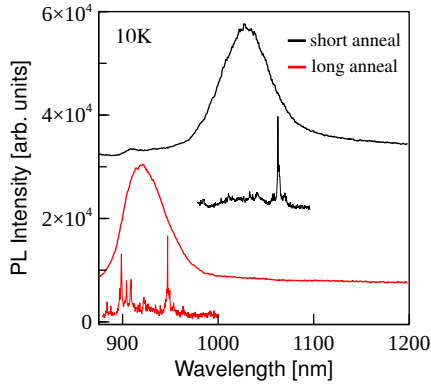


Figure 4.5: LT macro- and micro-PL spectra of the samples annealed for 1 minute (black) and for 10 minutes (red) at 480 °C. The curves are scaled and vertically offset for clarity.

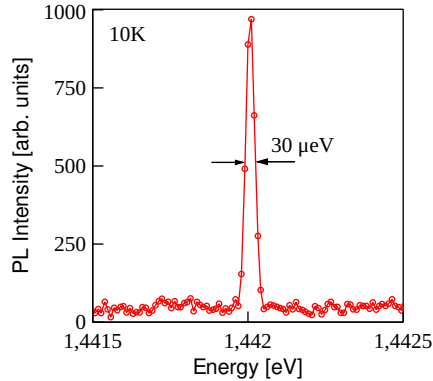


Figure 4.6: High-resolution LT micro-PL spectrum of an individual QD obtained by conversion of In NC.

observation of increasing local wetting layer with increasing annealing time. Micro-PL measurements, also presented in figure 4.5, show sharp and isolated emission lines from individual QDs. Due to the very low density, individual QDs are easily accessible without resorting to using masks or mesas. Additional high-resolution measurements (figure 4.6) reveal QD linewidths down to 30 μeV , what is the resolution limit of the used setup. This evidences that the approach of converting In NCs, deposited on As-poor GaAs surfaces, to InAs QDs reproducibly provides high quality QDs of low density required for applications in quantum functional devices.

The capped high density QD samples were characterized by RT PL spectroscopy. The result of this measurements is presented in figure 4.7. The observed emission band is centered at 1.26 μm and it is very broad

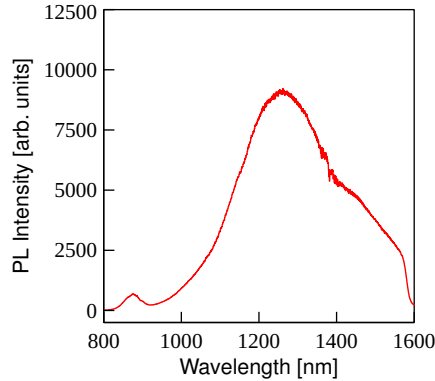


Figure 4.7: RT PL spectrum of a high density sample without annealing and with the initial capping layer grown at LT.

with a half-width of 350 nm. Interestingly, there is a significant PL signal around 1.5 μm and the emission extends beyond the 1.56 μm cut-off wavelength of the used liquid nitrogen-cooled InGaAs detector. Such long-wavelength emission is achieved without the use of strain-reducing InGaAs or InAlAs capping [23, 24]. This is a strong indication that even longer wavelengths could be achieved with the use of such capping layers. The large width of the observed PL peak suggests that the prolonged annealing step, which was not used in this case, has a large impact on the uniformity of the obtained QDs. It has to be noted at this point that for some applications broad emission is desirable. They include broadband semiconductor light sources, amplifiers and tunable lasers. Certainly, DE of InAs/GaAs QDs has a lot of potential to be used for the fabrication of such devices. Another very interesting feature of DE is the possibility to obtain long wavelength emission. Additional optimization and identification of the critical growth parameters is obviously necessary to further extend the wavelength range and improve the uniformity, however, the achieved results are already very promising. The unique features of DE could also be used in other material systems, for example in the case of InAs/InP to achieve emission beyond 2 μm [25], what is desirable for applications in semiconductor laser based gas sensing.

4.5 Summary

To conclude, the author demonstrated that conversion of In NCs into InAs is a suitable technique for the growth of low-density InAs QDs. The initial morphology of the In NCs depends strongly on the starting surface reconstruction and it was found that the most uniform structures were obtained for the (2x4) surface reconstruction. In this case the total InAs coverage for QD formation amounted to 1 ML, which is significantly less

than the InAs critical thickness for QDs grown in the SK mode. Capped QDs emit around 1 μm at low temperature, widely tunable upon post-growth annealing. No wetting layer emission was observed for samples with short annealing time. Micro-PL measurements revealed sharp and well isolated emission lines from individual QDs with linewidths down to 30 μeV . Additionally, broadband and long wavelength RT emission was demonstrated for higher density samples, proving large potential of DE to fabricate long-wavelength and broadband semiconductor light sources.

References

- [1] D. Press, T. D. Ladd, B. Zhang, and Y. Yamamoto, "Complete quantum control of a single quantum dot spin using ultrafast optical pulses," *Nature*, vol. 456, p. 218, 2008, 10.1038/nature07530.
- [2] X. Li, Y. Wu, D. Steel, D. Gammon, T. H. Stievater, D. S. Katzer, D. Park, C. Piermarocchi, and L. J. Sham, "An All-Optical Quantum Gate in a Semiconductor Quantum Dot," *Science*, vol. 301, p. 809, 2003.
- [3] W.-H. Chang, W.-Y. Chen, H.-S. Chang, T.-P. Hsieh, J.-I. Chyi, and T.-M. Hsu, "Efficient Single-Photon Sources Based on Low-Density Quantum Dots in Photonic-Crystal Nanocavities," *Physical Review Letters*, vol. 96, p. 117401, 2006.
- [4] S. Laurent, S. Varoutsis, L. L. Gratiet, A. Lemaitre, I. Sagnes, F. Raineri, A. Levenson, I. Robert-Philip, and I. Abram, "Indistinguishable single photons from a single-quantum dot in a two-dimensional photonic crystal cavity," *Applied Physics Letters*, vol. 87, p. 163107, 2005.
- [5] A. Imamoglu, D. D. Awschalom, G. Burkard, D. P. DiVincenzo, D. Loss, M. Sherwin, and A. Small, "Quantum Information Processing Using Quantum Dot Spins and Cavity QED," *Physical Review Letters*, vol. 83, p. 4204, 1999.
- [6] A. Badolato, K. Hennessy, M. Atature, J. Dreiser, E. Hu, P. M. Petroff, and A. Imamoglu, "Deterministic Coupling of Single Quantum Dots to Single Nanocavity Modes," *Science*, vol. 308, p. 1158, 2005.
- [7] N. P. Kobayashi, T. R. Ramachandran, P. Chen, and A. Madhukar, "In situ, atomic force microscope studies of the evolution of InAs three-dimensional islands on GaAs(001)," *Applied Physics Letters*, vol. 68, p. 3299, 1996.
- [8] B. Alloing, C. Zinoni, L. H. Li, A. Fiore, and G. Patriarche, "Structural and optical properties of low-density and In-rich InAs/GaAs quantum dots," *Journal of Applied Physics*, vol. 101, p. 024918, 2007.

- [9] T. Chikyow and N. Koguchi, "MBE Growth Method for Pyramid-Shaped GaAs Micro Crystals on ZnSe(001) Surface Using Ga Droplets," *Japanese Journal of Applied Physics*, vol. 29, p. L2093, 1990.
- [10] J. G. Keizer, J. Bocquel, P. M. Koenraad, T. Mano, T. Noda, and K. Sakoda, "Atomic scale analysis of self assembled GaAs/AlGaAs quantum dots grown by droplet epitaxy," *Applied Physics Letters*, vol. 96, 062101, p. 062 101, 2010.
- [11] E. Stock, T. Warming, I. Ostapenko, S. Rodt, A. Schliwa, J. A. Töfflinger, A. Lochmann, A. I. Toropov, S. A. Moshchenko, D. V. Dmitriev, V. A. Haisler, and D. Bimberg, "Single-photon emission from InGaAs quantum dots grown on (111) GaAs," *Applied Physics Letters*, vol. 96, 093112, p. 093 112, 2010.
- [12] T. Mano, M. Abbarchi, T. Kuroda, B. McSkimming, A. Ohtake, K. Mitsuishi, and K. Sakoda, "Self-Assembly of Symmetric GaAs Quantum Dots on (111)A Substrates: Suppression of Fine-Structure Splitting," *Applied Physics Express*, vol. 3, p. 065 203, 2010.
- [13] C. Somaschini, S. Bietti, N. Koguchi, and S. Sanguinetti, "Fabrication of Multiple Concentric Nanoring Structures," *Nano Letters*, vol. 9, p. 3419, 2009.
- [14] Z. Wang, K. Holmes, Y. Mazur, K. Ramsey, and G. Salamo, "Self-organization of quantum-dot pairs by high-temperature droplet epitaxy," *Nanoscale Research Letters*, vol. 1, p. 57, 2006, 10.1007/s11671-006-9002-z.
- [15] J. H. Lee, Z. M. Wang, N. W. Strom, Y. I. Mazur, and G. J. Salamo, "InGaAs quantum dot molecules around self-assembled GaAs nanomound templates," *Applied Physics Letters*, vol. 89, 202101, p. 202 101, 2006.
- [16] A. Urbančzyk, G. J. Hamhuis, and R. Nötzel, "In islands and their conversion to InAs quantum dots on GaAs (100): Structural and optical properties," *Journal of Applied Physics*, vol. 107, p. 014312, 2010.
- [17] T. Noda, T. Mano, and H. Sakaki, "Anisotropic Diffusion of In Atoms from an In Droplet and Formation of Elliptically Shaped InAs Quantum Dot Clusters on (100) GaAs," *Crystal Growth & Design*, vol. 11, p. 726, 2011.
- [18] T. Mano, T. Kuroda, K. Mitsuishi, T. Noda, and K. Sakoda, "High-density GaAs/AlGaAs quantum dots formed on GaAs (311)A substrates by droplet epitaxy," *Journal of Crystal Growth*, vol. 311, p. 1828, 2009.
- [19] C. Deparis and J. Massies, "Surface stoichiometry variation associated with GaAs (001) reconstruction transitions," *Journal of Crystal Growth*, vol. 108, p. 157, 1991.

- [20] J. Tersoff, D. E. Jesson, and W. X. Tang, "Running Droplets of Gallium from Evaporation of Gallium Arsenide," *Science*, vol. 324, p. 236, 2009.
- [21] A. Vasanelli, R. Ferreira, and G. Bastard, "Continuous Absorption Background and Decoherence in Quantum Dots," *Physical Review Letters*, vol. 89, p. 216 804, 2002.
- [22] C. Kammerer, C. Voisin, G. Cassabois, C. Delalande, P. Roussignol, F. Klopff, P. Reithmaier, A. Forchel, and J. M. Gérard, "Line narrowing in single semiconductor quantum dots: Toward the control of environment effects," *Physical Review B*, vol. 66, p. 041 306, 2002.
- [23] K. Nishi, H. Saito, S. Sugou, and J.-S. Lee, "A narrow photoluminescence linewidth of 21 meV at 1.35 μm from strain-reduced InAs quantum dots covered by $\text{In}_{0.2}\text{Ga}_{0.8}\text{As}$ grown on GaAs substrates," *Applied Physics Letters*, vol. 74, p. 1111, 1999.
- [24] J. Tatebayashi, M. Nishioka, and Y. Arakawa, "Over 1.5 μm light emission from InAs quantum dots embedded in InGaAs strain-reducing layer grown by metalorganic chemical vapor deposition," *Applied Physics Letters*, vol. 78, p. 3469, 2001.
- [25] J. Kotani, P. J. van Veldhoven, and R. Nötzel, "What Is the Longest Lasing Wavelength of InAs/InP (100) Quantum Dots Grown by Metal Organic Vapor Phase Epitaxy?," *Applied Physics Express*, vol. 3, p. 072 101, 2010.

5 Ag nanocrystals and hybrid quantum dot-Ag nanocrystal structures

In the current chapter the author demonstrates the growth of high quality epitaxial Ag NCs by MBE on GaAs. By changing suitable deposition parameters such as substrate temperature and Ag deposition rate their size and density can be controlled, thus allowing for tuning of their LSPR over a wide wavelength range. What is more, the author shows that it is possible to position such Ag NCs on individual, low density near-surface InAs QDs with very high yield. PL measurements of such hybrid structures show clear enhancement of the intensity of the emitted light.

5.1 Why In is not enough?

It was shown in chapter 3 that using MBE one can obtain epitaxial In NCs that self-align due to strain-driven ad-atom migration on both capped and uncapped InAs QDs. This result is a very important proof of concept of the epitaxy-based bottom-up fabrication of plasmonic nanostructures, however, other metals are more suitable for practical applications. In particular, Ag is the material with the lowest resistive losses of all metals [1]. It also has a much lower ω_p facilitating easier tuning of the LSPR into the NIR wavelength range, and it is very chemically stable. Additionally, Ag has a higher melting point than In (961 versus 156 °C [2]), what allows to deposit the metal NCs at higher substrate temperatures. This fact enables much better control and reproducibility of the process. Last but not least, the investigation of the formation of different metal NCs and their ordering on semiconductor QDs is necessary in order to prove the universality of the bottom-up approach to fabricate active and passive plasmonic nanostructures presented by the author.

5.2 Experimental details

All investigated samples were grown using a custom solid source MBE system with an additional metal deposition chamber on undoped, singular, (100)-oriented GaAs substrates. After thermal oxide desorption under As_4 flux at 580 °C, a 200 nm thick GaAs buffer layer was grown. Ag NCs

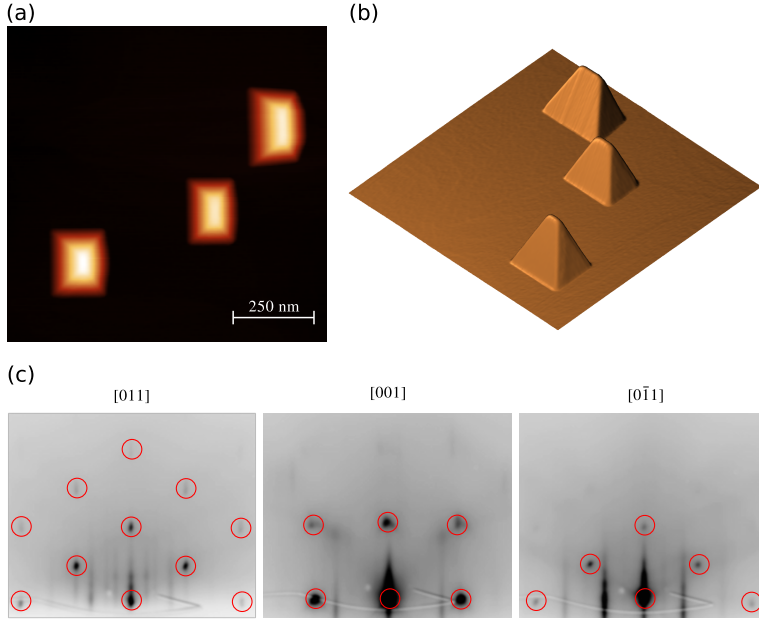


Figure 5.1: Typical AFM images of Ag NCs on GaAs (a). The characteristic hut-like shape and well-developed facets can be clearly seen in a 3D image of the AFM data (b). RHEED patterns (c) prove the crystallinity of the NCs. Red circles mark the diffraction spots that appear after metal deposition.

were deposited on both plain GaAs, and low density, near-surface InAs QDs. The QDs were grown by converting In NCs to InAs as described in chapter 4. One ML In was deposited at 100 °C to form In NCs, which were transformed into InAs QDs by annealing under As_4 flux, initially at 100 °C, and then at 450 °C. At this temperature the QDs were capped with a GaAs layer of 3 nm thickness. For Ag NC growth the samples were transferred into the metal deposition chamber. The substrate temperature was kept between 250 and 300 °C, the growth rate was 0.1 nm/min and the Ag coverage amounted to 0.5–2 nm. The Ag growth rate was calibrated by surface profilometry of a thick quasi-2D Ag layer grown at low substrate temperature. Both metal and III-V deposition was monitored by RHEED. The morphology of the samples was characterized by tapping-mode AFM under ambient conditions. The LSPR wavelength of the Ag NCs was measured by polarization-resolved DR spectroscopy. Additionally, the hybrid NC-QD structures were investigated by LT micro- and macro-PL spectroscopy at 10 K.

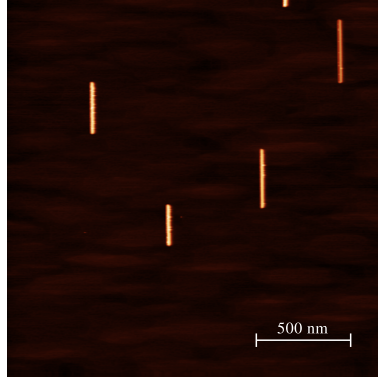


Figure 5.2: AFM image of Ag NCs obtained for coverage of only 0.003 nm.

5.3 Structural properties of Ag nanocrystals

Provided that the starting GaAs surface is clean, that is it has no native oxide, regular metal NCs with clear facets and well-defined epitaxial relation form during Ag deposition. This is confirmed both by AFM and RHEED measurements presented in figure 5.1. The NCs have a characteristic hut-like shape and are elongated preferentially in the [011] direction. This is also observed in the case of other substrates, namely Si [3], as well as in the case of deposition of In on GaAs, as described in the previous chapter. The Ag NCs are bound by {011} facets and for the investigated growth conditions their in-plane and out-of plane epitaxial relations are $(100)_{\text{Ag}} \parallel (100)_{\text{GaAs}}$ and $[001]_{\text{Ag}} \parallel [001]_{\text{GaAs}}$, respectively. This result is deduced from the RHEED data presented in figure 5.1c and is in accordance with reports found in the literature [4]. The deposition of Ag does not deteriorate the quality of the GaAs surface, as evidenced by the AFM data, however, sometimes a change in surface reconstruction is observed indicating the formation of thin Ag wetting layer. This is also confirmed by previous studies that identify Ag/GaAs as a material system supporting SK growth [5].

5.4 Shape, size and density control

MBE technology allows for very precise control of all relevant deposition process conditions, and this, in turn, enables very precise control of the size and density of the grown Ag NCs. The intuitively expected trend is observed – increase of the substrate temperature leads to increase of the average NC size and to decrease of the density due to higher adatom mobility [6]. On the other hand, higher coverage results in larger NCs and higher density. By controlling both parameters it is possible to achieve the desired average size and density, what is important for tuning of the

LSPR to a specific wavelength.

The natural tendency of the Ag NCs to elongate in the [011] direction causes that their exact shape, that is aspect ratio, varies a lot. Certainly it would be beneficial to control this in order to synthesize NCs with the desired aspect ratio, a parameter of great importance in the context of the optical properties. Preliminary results shown in figure 5.2 reveal that for very small coverages of the order of 0.003 nm, only very high aspect ratio NCs are formed. This effect can be used to achieve some control of the Ag NC shape, however, further investigations are necessary to understand the mechanism behind this phenomenon. It would be also beneficial to control the elongation direction of the NCs. This is possible by growing Ag NCs on QD templates, as will be discussed later in the current chapter. Additionally, it should be possible to obtain shapes other than huts by using different GaAs substrate orientations like (111)B or (311)B.

5.5 Optical properties

The results of the DR measurements and corresponding AFM data are presented in figure 5.3. In accordance with theoretical predictions there is a clear tendency of the LSPR peak to red-shift with increasing NC size. The demonstrated tuning range is quite impressive – the peak positions span from around 960 nm to 1.7 μm , covering both the 1.3 and 1.5 μm telecommunication bands. The LSPR peak widths are much smaller than in case of In, what is the consequence of the large reduction of resistive losses in Ag. Polarization resolved reflectivity measurements reveal a 100-200 nm splitting of the LSPR peak because of the symmetry breaking of the metal NCs due to the preferential elongation along [011]. As expected from theory, the long wavelength peak is observed for light polarized along [011]. Moreover, this peak is usually much wider than the one observed for the orthogonal polarization, which is partially due to higher radiation damping, that increases with size, but also because of higher inhomogeneous broadening due to varying Ag NC lengths. The latter is also the most likely reason for a significant asymmetry of the long-wavelength resonance, clearly visible in figure 5.3c.

5.6 Positioning on individual quantum dots

It was already demonstrated in chapter 3, that it is possible to position In NCs on capped and uncapped QDs. This approach is based on lattice mismatch, and thus it works very well in the case of Ag too, as shown in figure 5.4. For Ag the author decided to concentrate on positioning of low density NCs on low density QDs with the ultimate goal of investigating individual NC-QD pairs. The ordering process is depicted schematically in figure 5.4a. It can be very efficient with ordering yields approaching

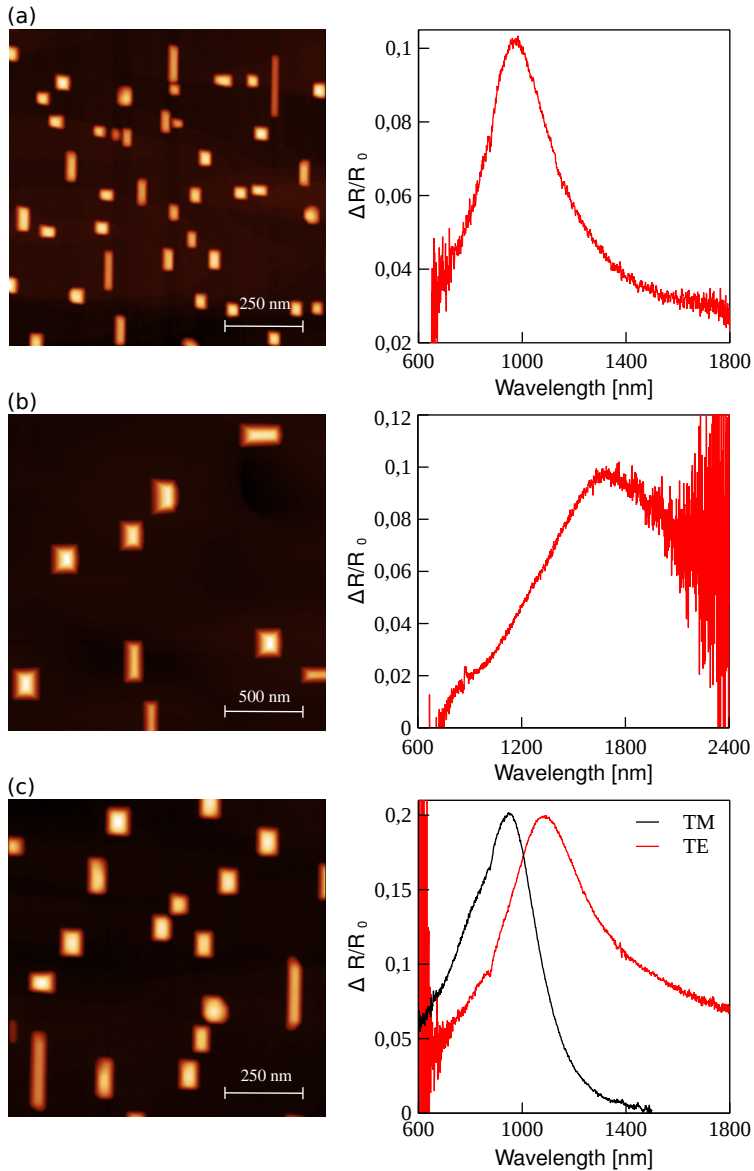


Figure 5.3: DR spectra (right panels) and corresponding AFM data (left panels) of different Ag NC samples. In (a) the coverage was 0.5 nm and the substrate temperature 250 °C, in (b) they amounted to 2 nm and 300 °C, and in (c) to 1 nm and 275 °C. In the last case the splitting of the LSPR due to anisotropy of the Ag NCs is clearly visible.

100% provided that the NC density matches the density of the QDs. In the presented structures it was possible to match the NC and QD density

5 Ag nanocrystals and hybrid quantum dot-Ag nanocrystal structures

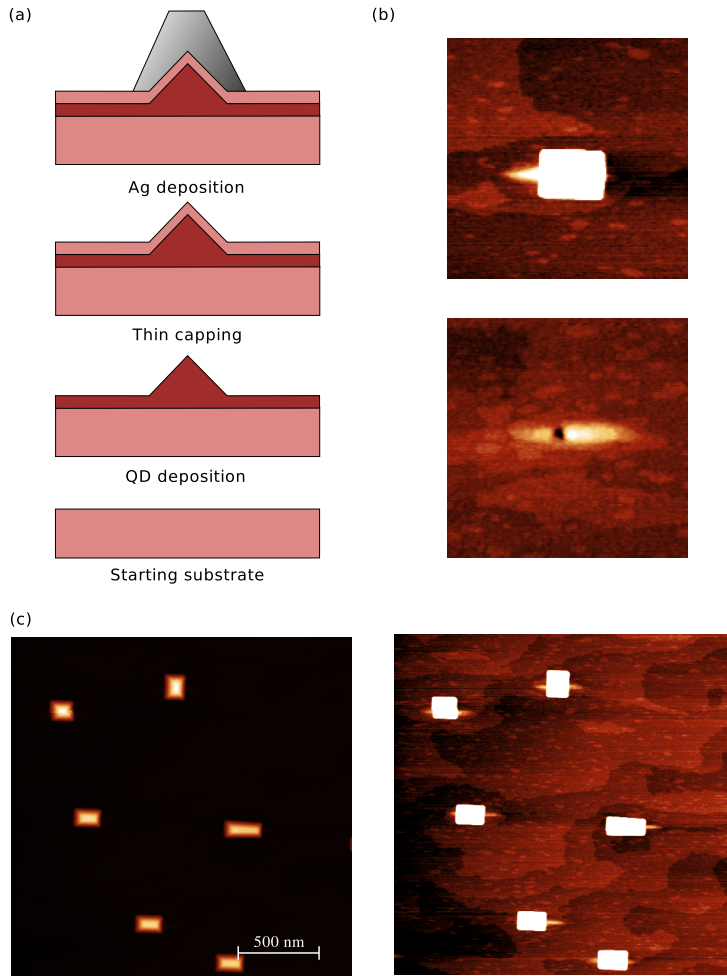


Figure 5.4: Growth steps for achieving alignment of single Ag NCs on individual QDs (a) and results of AFM measurements of such ordered structures (b,c). In case of (c), the right image has an expanded scale, so the QDs protruding from beneath of the Ag NCs can be seen.

within 10%. Under such conditions there are no unpaired structures visible over large areas, what is clearly seen in figure 5.4c. This is very important if one wants to consider single-structure investigations. Additionally, the presence of near-surface QDs affects strongly the shape of the metal NCs. They change the elongation direction from $[011]$ to $[0\bar{1}1]$, that is the elongation direction of the QDs. This is a very important result in the context of shape control of the Ag NCs and allows to engineer the polarization of the LSPR.

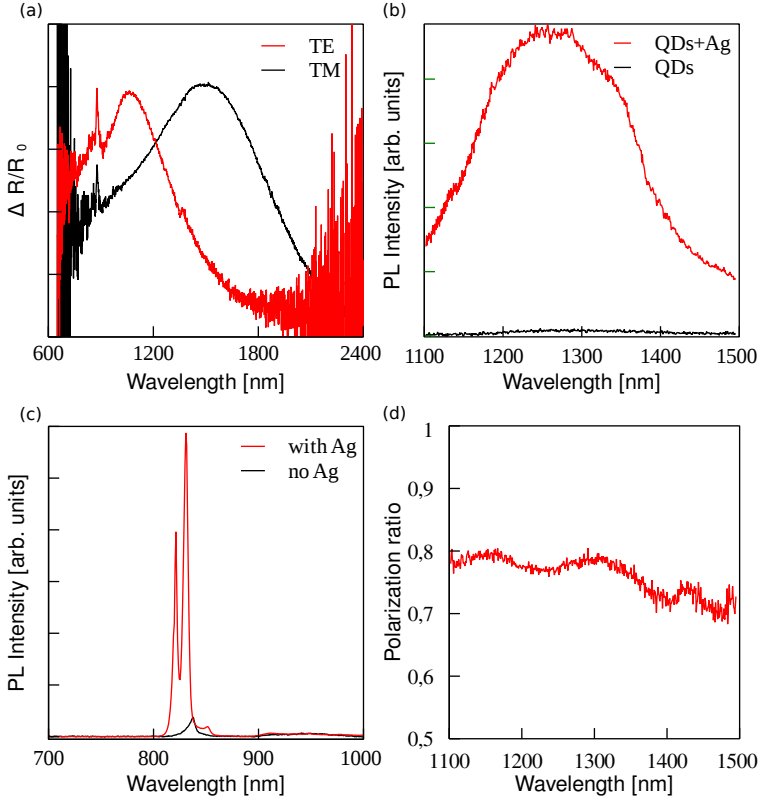


Figure 5.5: Polarization resolved DR spectra of the sample with Ag NCs positioned on InAs QDs (a), LT PL emission spectra of that sample and the reference one without Ag NCs, the bulk GaAs PL spectra (c), as well as the polarization ratio of the ordered NC sample (d).

5.7 Optical properties of hybrid structures

The results of the DR measurements of the hybrid structures are presented in figure 5.5a. The change of the elongation direction of the metal NCs discussed in the previous section results in reversed ordering of the LSPR modes. What is more, the splitting of the peaks is significantly larger than one usually observed for samples without QDs, 200 versus 100 nm, respectively. This might be due to larger average aspect ratio and also due to the presence of the QDs affecting the metal NCs with their higher refractive index.

The low temperature PL measurements reveal very strong increase of the QD as well as bulk GaAs signal compared to a reference structure without any Ag. It is tempting to interpret this effect as emission enhancement due to the interaction with the LSPR. Due to the strong anisotropy of the metal NCs shapes and corresponding polarization

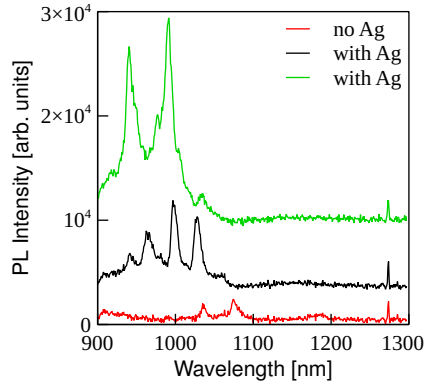


Figure 5.6: LT micro-PL of a sample with and without Ag on top of the QDs. In the case of the Ag sample the two measurements are taken under the same conditions at two different sites.

dependent LSPR peak positions, strongly polarization dependent QD emission would be expected in that case. This, however, is not observed as seen in figure 5.5d. The PL emitted by the QDs has no features in the polarization degree coinciding with the position of the LSPR peaks. Additionally, there are no characteristic features in the PL peak itself, what is an additional argument against such interpretation. Analysis of the coverage of the Ag NCs reveals that they take only 2% of the area of the wafer. Taking into account this and the high degree of localization of the LSPR, one can conclude that the high enhancement of the bulk GaAs emission cannot be attributed to plasmonic emission enhancement. Most probably, the observed PL enhancement is due to enhanced absorption of the exciting laser light, and thus enhanced local electron-hole pair injection. This would explain very well the lack of polarization dependence of the observed effect and the absence of specific spectral features corresponding to the LSPR that were observed in case of In NCs.

No individual QD lines could be resolved by micro-PL in the samples discussed above. Clear individual QD lines could be measured for a sample with low-density SK QDs and Ag NCs. The results are presented in figure 5.6. A clear enhancement of the QD signal is visible. The linewidths are significantly broader than those observed for high quality, buried QDs and they correspond well to what was measured in the case of hybrid structures with In. The broadening is obviously expected due to the close proximity of the sample surface, which is usually associated with abundance of defects. The amount of enhancement and the positions of the individual lines vary when different sites are measured. The former being most likely due to different efficiencies of metal-emitter coupling. This result is very promising, as alone the measurements of low-density and near-surface single QDs are very challenging. Obviously

further investigations are necessary to fully understand what is the exact enhancement mechanism in this case. Perfect characterization methods allowing to address this problem would be time-resolved measurements and near-field optical microscopy.

5.8 Summary

In conclusion, the author demonstrated the epitaxial growth of Ag NCs on GaAs that support LSPR tunable over a wide wavelength range including the important telecom bands. What is more, ordering of Ag NCs on near-surface QDs with very high yield was also demonstrated. These results prove the universality of the bottom-up approach for the fabrication of active plasmonic nanostructures such as spasers, optical transistors or switches. PL investigations show large enhancement of the light emitted by the QDs and the GaAs bulk. This is attributed to enhanced absorption of the exciting light. Additional micro-PL measurements revealed promising results regarding individual QD lines that were significantly stronger compared to those for reference samples without Ag NCs.

References

- [1] E. J. Zeman and G. C. Schatz, "An accurate electromagnetic theory study of surface enhancement factors for silver, gold, copper, lithium, sodium, aluminum, gallium, indium, zinc, and cadmium," *The Journal of Physical Chemistry*, vol. 91, p. 634, 1987.
- [2] W. Haynes and D. Lide, *CRC handbook of chemistry and physics*. Taylor & Francis Group, 2010.
- [3] M. Hanbücken, M. Futamoto, and J. Venables, "Nucleation, growth and the intermediate layer in Ag/Si (100) and Ag/Si (111)," *Surface Science*, vol. 147, p. 433, 1984.
- [4] J. Massies and N. T. Linh, "On the growth of silver on GaAs {001} surfaces," *Journal of Crystal Growth*, vol. 56, p. 25, 1982.
- [5] R. Ludeke, T.-C. Chiang, and D. E. Eastman, "Crystallographic relationships and interfacial properties of Ag on GaAs (100) surfaces," *Journal of Vacuum Science and Technology*, vol. 21, p. 599, 1982.
- [6] J. Venables, *Introduction to Surface and Thin Film Processes*. Cambridge University Press, 2000.

6 Positioning of Ag nanocrystals on patterned substrates

In this chapter the author demonstrates the site-controlled growth of epitaxial Ag NCs on patterned GaAs substrates by MBE with high degree of long-range uniformity. The alignment is based on lithographically defined holes with 10 μm pitch in which InAs QDs are grown. The Ag NCs align preferentially on top of the InAs QDs. No such ordering is observed in the case of bare patterned substrates, proving that the ordering is strain-driven. The presented technique facilitates the placement of active plasmonic structures at arbitrarily defined positions enabling single structure investigations and more importantly their integration into complex devices and circuits.

6.1 Importance of long-range ordering

Plasmonics is developing very quickly and it already provided significant contributions in the fields of biosensing [1, 2] or energy conversion [3]. However, it is still necessary to develop new, and perfect existing methods of synthesis and fabrication of complex structures consisting of many elements. This is especially important in the context of the increasing interest in active plasmonics [4–7], where one combines metallic nanostructures together with active media in order to obtain new functionalities including the generation of light through spasing [8–11], loss-compensated surface plasmon propagation and amplification [12], as well as ultrafast all-optical switching [5, 13]. Such active elements are of nanoscale dimensions, and if they were integrated together into one device or circuit they could offer performance comparable or superior to integrated electronics [14] and perhaps additional new functionalities [15]. This, however, requires highly reproducible fabrication of individual metallic structures with high quality in order to control their optical properties [16], positioning of the metal with respect to the active structures with single nanometer precision necessary for optimum coupling [17], as well as arbitrary positioning on large length scales in order to enable integration of different plasmonic devices. The author showed in the previous chapters that it is possible to grow by MBE epitaxial metal NCs of In and Ag that support LSPRs in the NIR wavelength range. Such NCs can self-align due to strain driven migration on top of optically active near-surface QDs. This self-assembly phenomenon offers a route

6 Positioning of Ag nanocrystals on patterned substrates

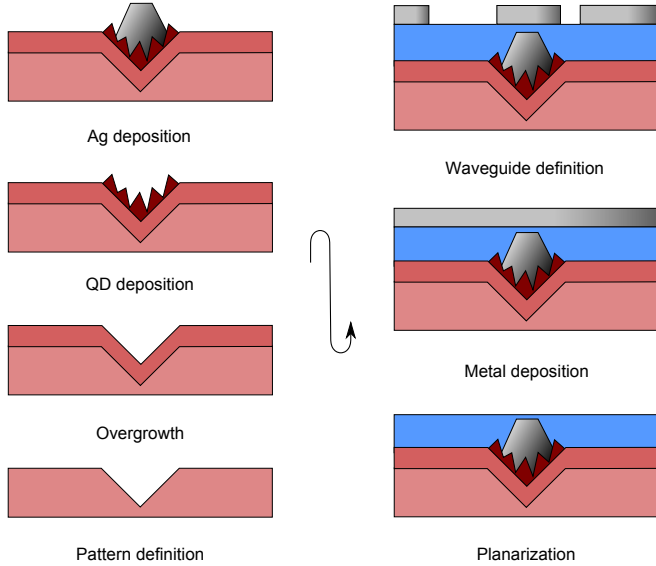


Figure 6.1: Proposed process flow for integrating self-assembled active Ag NC-InAs QD structures. In CMOS terminology the right column is a frontend-like part demonstrated in the thesis. The left one is a backend-like.

to synthesize individual active plasmonic nanostructures. Self-assembly has however one drawback, it cannot allow for arbitrary placement of structures on the substrate. It facilitates long-range ordering, but only for relatively simple periodic arrangements and with high spatial frequencies [18]. That is why it is necessary to consider hybrid approaches utilizing both bottom-up, as well as top-down methods like it is done in the case of SK QD positioning [19, 20].

In this chapter the author proposes to use guided self-assembly of epitaxial Ag NCs on lithographically defined structures. It is demonstrated that the Ag NCs grow preferentially on near surface QDs that are placed in etched holes. This allows for simultaneous precise QD-Ag NC coupling by controlling the capping layer thickness and long-range ordering of such hybrid structures with large NC separations and very good yield. After the coupled QD-Ag structures are synthesized at the desired positions, they can be planarized with a thin dielectric layer for additional deposition of a metal film and further processing as depicted in figure 6.1. Such a process flow is in direct analogy to one used for the fabrication of integrated electronic circuits, when first the active devices are defined (frontend of line), and then the interconnects are fabricated (backend of line). Defining passive plasmonic waveguides connecting the active structures would enable truly integrated active plasmonic circuitry. What is more, ordering of active plasmonic nanostructures with high

degree of precision and large NC separations allows for easy and reproducible single structure investigations – an additional gain that cannot be overlooked.

6.2 Experimental details

All investigated samples were grown using a custom solid source MBE system with additional metal deposition chamber on undoped, singular, (100)-oriented GaAs substrates. The patterns were obtained using contact lithography with a Karl Suss MA-6 mask aligner operating at the wavelength of 405 nm. Hole arrays with 10 μm pitch were defined in a positive photo resist (PR) layer (HPR-504, 0.5 μm thick) with diameters of 1 and 2.5 μm on the same wafer. This pattern was transferred onto the GaAs substrate by chemical etching in 40:1 citric acid:hydrogen peroxide, where the citric acid was a 50% aqueous solution of the corresponding monohydrate. The etching depth of the features was 70 nm. The cleaning procedure after processing included stripping of the PR in acetone, O_2 plasma cleaning, 10 minute dip in concentrated H_2SO_4 and final rinsing with copious amounts of deionized water. The MBE growth began with thermal oxide removal at 580 $^\circ\text{C}$. Afterwards, a 100 nm GaAs buffer layer was deposited at 520 $^\circ\text{C}$. In order to obtain better surface morphology, the III/V ratio was adjusted during the GaAs growth so that a (2x4) surface reconstruction was visible by RHEED. Later, 1.6 ML of InAs was deposited with growth rate of 0.002ML/s what resulted in QD formation only inside of the etched holes. In practice, it is challenging to determine the exact InAs growth rate due to thermal desorption of In, so the growth rate estimation was based on RHEED. The InAs deposition was stopped just at the onset of the 2D to 3D RHEED transition. The QDs were capped with a 6 nm thick layer of AlAs. All the III-V growth was performed under As_4 flux. At this point the sample was cooled and transferred to the Ag deposition chamber. Approximately 0.1 ML Ag was deposited with the growth rate of 0.01 ML/minute and at a substrate temperature around 350–400 $^\circ\text{C}$. It has to be noted at this point that the growth rate measurements are burdened with a significant experimental error due to the extremely low value. It was obtained by extrapolating the growth-rate versus beam-flux dependence known quite accurately for higher values. On the other hand, the run to run beam-flux readings were exactly reproducible, proving very good flux stability. Such low growth rate and high temperature were chosen to obtain a low nucleation density, preventing excess Ag NCs between the lithographically defined holes. Finally, the samples were cooled and taken out of the MBE system. They were characterized by room temperature micro-PL and their surface morphology was measured using tapping-mode AFM under ambient conditions. Large scanning areas used made those measurements more demanding than usual. Excessive tip-wear during such long scans

resulted sometimes in slightly distorted shapes of the Ag NCs.

6.3 Ordering

The results of the AFM measurements on the large holes are presented in figures 6.2 and 6.3. Clearly, in the case of the structures with QDs, the Ag NCs position on the sidewalls of the holes, where the QDs nucleated. The relatively high InAs deposition temperature and sub-critical coverage cause that QDs grow only at the side-walls of the etched holes. Moreover, they prefer the $\{11\bar{1}\}$ B-like facet. As seen in the figure 6.3a, the NCs follow the QDs. In the case of the bare structure without any deposited InAs, no ordering is observed, as clearly depicted in figures 6.2b and 6.3b. The significant roughness of the side-walls does not facilitate preferential nucleation of Ag. In the whole measurement area there are no Ag NCs positioned on the sidewalls, what is consistent with the low relative area of the sidewalls compared to the flat surface area. This fact clearly demonstrates that the morphology is not the driving force behind the observed ordering as in the case of InAs. It is strain-driven – the NCs can accommodate the lattice mismatch more easily on sites with near-surface InAs QDs.

Despite the bottom-up nature of the ordering process, it is highly reproducible. On a $25 \times 25 \mu\text{m}^2$ area no Ag NCs are found on the flat surface between the holes, which constitutes the majority of the scanned area. Interestingly, AFM measurements (data not shown) performed on unprocessed areas of the same sample reveal a much lower NC density with bigger size than on the patterned areas, 0.001 per μm^2 and 150 nm versus 0.005 per μm^2 and 40 nm, respectively. This demonstrates that patterned substrates in addition to position control, allow to control the size and density of the metal NCs, what is important for obtaining desired LSPR wavelength. According to the data on the optical properties of Ag NCs on GaAs presented in chapter 5, the NCs of the size obtained in the patterned areas support LSPR in the desired near-infrared wavelength range coinciding with the QD emission wavelength.

Due to relatively high area of the sidewalls as compared to the average base size of Ag NCs, the demonstrated positional accuracy of the ordering has a significant random component. This issue can be solved by decreasing the hole size. Doing so decreases the sidewall area available for preferential nucleation of the Ag NCs. For the initial hole size of $1.5 \mu\text{m}$ the AFM measurement results are presented in figure 6.4a. After overgrowth the initially round holes change into prolate-shaped ones. This is due to anisotropic surface diffusion of GaAs, which has a much higher rate in the $[0\bar{1}1]$ direction [21]. This causes faster closing of the holes in this direction, ultimately resulting in the disappearance of the planar areas at the bottom of the holes. Only the sidewalls remain, what allows for much more precise positioning of the Ag NCs. Additionally,

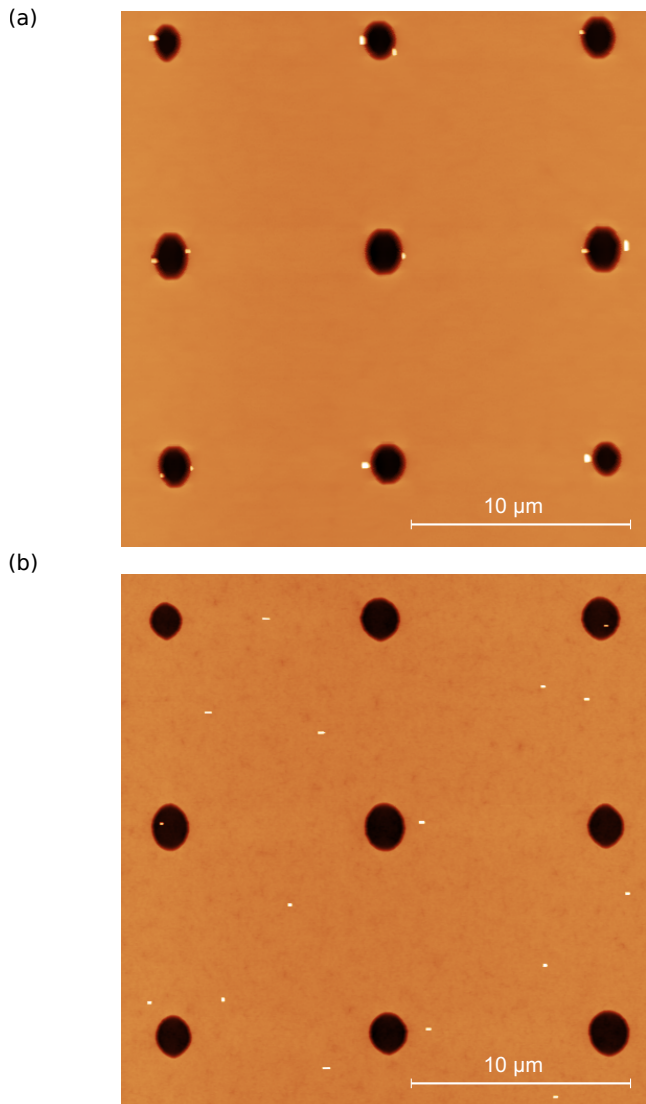


Figure 6.2: AFM measurements of sample with (a) and without (b) QDs. Ordering of the Ag NCs (white rectangles) is observed only in the former case. Both scan fields are 25 by 25 μm^2 .

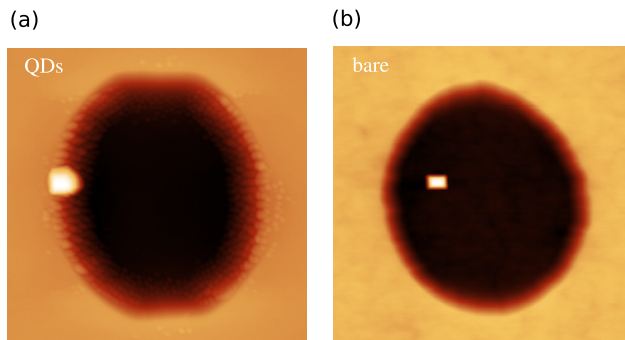


Figure 6.3: AFM images of individual holes with (a) and without (b) QDs. In both cases the scan fields are 4 by 4 μm^2 . In case of (a) the slightly distorted NC shape is due to tip wear.

statistical analysis of the nucleation sites reveals that the NCs prefer the symmetry axis of the hole in 60 % of the cases, what is shown in figure 6.4b. This increases further the placement accuracy, as well as opens up a possibility of rational design of the hole shape in order to achieve complex structures like NC dimers.

In order to demonstrate the feasibility of truly nanoscale positioning accuracy, it was necessary to overcome the resolution limitations of the used lithographic process. This was achieved by intentional underexposure of the patterns. In case of the 2.5 μm diameter holes the PR layer was not fully open and instead two adjacent submicron holes were created. The holes after overgrowth had an average size of 600 by 400 nm and the already discussed asymmetric shape. The observed positional accuracy was usually better than this value, because the Ag NCs nucleated preferentially on the symmetry axis of the hole along the [011] direction. As seen in figure 6.4c, it was then possible to obtain paired Ag NCs with submicron separation, what is an important step towards lithographically controlled synthesis of nanoantenna structures.

6.4 Room temperature photoluminescence emission

The results of the PL measurements are presented in figure 6.5. At room temperature and under ambient conditions the QDs emit strongly around 950 nm despite their close proximity to the sample surface. Unfortunately under constant laser light irradiation their optical properties deteriorate very quickly. After 30 s of laser irradiation, the PL signal from the QDs disappears almost completely. This is most likely due to local heating of the sample and oxidation of the thin AlAs capping layer that, in turn, causes excessive non-radiative recombination. Moreover, the author

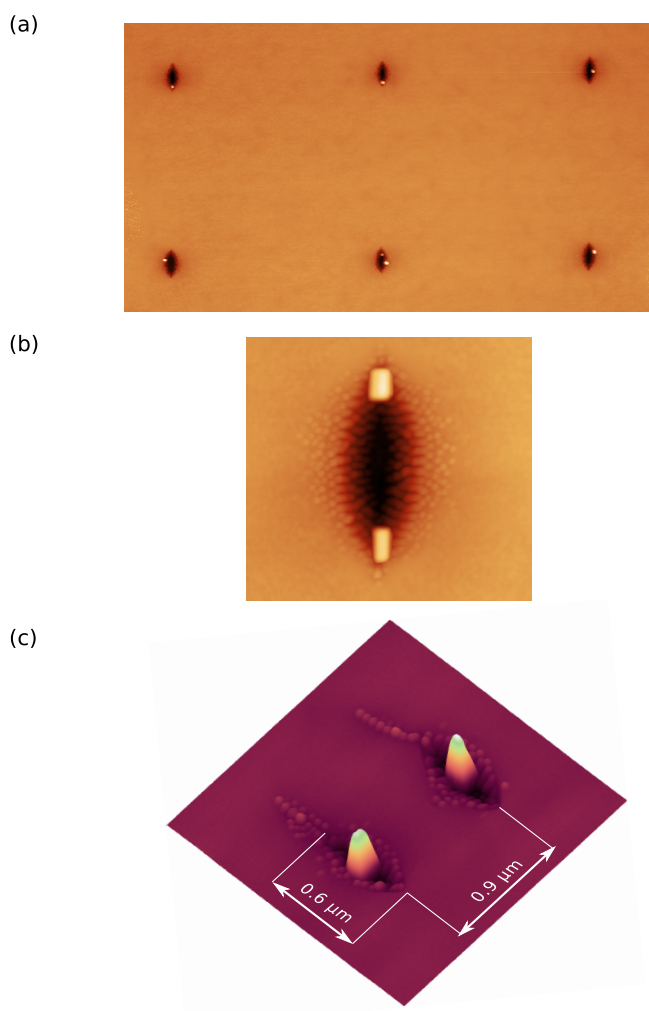


Figure 6.4: Results of scaling down of the hole size. More precise position control can be achieved (a). The Ag NCs tend to nucleate on the symmetry axis of the hole (b). Ultimately submicron accuracy is possible (c).

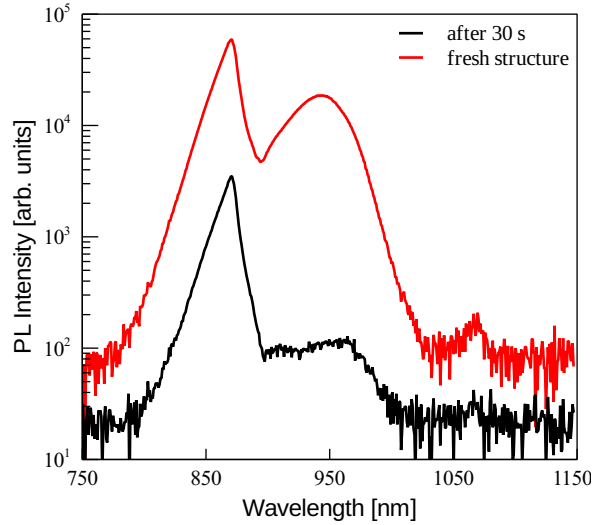


Figure 6.5: Room temperature micro-PL measurements of a single hole taken before (black) and after (red) 30 s of laser light irradiation. The curves are vertically offset for clarity.

observed that the samples deteriorate under ambient conditions also without any external stimulus, however on longer timescales of a few weeks. This result illustrates the importance of a good surface passivation for obtaining stable structures that can be characterized without resorting to special means like storage under inert gas atmosphere.

6.5 Challenges

Ultimately, in order to achieve sub 10 nm positioning accuracy it is necessary to scale-down the hole size even further. This can be done by using for example high resolution optical lithography, EBL or NIL, and should not pose much difficulties. On the other hand, the author thinks that much more investigations are necessary to fully understand how the hole size and shape influence the nucleation of the NCs in order to enable efficient synthesis of dimers and other complex structures. An additional important issue is the control of the hole morphology during the overgrowth process. Usually it is necessary to deposit a buffer layer, so the defects associated with the processed GaAs interface do not influence the QDs. This, as already discussed, inevitably changes the hole shape. One of the important facts in this context is the anisotropic surface diffusion, thus it might be beneficial to use in further studies growth under As_2 flux in order to prevent the anisotropic deformation of the holes after GaAs overgrowth [22–24]. This would allow for fine tuning of

the hole size by changing the buffer layer thickness. Probably even more could be achieved by deliberately switching on and off the anisotropy by changing the group V species during overgrowth. Finally, finding a suitable planarization method that would prevent the deterioration of the optical properties of the QDs due to aging is necessary. One particularly appealing solution would be the use of spin-on glass [25] due to its inherent processing simplicity and low cost. However, a lot of investigations are necessary to test and optimize the passivating properties of such a treatment.

6.6 Summary

To conclude, the author demonstrated site controlled growth of Ag NCs using lithographic patterning and strain-driven preferential nucleation on top of near surface InAs QD. With reducing size of the holes submicron precise positioning could be achieved together with single nanometer precise control over the near surface InAs QD to Ag NC distance. This allows for both long-range ordering of the NCs, as well as optimizing the Ag-QD coupling versus the non-radiative losses. Furthermore, the author clearly proved the feasibility of epitaxial growth for the fabrication of ordered and reproducible arrays of InAs QD–Ag NC hybrids, which easily facilitate single structure investigations. Furthermore, the author believes that the presented technique allows to integrate active plasmonic structures with passive plasmonic waveguides enabling complex LSPR-based devices.

References

- [1] K. M. Mayer and J. H. Hafner, “Localized Surface Plasmon Resonance Sensors,” *Chemical Reviews*, vol. 111, p. 3828, 2011.
- [2] J. Homola, “Surface Plasmon Resonance Sensors for Detection of Chemical and Biological Species,” *Chemical Reviews*, vol. 108, p. 462, 2008.
- [3] H. A. Atwater and A. Polman, “Plasmonics for improved photovoltaic devices,” *Nature Materials*, vol. 9, p. 205, 2010.
- [4] K. F. MacDonald and N. I. Zheludev, “Active plasmonics: current status,” *Laser & Photonics Reviews*, vol. 4, p. 562, 2010.
- [5] M. Abb, P. Albella, J. Aizpurua, and O. L. Muskens, “All-Optical Control of a Single Plasmonic Nanoantenna–ITO Hybrid,” *Nano Letters*, vol. 11, p. 2457, 2011.
- [6] A. Boltasseva and H. A. Atwater, “Low-Loss Plasmonic Metamaterials,” *Science*, vol. 331, p. 290, 2011.

- [7] M. I. Stockman, "The spaser as a nanoscale quantum generator and ultrafast amplifier," *Journal of Optics*, vol. 12, p. 024 004, 2010.
- [8] M. A. Noginov, G. Zhu, A. M. Belgrave, R. Bakker, V. M. Shalaev, E. E. Narimanov, S. Stout, E. Herz, T. Suteewong, and U. Wiesner, "Demonstration of a spaser-based nanolaser," *Nature*, vol. 460, p. 1110, 2009.
- [9] R. F. Oulton, V. J. Sorger, T. Zentgraf, R.-M. Ma, C. Gladden, L. Dai, G. Bartal, and X. Zhang, "Plasmon lasers at deep subwavelength scale," *Nature*, vol. 461, p. 629, 2009.
- [10] M. A. Noginov, G. Zhu, M. Mayy, B. A. Ritzo, N. Noginova, and V. A. Podolskiy, "Stimulated Emission of Surface Plasmon Polaritons," *Physical Review Letters*, vol. 101, p. 226 806, 2008.
- [11] P. Berini and I. De Leon, "Surface plasmon-polariton amplifiers and lasers," *Nature Photonics*, vol. 6, p. 16, 2012.
- [12] J. Grandidier, G. C. des Francs, S. Massenot, A. Bouhelier, L. Markey, J.-C. Weeber, C. Finot, and A. Dereux, "Gain-Assisted Propagation in a Plasmonic Waveguide at Telecom Wavelength," *Nano Letters*, vol. 9, p. 2935, 2009.
- [13] N. Large, M. Abb, J. Aizpurua, and O. L. Muskens, "Photoconductively Loaded Plasmonic Nanoantenna as Building Block for Ultracompact Optical Switches," *Nano Letters*, vol. 10, p. 1741, 2010.
- [14] R. Zia, J. A. Schuller, A. Chandran, and M. L. Brongersma, "Plasmonics: the next chip-scale technology," *Materials Today*, vol. 9, p. 20, 2006.
- [15] Z. Jacob and V. M. Shalaev, "Plasmonics Goes Quantum," *Science*, vol. 334, p. 463, 2011.
- [16] P. Biagioni, J.-S. Huang, and B. Hecht, "Nanoantennas for visible and infrared radiation," *Reports on Progress in Physics*, vol. 75, p. 024 402, 2012.
- [17] P. Anger, P. Bharadwaj, and L. Novotny, "Enhancement and Quenching of Single-Molecule Fluorescence," *Physical Review Letters*, vol. 96, p. 113 002, 2006.
- [18] T. Mano, R. Nötzel, G. J. Hamhuis, T. J. Eijkemans, and J. H. Wolter, "Direct imaging of self-organized anisotropic strain engineering for improved one-dimensional ordering of (In,Ga)As quantum dot arrays," *Journal of Applied Physics*, vol. 95, p. 109, 2004.
- [19] P. Atkinson, M. B. Ward, S. P. Bremner, D. Anderson, T. Farrow, G. A. C. Jones, A. J. Shields, and D. A. Ritchie, "Site-Control of InAs Quantum Dots using *Ex-Situ* Electron-Beam Lithographic Patterning of GaAs Substrates," *Japanese Journal of Applied Physics*, vol. 45, p. 2519, 2006.

- [20] C. Schneider, A. Huggenberger, T. Sünner, T. Heindel, M. Strauß, S. Göpfert, P. Weinmann, S. Reitzenstein, L. Worschech, M. Kamp, S. Höfling, and A. Forchel, “Single site-controlled In(Ga)As/GaAs quantum dots: growth, properties and device integration,” *Nanotechnology*, vol. 20, p. 434 012, 2009.
- [21] K. Ohta, T. Kojima, and T. Nakagawa, “Anisotropic surface migration of Ga atoms on GaAs (001),” *Journal of Crystal Growth*, vol. 95, p. 71, 1989.
- [22] Tatau and Nishinaga, “Atomistic aspects of molecular beam epitaxy,” *Progress in Crystal Growth and Characterization of Materials*, vol. 48–49, p. 104, 2004.
- [23] T. Ogura, D. Kishimoto, and T. Nishinaga, “Effect of As molecular species on inter-surface diffusion in GaAs MBE for ridge structure fabrication,” *Journal of Crystal Growth*, vol. 226, p. 179, 2001.
- [24] S. Matteson and H. D. Shih, “Morphological studies of oval defects in GaAs epitaxial layers grown by molecular beam epitaxy,” *Applied Physics Letters*, vol. 48, p. 47, 1986.
- [25] A. S. Holmes, R. R. A. Syms, M. Li, and M. Green, “Fabrication of buried channel waveguides on silicon substrates using spin-on glass,” *Applied Optics*, vol. 32, p. 4916, 1993.

7 Conclusions and outlook

To conclude, the most important result of this thesis is the demonstration of the strain-driven self-assembly of epitaxial metal NCs on top of surface and near-surface epitaxial QDs grown by MBE. This allows to obtain hybrid metal-semiconductor structures in many configurations with single nanometer distance control, what is necessary for optimization of the QD emitter to metal NC coupling. To the best of the authors knowledge, it is the first demonstration of such bottom-up approach for the fabrication of hybrid plasmonic nanostructures. It is quite universal, as it was demonstrated to work both in the In/InAs/GaAs, as well as Ag/InAs/GaAs material systems. The latter is of particular practical importance, because Ag is the metal of choice for plasmonics with its lowest resistive losses. What is more, it was shown that the obtained metal NCs support LSPRs tunable over wide range from below 0.9 to 1.7 μm , what covers both 1.3 and 1.5 μm telecommunication bands. Additionally, it matches well the typical emission wavelength range of InAs/GaAs QDs.

Investigations of ordered structures with In NCs on top of 1D QD arrays resulted in the observation of an additional PL band coinciding spectrally with the LSPR wavelength. In micro-PL measurements it resolved into emission lines of individual QDs. It was concluded that this new PL feature is due to QD emission enhancement facilitated by coupling to the LSPR of the In NCs. Measurements of low density hybrid structures with Ag NCs revealed large enhancements of the emitted PL as well. In this case, however, the bulk PL emission from the GaAs substrates was also greatly enhanced. No characteristic features coinciding with the LSPR and no strong polarization dependence of the emitted light, expected in the case of coupling to the strongly anisotropic Ag NCs, were observed. It was concluded that the measured PL intensity increase is due to the LSPR enhanced absorption of the exciting laser light. Additionally, preliminary results of micro PL measurements on samples with Ag NCs were presented with clear enhancement and easily resolved individual QD lines. More investigations, however, are necessary to clarify the enhancement mechanism in that case.

It has been also demonstrated that MBE grown In NCs can be converted into InAs QDs of high optical quality evidenced by narrow PL emission linewidths. Due to the alternative growth process, as opposed to usual SK growth, the obtained QDs have different properties. Firstly, they form a smaller total InAs coverage, what makes them unstable and facilitates a novel emission wavelength tuning mechanism. Secondly,

7 Conclusions and outlook

in some cases they have suppressed WL emission, what is also attributed to the lower InAs coverage. Last, but not least, they are good candidates for achieving long emission wavelengths. This fact makes them extremely interesting from the applied point of view.

Finally, it was shown that it is possible to align Ag NCs in lithographically defined holes in a GaAs substrate. This was only possible when first QDs were grown in those holes, proving once again that the positioning of the metal NCs is strain, and not surface morphology, driven. The Ag NC alignment was demonstrated with a high degree of long-range ordering, what is an important achievement in the context of fabrication of integrated plasmonic devices.

The author sees a lot of potential for applications of the presented results. However, more development is necessary. Firstly, more investigations on the coupling of individual QDs to the LSPRs of the metal NCs are needed. Such investigations are important for better understanding of the optimum QD-NC conditions, and additionally could lead to observations of effects such as dipole-approximation breaking, which are interesting from the basic physics point of view. Secondly, it is very important to investigate different passivation schemes in order to minimize the nonradiative losses in the QDs due to close proximity of the metal, as well as the semiconductor-air interface. Development of an appropriate passivation and planarization scheme is also necessary to prevent the deterioration of the properties of the QDs and enable further integration, respectively. This is obviously essential if the hybrid structures presented in this thesis are to be used in real devices. Last, but not least, further investigations of the In NC to InAs QD conversion process are necessary to achieve better understanding of its unusual features. This includes in particular optimization of the long wavelength emission and QD density, in order to enable the device applications of such QDs

Abstract

Epitaxial Metal Nanocrystal-Semiconductor Quantum Dot Hybrid Structures for Plasmonics

Certainly one of the most fascinating applications of plasmonics is in active structures like nanolasers, optical transistors and photonic switches, where a metal nanostructure is combined with a single emitter, for example a semiconductor quantum dot (QD). Such hybrid nanostructures can easily be scaled to subwavelength dimensions. However, fabrication of such devices requires single-nanometer precise control of the separation of the metal nanostructure and the emitter due to the extremely high confinement of electromagnetic field of the surface plasmon resonance (SPR) supported by metal nanostructures. The approach presented in the thesis to solve this problem is based on the alignment of epitaxial metal nanocrystals (NCs) on near surface InAs QDs all grown by molecular beam epitaxy (MBE). It is demonstrated to work for In, as well as Ag NCs, the latter metal being material of choice for plasmonic applications, as it offers lowest resistive losses. What is more, this approach, being based on standard epitaxial growth technology, offers the possibility of integration of active plasmonic structures with existing photonic and electronic semiconductor devices.

The main result of the thesis is the demonstration of self-alignment of epitaxial Ag and In NCs on epitaxial near surface InAs QDs grown on GaAs (100) substrates by MBE. The SPR positions of the metal NCs can be tuned over a wide range covering the emission wavelength of the QDs. Low temperature photoluminescence (PL) measurements reveal enhanced intensity of the emission with lines from individual QDs being resolved. It is also demonstrated that the Ag NCs can be ordered over large length scales on patterned substrates provided that first site-controlled QDs are grown in those patterns. This provides a unique bottom-up approach for the integration of many metal nanostructures into one complex plasmonic device.

Additionally, it is shown that In NCs can be converted to high optical quality QDs with a number of unique features. Due to the radically different growth process than in the case of Stranski-Krastanov (SK) QDs, it is much easier to obtain low density QDs. The total InAs coverage is below the critical thickness observed for SK QDs, what enables a novel

PL wavelength tuning mechanism. Additionally it is shown that the QDs obtained by conversion of In NCs are good candidates for obtaining long wavelength emission in the InAs/GaAs material system.

Acknowledgements

I am sure that the work presented in this thesis wouldn't be successful without the help and assistance of many other people. Because of that I am very happy I can acknowledge their input in writing so it will not be forgotten how much they contributed to my PhD project.

Firstly, I have to admit that I am greatly indebted to prof.dr. Richard Nötzel, my daily supervisor, for his guidance and help at all phases of my project. Richard, I really enjoyed working with you and I am very glad I become your PhD student because I liked your style of supervising me a lot. I wish you all the best in your private as well as scientific life. I sincerely hope you and your new group in Madrid will be very successful. Take care!

Secondly, I would like to thank prof.dr. Paul Koenraad, the promotor of my PhD thesis. Thank you Paul for your positive attitude and prompt support of my project, especially in the final phase. You were very flexible what helped a lot me in my slightly extraordinary situation.

Thirdly, I am very grateful to my committee members: prof.dr. Luis Viña, prof.dr. Jan Misiewicz, prof.dr. Jaime Gómez Rivas, prof.dr. Stefano Sanguinetti and dr. Rob van der Heijden. Thank you for all comments and for finding the time to take part in my PhD defense.

I would also like to acknowledge all the help I received from dr. Andrei Silov on many things related to optics and more. Andrei, it was really nice to work with you.

As a large part of my project I was growing samples by MBE. That is why I am really grateful for all the support from Rian who introduced to the practical side of MBE growth and who worked with me on the Varian system. I also owe a lot to Frank who supported me during my work on the Createc system. Thanks a lot guys for all the technical and non-technical things, nothing would be possible without you! I also have to acknowledge our MOVPE specialist, Rene, for his friendly attitude and support in many matters.

I would like to thank Erik Jan, Tjibbe and Barry for helping me with SEM, optical lithography and chemical etching of my samples for site-controlled growth. During this work I learned the hard way about the importance of laboratory safety. Barry deserves an extra acknowledgment for his immediate help in the times of emergency!

I have to thank Tom for introducing me to our AFM and PL setup, as well as Martine who continued his efforts. Many thanks to other two PSN technicians, namely Jos and Peter, for their support. Very big thanks has to go to Margriet and Annebee who made all the unorganized and

impossible things neat and manageable. Without you we would all drown in administrative chaos.

I enjoyed a lot the work with my fellow growers. Ekber, Nut, Junji, Alex, Jan, Hao, Jia, Tian and YongJin – thanks and all the best for the future!

PSN as a whole is a very nice group and I am very proud I could be a part of it. I especially have to acknowledge many people with whom I had nice personal and scientific interactions (this time the order really does not matter): Matthias, Mehmet, Cem, Niek, Joost, Robert, Leonardo, Steven, Erwin, Juanita, Thang, Arjan, Francesco, Samuel, Jens, Döndü, Thuy, Joris, Saeedeh, Salman, Sartoon, Tilman, Milo, Giulia, Chaoyuan, Bowen, Zili, Rosalinda, Ilaria and many others. It was a real pleasure!

Finally, big thanks goes to my parents and to my girlfriend Barbara. Your support really made a huge difference!

List of publications

A. Urbańczyk, G. J. Hamhuis, and R. Nötzel, *In islands and their conversion to InAs quantum dots on GaAs (100): Structural and optical properties*, Journal of Applied Physics **107**, 014312 (2010)

A. Urbańczyk, G. J. Hamhuis, and R. Nötzel, *Strain-driven alignment of In nanocrystals on InGaAs quantum dot arrays and coupled plasmon-quantum dot emission*, Applied Physics Letters **96**, 113101 (2010)

A. Urbańczyk, G. J. Hamhuis, and R. Nötzel, *Coupling of single InGaAs quantum dots to the plasmon resonance of a metal nanocrystal*, Applied Physics Letters **97**, 043105 (2010)

A. Urbańczyk, G. J. Hamhuis, and R. Nötzel, *Single InGaAs Quantum Dot Coupling to the Plasmon Resonance of a Metal Nanocrystal*, Nanoscale Research Letters **5**, 1926 (2010)

Adam Urbańczyk, Frank W. M. van Otten, and Richard Nötzel, *Self-aligned epitaxial metal-semiconductor hybrid nanostructures for plasmonics*, Applied Physics Letters **98**, 243110 (2011)

A. Urbańczyk, G. J. Hamhuis, and R. Nötzel, *Hybrid semiconductor quantum dot-metal nanocrystal structures prepared by molecular beam epitaxy*, Journal of Crystal Growth **323**, 290 (2011)

R. Nötzel and A. Urbańczyk, *Epitaxial self-alignment: A new route to hybrid active plasmonic nanostructures*, Current Opinion in Solid State and Materials Science, **16**, 59 (2012)

A. Urbańczyk and R. Nötzel, *Low-density InAs QDs with subcritical coverage obtained by conversion of In nanocrystals*, Journal of Crystal Growth, **341**, 24 (2012)

A. Urbańczyk and R. Nötzel, *Site-Controlled Ag Nanocrystals Grown by Molecular Beam Epitaxy - Towards Plasmonic Integration Technology*, Journal of Applied Physics, submitted

Curriculum vitae

Adam Jan Urbańczyk, born 9th June 1984 in Wrocław, Poland

2008-2012

Ph.D. in physics in Photonics and Semiconductor Nanophysics group, Department of Applied Physics, Eindhoven University of Technology. Thesis title: *Epitaxial Metal Nanocrystal-Semiconductor Quantum Dot Hybrid Structures for Plasmonics*, promotor: prof.dr. Paul Koenraad, copromotor: dr. Richard Nötzel.

2003-2008

M.Sc. in applied physics, Department of Physics, Wrocław University of Technology, Poland

M.Sc thesis title: *Electrical and optical characterization of MOS structures on III-V compounds*, promotor: prof.dr. Jan Misiewicz, copromotor: dr. Guy Brammertz. Thesis realized partially at IMEC, Lueven, Belgium

The Scholarship of Polish Ministry of Science and Higher Education for outstanding students in the academic year 2007/08

The Scholarship of Polish Ministry of Science and Higher Education for outstanding students in the academic year 2006/07

1998-2003

14th Highschool in Wrocław, Poland